ABSTRACT

Title of dissertation: HYDROMAGNETIC TURBULENT INSTABILITY IN LIQUID SODIUM EXPERIMENTS

Daniel R. Sisan, Doctor of Philosophy, 2004

Dissertation directed by: Professor Daniel P. Lathrop
Department of Physics

This dissertation describes the observation of magnetically-induced instabilities that occur from a preexisting hydrodynamically turbulent background. We claim these instabilities are the first direct observation of the magneto-rotational instability (MRI). An extensive body of theoretical and numerical research has established the MRI is important in the theory of accretion disks: magnetic fields destabilize otherwise stable astrophysical flows, causing turbulence and an increased angular momentum transport needed for accretion. Our instabilities occur in liquid sodium between differentially rotating concentric spheres (spherical Couette flow) where an external field is applied parallel to the axis of rotation. Our experiments are also the first known spherical Couette flow in an electrically conducting fluid, and only the second experiment, in any fluid, at an aspect ratio of $\beta = 2$, the same

of the Earth's core. We describe the development of a Hall probe array that measures the field at 30 points outside the sphere and is used to perform a spherical harmonic decomposition (up to $l = 4$) of the induced field. We present measurements taken with this array, along with measurements of torque needed to spin the inner sphere and of the flow velocity using ultrasound doppler velocimetry. Our experiment is consistent with prior theory, even though our instabilities occur in the presence of preexisting hydrodynamic turbulence (the theory starts with an initially laminar flow). This result may be particularly relevant in light of an ongoing debate on whether accretion disks are hydrodynamically unstable independent of external fields. The most important contribution of our experiments, however, may be in providing data with which to benchmark the many numerical and theoretical studies of the MRI and the codes used to simulate the Earth's core.

HYDROMAGNETIC TURBULENT INSTABILITY

IN LIQUID SODIUM EXPERIMENTS

by

Daniel R. Sisan

Dissertation submitted to the Faculty of the Graduate School of the
University of Maryland, College Park in partial fulfillment
of the requirements for the degree of
Doctor of Philosophy
2004

Advisory Commmittee:

Professor Daniel P. Lathrop, Chair/Advisor
Professor Thomas Antonsen
Professor William Dorland
Professor Rajarshi Roy
Professor Eve Ostriker

ACKNOWLEDGEMENTS

The acknowledgements, with the possible exception of the abstract, is perhaps the section most likely to be read in its entirety. The author, for one, admits to reading only the acknowledgements section of more than one dissertation. With this in mind, the author would first like to acknowledge you, the reader. Thanks for picking this up! One can only expect a Ph. D. dissertation to be looked at by so many people. Should you decide to read on[1]—or perhaps perform your own liquid sodium experiments—your efforts are fully appreciated and encouraged. The author would also like to preemptively acknowledge your forgiving any errors or shortcomings of the dissertation, including any of this very section, which you might want to skip after all, as it is a bit long and refers to people with whom you are likely unfamiliar.

The author would now like to switch to the first person, as the following would sound strange otherwise, and acknowledge the many people who helped make this research and dissertation possible.

Don Martin, at nearly every stage of my research, provided valuable technical advice and assistance. Before I arrived, he had constructed much of my experimental apparatus, and he made many additional parts that were needed along the way. Whenever I needed to build or modify a part of the experiment, his ideas and technical knowledge were always useful.

[1] If not, the author suggests looking at the figures as a compromise.

Former graduate student Nick Peffley helped me get started in the lab, showing me the intricacies of the experimental apparatus and the proper respect for (not fear of) sodium. I benefited also from the considerable work he and Fred Cawthorne put into the system before I inherited it. In particular, the plumbing, temperature control, data acquisition, and LABVIEW program were working together properly—which took months to put together and troubleshoot. Fred Cawthorne also built several electronic components and wrote a program (`cbhall_t`) that are still used (the latter in slightly modified form). Once I took over the experiment, Woody Shew and later Dan Zimmerman individually made lasting improvements to the system. In my first years Woody Shew also collaborated in running the experiments. More recently, Nicolás Mujica built the sodium-proof ultrasound transducer that allowed us to measure flow velocities. He and I together ran the spherical Couette experiment that forms the bulk of this dissertation. He's been a valuable collaborator in many other ways as well, and my last year and half here has been more productive because of him.

I would like to thank Santiago Triana, Kaveri Joshi, Dan Blum, Khurram Gulani, Matt Martin, and especially Dan Zimmerman, Nicolas Mujica, and Woody Shew for serving on "leak watch," and for assisting in the arduous task of (dis)assembling the system. Their help was instrumental in every run. I would also like to thank Benjamin Zeff and Dottie Brosius for providing the template for this dissertation, and Nicolás Mujica for carefully reading a late draft, finding several errors and suggesting other improvements.

Most of all I would like to thank my advisor, Dan Lathrop. He provided the idea and funding for the project, opportunities to attend interesting conferences (and to stare seriously at fake data on national television!), and invaluable guidance throughout my graduate career. He's helped with runs, data analysis, and troubleshooting a pesky prob-

lem. Less directly though no less importantly, I've learned from his example of an effective and productive scientist (or so I hope). I've even picked up several of his idiosyncracies—from some of his distinctive vocabulary to his general distaste for acronyms, which this dissertation nonetheless contains. In short, he's been the ideal "admixture" of advisor, teacher, role model, and friend. Grad school has been a more "robustifying" experience because of it!

To all my labmates past and present: thanks for years of making my workweeks fun. In particular, our lunchtime discussions of "controversial topics" were always interesting, and quite often the highlight of the day. To the lovely Heather Lindsay: thank you for your moral support and companionship, especially in these stressful last few months. I'm glad I met you.

Lastly I would like to express gratitude and love to my parents, who have been supportive every step of the way. I dedicate this dissertation to them.

TABLE OF CONTENTS

LIST OF TABLES

Partial List of Abbreviations

B_{ext}	external magnetic field
b	induced field
$\vec{B}$	magnetic field
$\vec{J}$	current density
U	typical velocity scale
L	typical length scale
ν	kinematic viscosity
ρ	density
μ_0	permeability of free space
η	magnetic diffusivity
σ	electrical conductivity
$\sigma(G)$	standard deviation in Gauss
$d\sigma$	differential area element
Ω	inner sphere rotation rate
$\Omega(s)$	angular velocity flow profile in cylindrical radius
L	angular momentum
a	outer sphere radius
b	inner sphere radius, or impeller radius
P_m	magnetic Prandtl number
R_m	magnetic Reynolds number
Re	Reynolds number
N	interaction parameter
S	Lundquist number
Ha	Hartmann number
$\vec{S}$, $\vec{T}$	poloidal and toroidal vector modes
ζ	vorticity index
Γ	torque
G	dimensionless torque
g	Gauss coefficient
MRI	magneto-rotational instability
MHD	magnetohydrodynamic(s)

Chapter 1

Introduction

Before declaring our topic's importance and ubiquity in nature—a popular starting point in scientific discourse—we follow a more pragmatic route and define our topic. In particular we turn to the title, where two somewhat unconventional terms appear. First, "turbulent instability" refers to an instability occurring from a preexisting turbulent background; almost invariably in fluid dynamics instabilities occur instead from a laminar state and *cause* any subsequent turbulence. Second, "hydromagnetic" refers to the interaction of an electrically-conducting fluid with magnetic fields. We use this term in place of the more common[1] "MHD," short for magnetohydrodynamic.

But as we avoid one acronym, we turn to another: the hydromagnetic state that we focus on is the magneto-rotational instability, or the MRI. The MRI plays a central role in theory of accretion disks, which are found around stars and black holes, and in the centers of galaxies. We claim here to have the first direct observations of the MRI: in liquid sodium flowing between concentric spheres with external fields applied parallel to the axis of rotation. Flow between concentric spheres is usually called spherical Couette flow, and as far as we know, we also report the first experimental study of hydromagnetic flow in that geometry—and one of only a few in any simple geometry. We also present

[1] Though less common, "hydromagnetic" does predate "MHD" and was used by the pioneers Chandrasekhar and Connelly, among others.

previously-published results from an experiment with co-rotating impellers (with no inner sphere). Though not mentioned in the paper [91]—and the data are less conclusive—that experiment likely shows the MRI as well.

Even without the astrophysical connection, our experiments are interesting from an electromagnetic and fluid dynamics point of view. Depending on the applied magnetic field strength, states with a wide range of prominent features result—from relatively simple azimuthally-precessing patterns, to irregularly-oscillating axisymmetric bands with short-lived precessing structures, to beating patterns resulting from competing modes—showcasing the dynamical richness hydromagnetic turbulence has to offer.

1.1 A brief history of the project

As is often the case in science, the initial motivation for pursuing this project was not what ultimately made it most interesting. The current experiments sprung from the context of homogenous dynamo experiments. Like the MRI, a homogenous dynamo is an instability that occurs in electrically-conducting flows. In a dynamo, however, the initial growth occurs only in the magnetic field and the field becomes self-sustaining.[2] We [83], along with several other groups [78, 77, 5], have been trying to produce a homogenous dynamo in the laboratory using liquid metals, though unsuccessfully. The experimental apparatus used in this dissertation was first used to attempt a mechanically-forced dynamo (as opposed to a convectively-driven one), and still goes colloquially in the lab by the name "Dynamo II."

In these previous experiments, pulsed-decay measurements of small external magnetic fields probed how close the system was to a self-generating dynamo. We found

[2] A dynamo is a device that converts mechanical energy to electric energy. Homogenous means the conductor in the dynamo is uniform and simply-connected—unlike, say, the wrapping of wire in a generator.

a linear trend toward self-generation in the decay rate with magnetic Reynolds number (non-dimensional rotation rate) but power limits were reached at a 1/3 of the way [83]. The magnetic Reynolds number is $R_m \equiv UL/\eta$, where U and L are typical velocity and length scales, and η is the magnetic diffusivity; R_m quantifies the ratio of field advection to diffusion, and must be greater than unity to produce a dynamo. Large R_m is not enough however; flow geometry matters greatly. The flow in the original experiments [83] was driven by counter-rotating impellers, as inspired by the numerical work of Dudley and James [31]. Multiple geometric variations were subsequently tried to strengthen the trend to self-generation [93, 66], but to no avail. Though the lack of a dynamo was disappointing, the trend was encouraging—enough that a much larger system (capable of larger R_m) has been proposed and funded, and which should be online perhaps within a year.

Small external fields were used in these attempted dynamos so that Lorentz forces did not alter the flow. A next step was to apply large fields to purposefully alter the flow. In other words, the ratio of the Lorentz to inertial forces—the interaction parameter—is made greater than unity. The interaction parameter is $N = B^2 L\sigma/\rho\mu_0\eta U$, where B is the magnetic field, U and L characteristic velocity and length scales, ρ the density, and σ the electrical conductivity.

Had a dynamo developed, one of the more interesting results would have been the subsequent saturation—at what value would the field stop growing? Lorentz forces would necessarily be involved, as it is the only available mechanism for altering the flow to halt the growth. By applying large external fields, we expected to find clues to the process, even without a dynamo. What we found, and subsequently focused on, probably has limited applicability to dynamo saturation but is interesting nonetheless: with co-rotating impellers the magnetic field exhibited somewhat peculiar oscillations. We published the

results in a geophysical journal [91], parts of which are found in Chapter 5.

Similar dynamics had been found numerically in spherical Couette flow by Hollerbach and Skinner [50], though at much lower Reynolds number. To better compare to these results—and realizing that no numerical study could incorporate our complicated impellers—we began to study spherical Couette flow. In the process we built an array of Hall probes to decompose the field into spherical harmonics, developed an ultrasound transducer to measure the velocity of sodium, and became aware of the work of Hantao Ji [53] and Gunther Rüdiger [59] and their collaborators (and others) who were exploring the possibility of studying the MRI in the lab. The result comprises the rest of this dissertation.

On this note we should warn that interpreting our results as the MRI is still somewhat controversial. There are several alternative interpretations, the most likely coming from the paper by Hollerbach and Skinner. We discuss these alternative explanations in Chapter 5.

1.2 Relation to other experiments

What distinguishes our experiments is the combination of simple geometry, turbulence (large Reynolds number), and large applied magnetic fields (near unity interaction parameter). Here we discuss other experiments having some of the same or similar features to our own.

1.2.1 Non-magnetic spherical Couette experiments

Though we present the first hydromagnetic experiment in spherical Couette geometry, many spherical Couette experiments have been performed in water. Nearly all of them are with medium to narrow gap widths, however. The gap width in a spherical Couette

geometry is specified by the aspect ratio $\beta \equiv (a-b)/a$, where a and b are the outer and inner sphere radii respectively. In the literature $\beta \geq 0.25$ is considered wide, so our geometry, with aspect ratio $\beta = 2$, falls well into the wide gap category. In fact, there is only one known experiment at our aspect ratio [56]—a somewhat surprising paucity considering the geophysical motivation often ascribed to many spherical Couette studies and that the Earth's core has this aspect ratio.[3] There is one other experiment at a slightly larger aspect ratio ($\beta = 2.29$) [75]; all other known experiments are at smaller gap widths. The number of spherical Couette experiments—at any aspect ratio—is quite small, compared to, say, the number of cylindrical Couette experiments or plane shear flow experiments—two other basic fluid experiments. In fact, spherical Couette has elements of both these geometries, being like cylindrical Couette flow at the equator and like plane flow at the poles.

In the spherical Couette experiments—as well as the other simple geometry hydrodynamic experiments—the focus is often on the symmetry-breaking bifurcations leading from laminar flow to turbulence. Spherical Couette flow involves two types of symmetry: reflection symmetry about the origin and rotational symmetry. Depending on the aspect ratio, both types of symmetry breaking bifurcations occur. The types of states one finds in these spherical Couette studies, which share basic features with other hydrodynamic instabilities, are Taylor vortices (toroidal vortices wrapped around the azimuthal direction) near the equator, travelling wavy Taylor vortices, spiral Taylor vortices, and travelling spiral waves.

[3] We presume the geophysical motivation in those studies concerned not the Earth's core but its atmosphere, which does have a narrow gap geometry.

Adding a dimension

By imposing an external field and allowing for Lorentz force interactions, we allow another degree of freedom. Correspondingly we might expect richer dynamics. We explore parameter ranges in these experiments where the applied fields are large enough to alter the flow: near unity interaction parameter. This parameter range should be the most interesting regime, as a competition exists between two dominant forces.

We find in our experiments here that the applied magnetic fields can cause many of the bifurcations one sees at much lower Reynolds numbers, except that they take place from a turbulent background. This is perhaps not surprising. The time-averaged turbulent state has the same rotational and reflectional symmetries as the laminar flow, and the applied field can break these symmetries—in fact *must* break the latter at high external field. The instabilities we see in our experiment have qualities common to the instabilities that generate the turbulence in the first place.

1.2.2 Dynamo experiments

As mentioned earlier, several groups including our own have been trying to produce homogenous dynamos in the laboratory. However, groups in Riga, Latvia [38, 37] and Karlsruhe, Germany [97] have actually produced liquid metal laboratory dynamos, though in geometries that force helical flow using baffling and duct-work.

These liquid metal dynamos are substantial achievements, but their geophysical relevance may be limited. First, in those experiments turbulence may not play an important role in the magnetic field dynamics. For instance, the Karlsruhe dynamo is two-scale: while the velocity field is small-scale and turbulent, the magnetic field is large scale and apparently unaffected by the fluid turbulence. Second, in both the Riga and Karlsruhe ex-

periments the magnetic field reaches equilibrium through mechanisms simpler than what would operate in a less constrained dynamo. In the Karlsruhe experiment, the equilibrium magnetic energy corresponds simply to the pressure head in excess of the critical value for dynamo action. In a less constrained dynamo, the equilibrium magnetic energy would be much harder to predict as Lorentz forces would alter the flow in a more complicated way. Gailitis et al. [37] presented evidence of saturation in the Riga dynamo experiment that appears more complicated than the saturation in the Karlsruhe experiment. However, the saturated field value was small (8 G) for moderate magnetic Reynolds number, corresponding to an interaction parameter much less than one, far from the regime thought present in the Earth.

We should point out that turbulence *does* appear important in the saturation of the Riga (and possibly the Karlsruhe) experiment [34]. Dimensional analysis assuming turbulence (i.e., neglecting viscosity) predicts a saturated interaction parameter that is $Pm^{-1/2}$ the corresponding laminar value; the turbulent prediction is close to the Riga value.

We have not produced a self-generating dynamo like the experiments in Karlsruhe and Riga, and our results have little direct relevance to dynamos, but we our closer to the parameter range where the Earth's dynamo is thought to operate. For a more extensive discussion of the relation between dynamo theory and experiments see a review by Busse [17].

1.2.3 Other hydromagnetic experiments

There are only a handful of other experiments using electrically-conducting fluids and applied fields in a simple geometry [27, 28, 29, 13]—all of them in cylindrical Taylor-Couette

flow, and all but one performed by Donnelly and collaborators. These experiments focused on the stabilization of centrifugal instabilities by external fields—quite opposite the MRI, in which external fields turn a centrifugally stable flow unstable! Since these experiments examined the onset of turbulence, these experiments were at Reynolds numbers much lower than ours.

Many other experimental studies of magnetic fields on electrically-conducting flows in other geometries (Rayleigh-Benard convection, duct flows, magnetically-driven flows, flow around obstacles, etc.) have been performed [74, 16]. However, to our knowledge, no experiments have been performed for high interaction parameter N, $R_m = UL/\eta > 1$.

1.3 Geophysical and astrophysical relevance

1.3.1 The role of the MRI

Accretion disks, from which stars and planets are thought to form, are disk-shaped rotating clouds of gas. The gas particles are attracted gravitationally to a central, dense core and are held in orbit by the balance of centrifugal forces. When gas particles in neighboring orbits bump into each other, they transfer angular momentum. In orbital dynamics, if a particle loses angular momentum from a deceleration in the azimuthal direction it drops to a lower orbit. However, in a Keplerian disk, where the angular momentum increases with radius (as $r^{1/2}$), a lower orbit has a *higher* angular momentum. Since a closed system preserves its angular momentum, these perturbed trajectories get restored. Conversely, accelerated particles go to higher orbits and likewise return to their orbits. The flow is stable.

The situation changes if there are stresses within the flow that sap angular momentum from the system. Angular momentum can be lost through viscosity—molecular

friction that transfers kinetic energy into heat—which leads to gas particles falling inward: accretion. Using the expected values of the microscopic viscosities, however, accretion models predict accretion rates that are several orders of magnitude too small (see, e.g., [95]).

Turbulence—through the action of the so-called Reynolds stress—leads to angular momentum loss too. Ultimately the resulting energy loss there is converted into heat through viscosity too, but turbulent dissipation does not depend on the value of the viscosity. By analogy to laminar flow, this extra dissipation is sometimes accounted for by a larger effective turbulent viscosity. However, turbulent dissipation depends on the structure of the flow, and usually cannot be predicted by a single scalar parameter. Turbulent viscosities are variously used in the literature nonetheless (e.g., [14]). To fix the problem of too slow accretion, the same basic approach was incorporated into accretion models by setting the amount of turbulence by a parameter—a proportionality constant relating the turbulent stresses to the disk pressure. Models that parameterize turbulence in this way are sometimes called alpha models—only because the constant of proportionality is denoted by the symbol α. Two α- accretion models that have become standards in this style are those of Shakura and Sunyaev [92] and Lynden-Bell and Pringle [71].

Work on accretion theory using α models continued for years, allowing a substantial amount of progress [48]. There were two problems, however. First, the underlying physics of the turbulent Reynolds stress was not understood. Second, and more importantly, it was not known if having turbulence in accretion systems was even justified—even considering that the Reynolds number of typical accretion disks is typically very large ($Re \sim 10^8$), due to their large (indeed astronomical) length scales. Laboratory flows are known to become turbulent at Reynolds numbers orders of magnitude smaller ($Re \sim 10^3$, depending on the

particular flow), but the turbulence arises from centrifugal instabilities. Accretion disks, however, are centrifugally stable, and so turbulence seemed unlikely to develop. The only justification for using turbulent values for α was that accretion had to occur.

In 1991 the situation changed when Balbus and Hawley published a series of papers describing a linear instability arising in differential flows with weak magnetic fields [9, 46, 10]. As long as ionization and magnetic fields were present in accretion disks—a likely scenario—a means to generate the presupposed turbulence was found. The magnetic fields do more than just trigger turbulence, though. They are inexorably linked with the continuing dynamics—Maxwell stresses (stresses from the Lorentz force) are just as important as Reynolds stresses. For a while the instability was called the Balbus-Hawley instability, but now it is typically called the magneto-rotational instability, or MRI. Actually the MRI was independently discovered by Velikhov [103] and Chandrasekhar [19], but its astrophysical implications were not realized. Since 1991, Balbus and Hawley and a number of other researchers have explored many aspects of the MRI, producing a significant body of MRI literature [11]. Balbus and Hawley's first 1991 paper, for instance, has been cited over 600 times.

1.3.2 Experimental astrophysics

The studies in the magneto-rotational instability literature have been guided by astronomical observation, but there have been no direct comparisons to controlled experiments. Indeed, the term "experimental astronomy" when it is used usually refers to observation astronomy—observing astrophysical objects themselves, through imaging, spectroscopy, radiometry, etc. Here we provide the rare example of an astrophysical phenomena that can be studied in the *laboratory*: an experiment by the usual physics definition.

In fact, multiple papers have explored the possibility of observing the MRI in just this way. One of these papers, by Ji, Goodman and Kageyama [53], calculates through WKB methods a stability condition for a Taylor-Couette flow based on the local dispersion relation, which when adapted to our experiment produces qualitative and quantitative agreement with our data. Goodman and Ji also perform the corresponding global calculation and find that it differs little from the local analysis. A similar local analysis in the same geometry has been performed by Noguchi et al. [76], and by Rüdiger and collaborators [89, 90], and in a spherical geometry [59].

Because there are very few laboratory experiments in astrophysics, these experiments are more noteworthy—but also more difficult to interpret. In geophysics, by contrast, where experiments are more common (e.g., [15, 97, 78, 83]), there is a shared literature that includes experiment, theory, and simulation (e.g., [24]).

Another possible difficulty in interpreting our experiment astrophysically will be simply in identifying it as the MRI: our instability occurs from a hydrodynamically turbulent background. This difficulty, however, may also be what proves most interesting. The MRI has been considered important because it *generates* needed turbulence and angular momentum transport for accretion to work. Here we will provide evidence the MRI occurs—and that angular momentum transport increases—even in the presence of *preexisting* hydrodynamic turbulence. This may broaden the relevance of the MRI to astrophysical and geophysical flows that are not expected to be centrifugally stable.

Our results may be especially important in the face of recent challenges to the prevailing view in the astrophysics community that Keplerian disks, in the absence of magnetic fields, are hydrodynamically stable. Among the possible routes to hydrodynamical turbulence are nonlinear instabilities and the so-called *bypass* concept [18], where linear growth

occurs only if perturbations reach a certain finite amplitude. The former was examined in particular by Balbus, Hawley, and Stone [11] and others [88], and they concluded that none were likely in accretion disks, but more recent challenges have come about [70, 84]. Other possible processes leading to hydrodynamic turbulence in accretion disks are: a linear (spectral) instability arising from stratification perpendicular to the disk, and baroclinic instabilities [60, 101] resulting from vertical dependence of the cylindrical rotation. Even if these instabilities are present in accretion disks and produce purely hydrodynamic turbulence, our results suggest that magnetic fields will have continued importance in accretion disks.

If we've observed the MRI, we have what might be considered to some approximation an experimental model of a galaxy or a young star. Of course the model has serious limitations; those astrophysical flows have no boundaries that impose no-slip conditions as ours do, for instance. Other astrophysically important processes, like radiation, have no counterpart in our experiment either. Less seriously, the magnetic Prandtl number of sodium is $O(10^{-5})$ versus $O(1)$ for most (though not all) accretion disks.

Our experiment's differences with accretion disks, however, are similarities with the Earth's core. As we'll see next, we have to a closer approximation a model of the Earth's core.

1.3.3 Similarity to Earth's core

Our spherical Couette experiments have a similar geometry to the Earth's core, where a liquid iron outer core surrounds a solid inner core (solid because of the higher pressure). We have chosen our inner sphere so that our system has the same radius ratio as the Earth, 0.3. Seismological evidence suggests the inner core is rotating faster than the outer core

and mantle[94], just as our inner core rotates faster than the outer spherical vessel. The causal link is opposite in the two cases, however: in our experiments the rotation is forced and causes the induced field, whereas in the Earth the induced field is self-generated most likely by a combination of thermal and compositional convection, which causes the super-rotation. Nonetheless, the mechanical and electromagnetic couplings that occur in both cases follow the same principles. One way these couplings become important in the Earth is in variations of the Length of Day and in the orientation of Earth's axis of rotation. Both can result from a transfer of momentum from the fluid core to the mantle, directly equivalent to our torque measurements. Furthermore, should our experiments one day show dynamo action, our geometry, being like that of the Earth, would obviously be most suitable for comparison to direct measurements of the Earth's field and to geodynamo simulation.

Two basic approaches in the study of planetary cores were to analytically find a velocity field capable of producing a dynamo, and numerically to understand how the field saturates. The first was achieved by multiple researchers starting in the 1960s [96, 73, 31]; the latter has been achieved to some extent starting in the last decade by self-consistent numerical simulations [42, 61, 86, 30].

How does the MRI fit into the study of planetary cores? In fact its destabilizing effect calls the underlying conceptual approach used in most analytical studies into question. Small magnetic fields are not necessarily passive as assumed; they can drive turbulence, altering both the statistical properties and the mean flow. In the numerical studies, however, where the simulation is self-consistent, the MRI can probably be safely ignored, though considering it might bridge the two fields of study. The main effect of the MRI in the Earth's core would be as a mechanism for the initial field growth, and might affect

long-term features like the relative strengths of the toroidal to poloidal fields. The MRI might also manifest itself in the dynamics of these simulations or in the Earth's core, for instance with slowly precessing flux lobes, as discussed in Chapter 5.

Research on the Earth's core has to our knowledge not yet involved the MRI. Its absence in geodynamo research is not surprising. Unlike accretion disks, in the Earth's core there was never a problem of missing angular momentum transport, and with or without magnetic fields turbulence was never in question. Indeed turbulence is a continuing problem. With analytical studies, turbulence is either ignored or approximated and parameterized (e.g., the α-effect—which is distinct though not so fundamentally different from the α parameterization in accretion theory). In numerical studies, weak turbulence exists but realistic levels of turbulence cannot be fully resolved and so hyperdiffusivities or artificially large Prandtl numbers are used.

Experiments, however, are well-suited for studying turbulence. Our experiments reach parameter ranges inaccessible to numerical simulation, now or in the foreseeable future. To see why, one needs to understand how turbulent fluid systems are simulated.

1.4 Simulations and the problem of turbulence

While many fields of science are limited by a lack of direct information (e.g., in geophysics, basic information like the rotation rate of the Earth's inner core has to be indirectly inferred, leading to large uncertainty), the study of turbulence is in a way limited by too much. The information of turbulence lies entirely in the Navier-Stokes equation, which looks simple enough. But no algebraic turbulent solutions exist; instead, one can only numerically solve the equation at points in space (grid points) for successive steps in time. This description of course has a finite resolution, and to increase it one adds grid points

and time steps, which means adding computations and more memory.

As a flow becomes more turbulent, its simulation requires more resolution: the fluctuations become more irregular and occur over smaller lengths and shorter times, while the largest scales remain important. One can't just zoom in without losing important information. The problem with turbulence is that the resolution requirements quickly exceed the limits of modern computers.

We can quantify the resolution problem using the Reynolds number, Re. In fully developed turbulence, the Reynolds number relates the smallest length scale, often called the Kolmogorov length l_k, to the largest length scale L (generally the size of the system): $l_k = LRe^{-3/4}$. For a Reynolds number of $Re = 5 \times 10^6$—a typical value for experiments—the ratio of length scales L/l_k and thus the needed number of grid points for one dimension is 10^5. In three dimensions, the grid points needed is the cube of this ratio: $\sim 10^{15}$. Likewise, the smallest time scale, the Kolmogorov time τ_k, is related by the Reynolds number to the longest time scale (the turnover time L/U): $\tau_k = Re^{-1/2}L/U$. To simulate all the time dynamics at $Re = 5 \times 10^6$ ($\Omega/2\pi \approx 50$ Hz) for one second would then require 10^5 time steps. At each grid point the equations of motion are solved for three velocity components (and for us also three magnetic field components), meaning at least three operations per grid point. In total, that's $3 \times 10^{15} \times 10^5 = 3 \times 10^{20}$ calculations, and as many data bytes! For perspective, if one could use all the computing power on the National Science Foundation's recently funded 20 Teraflop computer network, the full simulation of one second of our experiment in a naive estimate would take about a year.

In practice, the time to simulate the experiment would be considerably longer as data would have to be written and read from hard disks at rates much slower than processor speeds. The maximum Reynolds number that can be simulated with fully resolved length

and time scales is around $Re = 10^3$. By contrast, the Reynolds number of the Earth's core, which is typical of other astrophysical flows, is around 10^8. Experiments can get far closer to this parameter range than any simulation can do—now or in the foreseeable future. A turbulence experiment, in essence, is a very powerful (though specialized) supercomputer.

Computer simulations do, however, have significant advantages over experiments. They can control every aspect of the simulation, for instance, and have complete knowledge of the dynamics. Experiments on the other hand have uncertainties and noise, and measurements are incomplete and often difficult. For instance, in our liquid sodium experiments, because the flow is opaque we can only measure the velocity using ultrasound doppler velocimetry, currently only along one line in the flow—and even that limited measurement was very challenging, as we'll see in Chapter 3. Furthermore, the $Re = 10^3$ limit on numerics can—to an acceptable approximation—be overcome. Numerical techniques have been developed (like using hyperdiffusivities) that try to artificially suppress turbulence while minimally affecting the essential dynamics. Also, in some situations simplifying assumptions can be made. Other times an under-resolved model is simply good enough.

1.4.1 Untangling the role of turbulence

Experiments deal readily with turbulence—indeed it's nearly unavoidable—and they are thus well-suited to untangle its role. One problem in which laboratory hydromagnetic turbulence experiments could offer insight is a dynamo or MRI saturation mechanism. In both, the magnetic field grows exponentially from the fluid motion, a result coming simply from linear analysis. But the challenging and interesting problem is to determine what turns the growth off—that is, what controls saturation. Turbulence almost certainly

plays a significant role. In the MRI literature, the problem of saturation is to find the magnetic energy as a function of the pressure, which, as formulated in an α model, is a constant times the turbulent stresses. In the Earth's core, small-scale currents, due to small-scale turbulent velocity fluctuations, contribute to Joule heat production, even if they do not contribute directly to the observable field. Joule heat production, which obviously cannot exceed the power source driving the dynamo, places limitations on the intensity of magnetic fields in the core.

Turbulence also has a dynamical effect on the Earth's field, as evidenced by the broad magnetic energy spectra at the core-mantle boundary. Satellite data imply that the Earth's field at the core-mantle boundary has significant contributions at least up to degree $l = 12$ [52]. As the Earth's mantle filters the field increasingly with higher l, the Earth's field may thus be even more broadband than we are able to infer from measurements at the surface.

Evidence that turbulence is significant in dynamos is also found in experiments [78, 83]. For instance, liquid metal experiments that should self-generate based on the time-averaged velocities do not in practice [72]. The time-dependent turbulent fluctuations apparently play a non-trivial (and, for at least some homogenous dynamos, detrimental) role.

So while any turbulent experiment is a sort of computational study of the Navier-Stokes equation (and induction equation, if the turbulence is hydromagnetic), ours has the added value that it can, to some extent, model the Earth's core and the magneto-rotational instability. It can also help computational studies by providing an experimental turbulent benchmark to calibrate to.

1.4.2 Benchmark numerical codes

A major motivation for this experiment was to provide a testbed for numerical codes that incorporate the Lorentz force. Experiments and numerical simulation, because of turbulence, are excellent complements.

In particular, the spherical Couette system described in this dissertation is an ideal benchmark for several reasons. First, the geometry is spherically symmetric and simple. In many hydromagnetic turbulence experiments [78, 83, 91], the flow is generated by moving impellers—complicated boundary conditions that are difficult to model. By contrast, the spherical Couette flow is driven by a simple moving boundary. Indeed, several codes that include Lorentz forces have already been developed in our geometry, for example those of Glatzmaier and Roberts [42], Kuang and Bloxham [61], and others [30] (though minor modification would be necessary to make the inner sphere rotate and the outer sphere stationary). Second, oscillating velocities and magnetic fields present a dynamic signature that is straightforward to compare. Trends, such as our torque measurements versus rotation rate and applied field, could be compared as well. Furthermore, these dynamics change with electrical boundary conditions, another dimension that can be benchmarked.

Lastly, since the complementary nature of experimental turbulence in simple geometries is the same for any experiment in a simple geometry, we should note one difference: the external fields suppress gradients in the direction of the field, which would lower the needed resolution in that direction.

Chapter 2

Theoretical background

2.1 Equations of motion

The equations of motion relevant to our system are the Navier-Stokes equation with the added Lorentz force:

$$\frac{\partial \vec{u}}{\partial t} + (\vec{u} \cdot \vec{\nabla})\vec{u} = -\frac{1}{\rho}\vec{\nabla}p + \nu\nabla^2\vec{u} + \frac{1}{\rho\mu_0}\left(\vec{\nabla} \times \vec{B}\right) \times \vec{B} \tag{2.1}$$

and the induction equation:

$$\frac{\partial \vec{B}}{\partial t} = \vec{\nabla} \times \left(\vec{u} \times \vec{B}\right) + \eta\nabla^2\vec{B} \tag{2.2}$$

derived from the Maxwell equations and Ohm's law for a moving conductor, where $\vec{u}$ is the velocity, p the pressure, $\vec{B}$ the magnetic field, ν the kinematic viscosity, ρ the density, μ_0 the magnetic permeability of free space, and $\eta \equiv 1/\mu_0\sigma$ the magnetic diffusivity, composed of the magnetic permeability and electrical conductivity.

In addition, in our operating conditions sodium is effectively incompressible:

$$\vec{\nabla} \cdot \vec{u} = 0. \tag{2.3}$$

Incompressibility holds when local density variations $\Delta\rho$ are small compared to the globally-averaged density ρ_0. These local density variations are caused by local changes in either pressure or temperature.

Local changes in pressure Δp lead to density fluctuations because of a fluid's finite compressibility β:

$$\Delta\rho/\rho_0 = \beta\Delta p.$$

In a turbulent flow, these local pressure fluctuations balance the advective term and scale as a typical velocity squared $\Delta p \sim \rho U^2$. The compressibility, in turn, is inversely related to the square of the sound speed $\beta \sim 1/\rho c^2$. Thus, the fractional change in density can be expressed:

$$\frac{\Delta\rho}{\rho_0} \sim \frac{U^2}{c^2}$$

[100]. However, even at our highest rotation rates ($\Omega \sim 100$ Hz), the maximum speed $U \approx 30$ m/s is much smaller than the sound speed of sodium, $c = 2500$ m/s, giving a maximum fractional change in local density of only $O(10^{-4})$.

Local changes in temperature lead to density fluctuations because of thermal expansion. The linear thermal expansion coefficient for sodium is roughly $10^{-5}K^{-1}$, corresponding to a 0.5% change in density per $10°C$. In our system there are small temperature variations ($< \pm 5°$) in time due to imperfect temperature regulation, which might produce local temperature gradients. At worst these temperature fluctuations would produce density fluctuations of order $O(10^{-3})$. However, even that effect is unlikely as the time scale of temperature changes is much longer than the turnover time for our system, $L/U < 1$ s.[1]

Boundary conditions

No-slip boundary conditions for the velocity apply at all surfaces.

The magnetic field boundary conditions can be deduced from the integral form of the

[1]We might wonder here about the thermal diffusive time scale, $\tau_D = L^2/\kappa \approx 5$ min., based on the thermal diffusivity $\kappa = 0.68$ cm^2/s for our system. Advective stirring, however, is much more effective at mixing temperature than diffusion.

Maxwell equations. First, we apply $\oint \vec{B} \cdot d\vec{a} = 0$ on an infinitesimally-thin Gaussian box sandwiching the interface, where $d\vec{a}$ is an area element pointing normal to the surface. Having infinitesimal area, the sides of the box intersected by the interface contribute nothing to the integral, leaving the top and the bottom surfaces. We can shrink these top and bottom surfaces until the field components along their normals are constant, leading to

$$B_{1\perp} = B_{2\perp}, \tag{2.4}$$

the requirement that the magnetic field component perpendicular to the interface be continuous, where the subscripts 1 and 2 refer to the regions on either side of the interface.

Second, we apply $\oint \vec{B}/\mu_0 \cdot d\vec{l} = I_{f,enc}$ around a rectangular loop sandwiched infinitesimally close to the interface, where $d\vec{l}$ is a displacement element. Integration along the infinitesimal loop segments perpendicular to the interface cancel because of Eqn. 2.4. The magnetic field component parallel to the surface is discontinuous because of free surface currents $I_{f,enc}$ enclosed by the integration loop. With finite conductivities, however, the surface currents are zero. Therefore,

$$\frac{1}{\mu_1}\vec{B}_{1\parallel} = \frac{1}{\mu_2}\vec{B}_{2\parallel}. \tag{2.5}$$

The materials used in our experiments are non-ferromagnetic, so the magnetic permeabilities are very nearly equal to the vacuum value, μ_0. Thus, the parallel magnetic field component $\vec{B}_{\parallel}$ is continuous too. The solution for the magnetic field outside the sphere is $\nabla^2 \vec{B} = 0$.

2.2 Dimensionless parameters

The equations of motion are often cast in dimensionless form:

$$\frac{\partial \vec{u}}{\partial t} + (\vec{u} \cdot \vec{\nabla})\vec{u} = -\vec{\nabla} p + Re^{-1}\nabla^2 \vec{u} + N\, R_m^{-1} \left(\vec{\nabla} \times \vec{B}\right) \times \vec{B}, \tag{2.6}$$

$$\frac{\partial \vec{B}}{\partial t} = \vec{\nabla} \times \left(\vec{u} \times \vec{B} \right) + R_m^{-1} \nabla^2 \vec{B} \tag{2.7}$$

where the the velocity $\vec{u}$ has been scaled by the driving speed Ωb, time by the rotational time scale Ω^{-1}, length by the outer sphere radius a, and the magnetic field $\vec{B}$ by the imposed field strength B_0. Doing so introduces the dimensionless parameters the Reynolds number Re, the magnetic Reynolds number R_m, and the interaction parameter N, which are described below. The dimensionless form makes it easier to compare systems of different scales—for instance a meter diameter sphere and a moon sized object like the Earth's core—in a meaningful way.

2.2.1 Interaction parameter

The state of the fluid flow, and thus the induced field, depends on a competition between the inertial and Lorentz forces (the second and fifth terms in Eq. 2.1). The interaction parameter quantifies this competition.

An expression for the interaction parameter can be found using dimensional analysis. Using Ohm's law $\vec{J} = \sigma(\vec{E} + \vec{u} \times \vec{B})$ (where σ is the electrical conductivity, and $\vec{E}$ the electric field) and a scaling from Faraday's law ($E_{ind} \sim U_{ind} B_{ind}$), the dimensional form of the Lorentz force per unit mass ($\vec{F} = \vec{J} \times \vec{B}/\rho$) scales as:

$$F_{Lor} \sim \frac{\sigma}{\rho} U_{ind} B_{ext} B_{ind} + \frac{\sigma}{\rho} U B_{ext}^2 \tag{2.8}$$

where ρ is the density. The second term above dominates based on two empirical observations: first because the characteristic induced field velocity $U_{ind} = L\Omega_{ind}$ is always smaller than the characteristic advective velocity $U = \Omega L$ (because the characteristic induced field frequency is always smaller than the rotation rate), and because the induced magnetic field is always at least 100 times smaller than the external magnetic field. The second term divided by the scaling of the advective term in the Navier-Stokes equation U^2/L gives the

interaction parameter: $N = B_{ext}^2 L/\eta\rho\mu_0 u$, where $\eta \equiv 1/\sigma\mu_0$ is the magnetic diffusivity, composed of the electrical conductivity and magnetic permeability. Using the outer sphere radius a, and the maximum driving speed Ωb, gives

$$N = \frac{B_{ext}^2 a}{\eta\rho\mu_0\Omega b}. \tag{2.9}$$

2.2.2 Reynolds numbers

The only other independent, adjustable dimensionless parameter is the magnetic Reynolds number, $R_m \equiv UL/\eta$. We define R_m using the sphere radius and driving speed

$$R_m \equiv \Omega b a/\eta. \tag{2.10}$$

The magnetic Reynolds number quantifies the ratio of field advection (twisting, stretching, etc.) to resistive diffusion.

The (hydrodynamic) Reynolds number, $Re \equiv \Omega b a/\nu$, is related to the magnetic Reynolds number by the ratio of kinematic viscosity to magnetic diffusivity. This ratio, known as the magnetic Prandtl number $Pr_m \equiv \nu/\eta$, is a property of the fluid. For sodium at 120° C, this number is small ($Pr_m = 8.3 \times 10^{-6}$), meaning flows with $R_m > 1$ will be highly turbulent ($Re > 10^5$).

2.2.3 Other dimensionless numbers

The radius ratio $\epsilon = r_{inner}/r_{outer}$ is a third, independent dimensionless parameter that is adjustable but which remains fixed for our experiments. Our value, $\epsilon = 0.33$, was chosen to be close to the value for the Earth.

Other dimensionless numbers can be formed from the Reynolds numbers and interaction parameter. One such number is the Lundquist number, $S = \sqrt{NR_m}$, which is commonly used to make the applied field dimensionless. Unlike the interaction parameter,

the Lundquist number,

$$S = \frac{Ba}{\eta\sqrt{\rho\mu_0}},$$

is linear in applied field. The Lunquist number is a type of Reynolds number where the velocity scale is the Alfvén velocity, $v_a = B/\sqrt{\rho\mu_0}$ —the group velocity of Alfvén waves. Alfvén waves are transverse inertial waves that propagate in the direction of the magnetic field, with magnetic tension providing the restoring force (see Sect. 2.3.1). The Lundquist number is the ratio of the Alfvén period $\tau_A = L/v_A$ to the resistive decay time $\tau = \rho/B^2\sigma$. For $S \sim 1$, system-size magnetic field oscillations within the sodium damp in about one period; shorter wavelengths are damped more strongly.

2.3 The Lorentz force

The Lorentz force is $\vec{F} = \vec{J} \times \vec{B}$. In our experiment we do not measure currents, so we can more usefully rewrite it using Ampére's law (Eqn. A.11) in terms of $\vec{B}$ alone, as we did in Eqn. 2.1:

$$\vec{F} = \frac{1}{\mu_0}\left(\vec{\nabla} \times \vec{B}\right) \times \vec{B}.$$

It is useful to write the magnetic field as a sum of a constant applied field $\vec{B}_{ext}$ and an induced field $\vec{b}$, where we assume (as seen in our experiments) that $|\,\vec{b}\,| \ll |\,\vec{B}\,|$. Neglecting terms quadratic in $|\,\vec{b}\,|$ and using $\vec{\nabla} \times \vec{B}_{ext} = 0$ the Lorentz force thus becomes:

$$\vec{F} = \frac{1}{\mu_0}\left(\vec{\nabla} \times \vec{b}\right) \times \vec{B}_{ext}. \tag{2.11}$$

2.3.1 Magnetic tension and pressure

Using vector identity A.3, that the applied field $\vec{B}_{ext}$ is curl- and gradient- free, and that magnetic fields are divergenceless, the Lorentz force (Eqn. 2.11) can be written:

$$\vec{F} = \frac{1}{\mu_0}\left[\left(\vec{B}_{ext} \cdot \vec{\nabla}\right)\vec{b} - \vec{\nabla}\left(\vec{B}_{ext} \cdot \vec{b}\right)\right]. \tag{2.12}$$

Parameter:	Re	R_m	N	S
Definition	$\frac{UL}{\nu}$	$\frac{UL}{\eta}$	$\frac{B^2 L}{U\eta\rho\mu_0}$	$\frac{BL}{\eta(\mu_0\rho)^{1/2}}$
Range for experiment	1×10^5– 1×10^7	1-25	0-50	0-10
Estimate for Earth	$\sim 10^8$	~ 100	$\sim 10^5 - 10^7$	$\sim 10^3 - 10^5$
Estimate for Sun	$\sim 10^2 - 10^{11}$	$\sim 10^2 - 10^4$	$\sim 1 - 10^4$	$\sim 10 - 10^4$

Table 2.1: Relevant dimensionless parameters. Parameter estimates for the Earth use the westward drift rate of field patterns ($U \approx 10^{-4}$ m/s) for the velocity and $B = 5$ G (radial component at core-mantle boundary) to $B = 500$ G (estimated toroidal component) for the magnetic field. Density, electrical conductivity, kinematic viscosity, and length scale of the fluid core are taken from Ref. [85].

The second term, being a gradient of a scalar, acts on the fluid in exactly the same way as the pressure term $-\vec{\nabla}p$. It's irrotational and thus does not enter into the vorticity equation (see next section). This implies that it does not influence the system dynamics, as closed flows can be described as a sum of vortices.

The first term in Eqn. 2.12 can be rewritten in terms of curvilinear coordinates:

$$\left(\vec{B}_{ext} \cdot \vec{\nabla}\right) \vec{b} = B\frac{\partial b}{\partial s}\hat{e}_t - \frac{bB}{R}\hat{e}_n.$$

Here b and B are magnitudes, $\hat{e}_t$ and $\hat{e}_n$ are unit vectors in the directions tangential and normal to the external field, s is a streamwise coordinate, and R is the local radius of curvature of the streamline. Thus, there are force components tangent to and perpendicular to the flux tubes. It is as though the magnetic field lines are in tension. If a region of conducting fluid moves across the field lines, the field lines will be swept along and the resulting curvature will create a restoring force $B^2/\mu_0 R$ on the fluid.

Two important points arise. First, in an incompressible fluid, an applied field will suppress velocity gradients in the direction of the field. Second, we see the possibility for propagating disturbances (Alfvén waves) in an electrically conducting fluid permeated by magnetic fields, analogous to waves along a taut string. These Alfvén waves will be underdamped (that is, the magnetic fields won't decay too quickly) if the Lundquist number S is greater than one.

The tension and pressure correspond to the two terms of the Maxwell electromagnetic stress tensor:

$$M_{ij} \equiv \frac{B_i B_j}{\mu_0} - \frac{B_i B_j}{2\mu_0}\delta_{ij}, \tag{2.13}$$

where δ_{ij} is the Kronecker delta function[2]. Taking the divergence of the Maxwell stress

[2]The electric field makes a negligible contribution to the stress because the flow velocity is much slower than the speed of light.

tensor gives the Lorentz force. The Maxwell stress tensor is generally used in place of the Lorentz force in the MRI literature.

2.4 Analogies with the induction and vorticity equations

The first term in the Lorentz force (Eqn. 2.12) can be rewritten using another vector identity (A.4) to give:

$$\vec{F} = \frac{1}{\mu_0}\left[\vec{\nabla}\times\left(\vec{b}\times\vec{B}_{ext}\right) - \vec{\nabla}\left(\vec{B}_{ext}\cdot\vec{b}\right)\right]. \tag{2.14}$$

Now this first term looks like the first term in the induction equation, with $\vec{u}$ replaced with $\vec{b}$. This similarity will prove useful when we decompose the velocity and magnetic fields into spherical harmonics. Velocity disturbance modes that interact with the applied field (according to the induction equation) will produce a magnetic disturbance mode that, in turn, interacts (through the Lorentz force) with the velocity disturbance, setting the stage for instabilities to form.

If we take the curl of the momentum equation:

$$\vec{\nabla}\times\left(\frac{\partial\vec{u}}{\partial t} + (\vec{u}\cdot\vec{\nabla})\vec{u} = Re^{-1}\nabla^2\vec{u} + N\ R_m^{-1}\left[\vec{\nabla}\times\left(\vec{b}\times\vec{B_{ext}}\right) - \vec{\nabla}\left(\vec{B_{ext}}\cdot\vec{b}\right)\right]\right)$$

and define the vorticity $\vec{\omega} \equiv \vec{\nabla}\times\vec{v}$ we obtain the vorticity equation:

$$\frac{\partial\vec{\omega}}{\partial t} = \vec{\nabla}\times(\vec{u}\times\vec{\omega}) + Re^{-1}\nabla^2\vec{\omega} + N\ R_m^{-1}\ \vec{\nabla}\times\vec{\nabla}\times\left(\vec{b}\times\vec{B}_{ext}\right). \tag{2.15}$$

The second term above was obtained through use of the identities A.1 and A.3.

The vorticity equation looks like the induction equation with the magnetic field $\vec{B}$ replaced by the vorticity $\vec{\omega}$ and with an additional Lorentz force source term. The analogy is not perfect, as $\vec{\omega}$ depends functionally on $\vec{u}$ in a way that $\vec{B}$ does not.

Note that in taking the curl, the hydrodynamic pressure term $-\vec{\nabla}p$ and the magnetic pressure term $\vec{\nabla}\left(\vec{B}\cdot\vec{b}\right)$, being gradients of scalars, both vanish because of identity A.1.

As noted earlier, their absence for the vorticity equation implies that neither can influence the flow field.

A third analogy to hydromagnetic flow exists with viscoelastic (polymeric) fluids; this connection has been analyzed recently by Ogilvie and Proctor [79]. As mentioned in Sect. 2.3.1, magnetic fields act as lines of tension coupled to the fluid, provided the time scale of the flow is faster than the diffusive time (i.e., R_m is greater than unity). Likewise, polymers can also act as lines of elastic tension coupled to the fluid provided the time scale of the flow is faster than the relaxation time of the polymer (i.e., a dimensionless number analogous to the Reynolds number, the Deborah number, is larger than unity). This analogy becomes exact in the limit of the magnetic Reynolds and Deborah numbers going to infinity. Formally, the analogy is made using the Oldroyd-B stress tensor (a widely used model for viscoelastic fluids) and the Maxwell electromagnetic stress tensor, which we saw in the previous section.

As might be expected, and as shown by Ogilvie and Proctor, an instability in a polymeric flow exists that is directly analogous to the MRI in hydromagnetic flows. Though not investigated here, analogous experiments to those in this dissertation, with a water-polymer mixture replacing the sodium, might be an interesting avenue for future research.

2.5 Spherical harmonics

The equations of motion (Eqns. 2.1, 2.2) are far too complicated to solve for the velocity or magnetic fields arithmetically, except in rare cases. So in a divide-and-conquer style approach, often the fields are decomposed into orthogonal modes. In spherical geometries these modes are the spherical harmonics, Y_l^m. The Earth's field is decomposed into spherical harmonics, as are the fields in many numerical geodynamo models and other

numerical simulations in spherical geometries. Motivated by the same reasons—and to make it easier for numericists and geophysicists to compare with our data—we use the spherical harmonics to decompose our induced field too. We'll see how in Chapters 3. Here we first provide some mathematical details.

The spherical harmonics are the angular parts of the solutions to Laplace's equation ($\nabla^2\psi = 0$) in spherical polar coordinates [64]. (They work as a basis in our experiment because there are no currents outside our vessel and the magnetic field satisfies Laplace's equation.) The spherical harmonics are related to the associated Legendre polynomials, P_l^m:

$$Y_l^m = P_l^m(\cos\theta)\, e^{im\phi}. \tag{2.16}$$

Each harmonic has a "degree" l and "order" or "azimuthal wave number" m.

The spherical harmonics are scalars, whereas the velocity and magnetic fields are vectors. Following the convention of Bullard and Gellman [7], we decompose the magnetic and velocity fields using the toroidal modes:

$$T_r = 0, \quad T_\theta = \frac{T(r,t)}{r\sin\theta}\frac{\partial Y_l^m}{\partial\phi}, \quad T_\phi = \frac{-T(r,t)}{r}\frac{\partial Y_l^m}{\partial\theta}, \tag{2.17}$$

which are each the curl of a radial vector, $\vec{T}_l^m = \vec{\nabla}\times T(r,t)Y_l^m(\theta,\phi)\hat{r}$, and the poloidal modes:

$$S_r = \frac{n(n+1)}{r^2}S(r,t)Y_l^m, \quad S_\theta = \frac{1}{r}\frac{\partial S(r,t)}{\partial r}\frac{\partial Y_l^m}{\partial\theta}, \quad S_\phi = \frac{1}{r\sin\theta}\frac{\partial S(r,t)}{\partial r}\frac{\partial Y_l^m}{\partial\phi}, \tag{2.18}$$

which are each the curl of a $\vec{T}$-like vector, $\vec{S}_l^m = \vec{\nabla}\times\vec{\nabla}\times S(r,t)Y_l^m(\theta,\phi)\hat{r}$. We separate the nonaxisymmetric modes into their real and imaginary parts—that is by their azimuthal dependence, $\cos m\phi$ or $\sin m\phi$, denoted by adding c or s after m. (When c or s is omitted, the azimuthal dependence is not important there.) For clarity, v or b will be added after

l to specify which field, velocity or magnetic, the mode represents. Putting this together in an example: $\vec{S}_{2v}^{1c}$ is the $l = 2$ velocity mode with the azimuthal dependence $\cos\phi$.

The radial functions $S(r,t)$ and $T(r,t)$ above are in general different for each mode, and fully specify the time dependence. For the special case where the fields satisfy Laplace's equation (such as outside our vessel), the radial modes correspond to $T(r) = 0$, $S(r) \propto r^{-n}$.

Properties of $\vec{S}$ and $\vec{T}$

The vectors $\vec{S}_l^m$ and $\vec{T}_l^m$ are both divergenceless (as they must to compose magnetic and incompressible velocity fields). $\vec{S}_l^m$ and $\vec{T}_l^m$ also form a basis, and are orthogonal when integrated over the surface of a sphere:

$$\iint \vec{T}' \cdot \vec{T} d\sigma = \iint \vec{S}' \cdot \vec{S} d\sigma = 0$$

when $\vec{S} \neq \vec{S}'$ and $\vec{T} \neq \vec{T}'$. This orthogonality is directly due to the orthogonality of the scalar spherical harmonics, so here the functions are orthogonal if they differ only in their radial dependence. Also, for all $\vec{S}$ and all $\vec{T}$

$$\iint \vec{S} \cdot \vec{T} d\sigma = 0,$$

even if based on the same spherical harmonic. (Note that $d\sigma \equiv r^2 sin\theta d\theta d\phi$ used here and throughout the chapter is a differential area element and is of course unrelated to the electrical conductivity σ.)

For non-orthogonal modes based on the same harmonic then:

$$\begin{aligned}
&\iint \vec{T}' \cdot \vec{T} d\sigma = N_l T(r) T'(r), \\
&\iint \vec{S}' \cdot \vec{S} d\sigma = N_n \left[l(l+1) S(r) S'(r)/r^2 + \frac{dS(r)}{dr} \frac{dS'(r)}{dr} \right],
\end{aligned} \tag{2.19}$$

where

$$\begin{aligned}
N_l &= \frac{2\pi l(l+1)}{2l+1} \frac{(l+m)!}{(l-m)!} \quad \text{if } m \neq 0, \\
N_l &= \frac{4\pi l(l+1)}{2l+1} \quad \text{if } m = 0.
\end{aligned}$$

The $\vec{S}$'s and $\vec{T}$'s are related to each other:

$$\left.\begin{aligned}
&\vec{\nabla} \times \vec{T} = \vec{S}', \\
&\vec{\nabla} \times \vec{\nabla} \times \vec{T} = \vec{\nabla} \times \vec{S}' = \vec{T}^*, \\
&\vec{\nabla} \times \vec{\nabla} \times \vec{S} = \vec{S}^*,
\end{aligned}\right\} \tag{2.20}$$

where $\vec{S}'$ is $\vec{S}$ with $T(r,t)$ in place of $S(r,t)$, as we saw from their definitions, and furthermore, $\vec{T}^*$ and $\vec{S}^*$ are $\vec{T}$ and $\vec{S}$ with $S(r,t)$ and $T(r,t)$ replaced by

$$\left.\begin{aligned}
T^*(r,t) &= -\frac{d^2T}{dr^2} + \frac{l(l+1)}{r^2} T, \\
S^*(r,t) &= -\frac{d^2S}{dr^2} + \frac{l(l+1)}{r^2} S.
\end{aligned}\right\} \tag{2.21}$$

Induction Equation

Again following the example of Bullard and Gellman, we can find an equation governing each magnetic field mode. First, rewrite the induction equation by expanding the velocity and magnetic fields in $\vec{S}$ and $\vec{T}$. Then project these equations onto the "test" modes $\vec{S}'_\gamma$ and $\vec{T}'_\gamma$, whose radial functions are unity for all r, and integrate over a sphere of radius r to give (after using identity A.2 and Eqns. 2.20, 2.21):

$$\left.\begin{aligned}
r^2 \frac{\partial S_\gamma}{\partial t} &= r^2 \frac{\partial^2 S_\gamma}{\partial r^2} - \gamma(\gamma+1) S_\gamma - \iint \vec{S_\gamma}' \cdot \vec{\nabla} \times \left(\vec{v_\beta} \times \vec{B_\alpha} \right) \sin\theta \, d\theta \, d\phi, \\
r^2 \frac{\partial T_\gamma}{\partial t} &= r^2 \frac{\partial^2 T_\gamma}{\partial r^2} - \gamma(\gamma+1) T_\gamma - \iint \vec{T_\gamma}' \cdot \vec{\nabla} \times \left(\vec{v_\beta} \times \vec{B_\alpha} \right) \sin\theta \, d\theta \, d\phi.
\end{aligned}\right\} \tag{2.22}$$

where $\vec{v_\beta} = \vec{S_\beta} + \vec{T_\beta}$ and $\vec{B_\alpha} = \vec{S_\alpha} + \vec{T_\alpha}$, and S_γ and T_γ are the radial functions. When γ stands alone (not as a suffix) it represents the mode order. The suffixes implicitly contain l,m, and c or s. Furthermore, β always corresponds to the inducing velocity, α the background field being acted on by the velocity, and γ the resulting induced field.

The integrals in Eqn. 2.22 can be made to depend on one of the following two integrals:

$$\left.\begin{aligned} K_{\alpha\beta\gamma} &= \iint Y_\alpha Y_\beta Y_\gamma \sin\theta \, d\theta \, d\phi, \\ L_{\alpha\beta\gamma} &= \iint Y_\alpha \left(\frac{\partial Y_\beta}{\partial \theta} \frac{Y_\gamma}{\partial \phi} - \frac{\partial Y_\beta}{\partial \phi} \frac{Y_\gamma}{\partial \theta} \right) d\theta \, d\phi. \end{aligned}\right\} \tag{2.23}$$

We can then rewrite the induction equation as:

$$\left.\begin{aligned} \frac{\partial S_\gamma}{\partial t} &= \frac{\partial^2 S_\gamma}{\partial r^2} - \frac{\gamma(\gamma+1)}{r^2} S_\gamma - \frac{V}{r^2} \sum_{\alpha,\beta} \quad [(S_\alpha S_\beta S_\gamma) + (T_\alpha S_\beta S_\gamma) + (S_\alpha T_\beta S_\gamma)], \\ \frac{\partial T_\gamma}{\partial t} &= \frac{\partial^2 T_\gamma}{\partial r^2} - \frac{\gamma(\gamma+1)}{r^2} T_\gamma - \frac{V}{r^2} \sum_{\alpha,\beta} \quad [(S_\alpha S_\beta T_\gamma) + (T_\alpha S_\beta T_\gamma) + (T_\alpha T_\beta T_\gamma) \\ &\qquad\qquad\qquad\qquad\qquad\qquad\qquad\qquad +(S_\alpha T_\beta T_\gamma)]. \end{aligned}\right\} \tag{2.24}$$

where $(S_\alpha S_\beta S_\gamma)$, $(T_\alpha S_\beta T_\gamma)$, and $(S_\alpha T_\beta T_\gamma)$ depend on $K_{\alpha,\beta,\gamma}$; $(T_\alpha S_\beta S_\gamma)$, $(S_\alpha T_\beta S_\gamma)$, $(S_\alpha S_\beta T_\gamma)$, and $(T_\alpha T_\beta T_\gamma)$ depend on $L_{\alpha,\beta,\gamma}$; and V is a constant. These terms are related to the Wigner 3-j symbols used in quantum mechanical systems having coupled angular momenta, and they follow the same selection rules. We'll present these selection rules in Sect. 2.5.1. A sampling of these terms, taken from Bullard and Gellman [7], are shown below:

$$\begin{aligned} (S_\alpha S_\beta S_\gamma) &= -\frac{K_{\alpha\beta\gamma}}{2N_\gamma} \Big[\alpha(\alpha+1) \{\alpha(\alpha+1) - \beta(\beta+1) - \gamma(\gamma+1)\} S_\alpha \frac{\partial S_\beta}{\partial r} \\ &\qquad + \beta(\beta+1)\{\alpha(\alpha+1) - \beta(\beta+1) + \gamma(\gamma+1)\} \frac{\partial S_\alpha}{\partial r} S_\beta \Big], \\ (T_\alpha S_\beta S_\gamma) &= -\frac{L_{\alpha\beta\gamma}}{N_\gamma} \beta(\beta+1) T_\alpha S_\beta, \\ (S_\alpha T_\beta S_\gamma) &= -\frac{L_{\alpha\beta\gamma}}{N_\gamma} \alpha(\alpha+1) S_\alpha T_\beta. \end{aligned} \tag{2.25}$$

Each term in Eqn. 2.24 has a simple physical interpretation. The terms on the left side are the rate of growth; the first two terms on the right side give diffusion. The remain-

ing "field-generating" terms give the rate of growth from the magnetic field component $\vec{B}_\alpha = \vec{S}_\alpha + \vec{T}_\alpha$ interacting with the velocity mode $\vec{v}_\beta = \vec{S}_\beta + \vec{T}_\beta$ to produce $\vec{B}_\gamma = \vec{S}_\gamma + \vec{T}_\gamma$.

Momentum equation

We can perform a similar analysis with the momentum equation. Again we expand the magnetic and velocity fields into poloidal modes. First we rewrite the advective term $(\vec{u}\cdot\vec{\nabla})\vec{u}$ using identity A.3 to get

$$\vec{\nabla}\left(u^2\right)/2 - \vec{u}\times\left(\vec{\nabla}\times\vec{u}\right).$$

We use Eqn. 2.14 for the Lorentz force. To begin we have:

$$\frac{\partial\vec{u}}{\partial t} + \frac{\vec{\nabla}\left(\vec{u}\cdot\vec{u}\right)}{2} - \vec{u}\times\left(\vec{\nabla}\times\vec{u}\right) = -\vec{\nabla}p + \frac{\nabla^2\vec{u}}{Re} + \frac{N}{R_m}\left[\vec{\nabla}\times\left(\vec{b}\times\vec{B}_{ext}\right) - \vec{\nabla}\left(\vec{b}\cdot\vec{B}_{ext}\right)\right] \quad (2.26)$$

As with the induction equation, we expand the velocity and magnetic fields in $\vec{S}$ and $\vec{T}$ and then multiply by $\vec{S}'_\gamma$ and $\vec{T}'_\gamma$ (modes with unity r dependence) and integrate over a sphere of radius r to obtain:

$$\frac{\partial\vec{u}_\gamma}{\partial t} - \iint \vec{S}_\gamma{}'\cdot\vec{u}\times\left(\vec{\nabla}\times\vec{u}\right)d\sigma = \frac{\nabla^2\vec{u}_\gamma}{Re} + \frac{N}{R_m}\iint\vec{S}_\gamma{}'\cdot\vec{\nabla}\times\left(\vec{b}_\beta\times\vec{S}_{\alpha=1B}\right)d\sigma \quad (2.27)$$

The three terms that are gradients of a scalar vanish. To see this, consider integrating a general divergenceless vector $\vec{S}$ projected onto the gradient of a general scalar function ψ over the surface of a sphere. After using identity A.5, we obtain:

$$\iint\vec{\nabla}\cdot\left(\psi\vec{S}\right)d\sigma.$$

From the two-dimensional divergence theorem, this surface integral reduces to a line integral enclosing the area. Our area is closed, however, so the integration path collapses to a point. Assuming $\psi\vec{S}$ is well behaved, the integral vanishes.

The last term in Eqn. 2.27, with the Lorentz force, is structurally identical to the last term in the induction equation (Eqn. 2.22), and thus can also be made to depend on the surface integrals $K_{\alpha,\beta,\gamma}$ and $L_{\alpha,\beta,\gamma}$. Here the subscripts α, β, γ will have different interpretations: b_β indicates the induced field mode that interacts with the applied field ($\vec{S}_{\alpha=1B}$) to produce velocity mode $\vec{u}_\gamma$.

Without analogy to the induction equation, there is also the nonlinear advection term, $\vec{u} \times \left(\vec{\nabla} \times \vec{u}\right)$. To decompose it, we would need to introduce two more subscripts in Eqn. 2.27, as the two occurrences of $\vec{u}$ need not be the same mode, nor the inducing velocity mode $\vec{u}_\beta$.

Boundary conditions

Earlier we showed the magnetic field must be continuous at all boundaries. Here we derive explicit boundary conditions for the individual toroidal and poloidal modes.

At the outer wall, the perpendicular magnetic field is approximately continuous with an exterior vacuum solution, as stainless steel has a conductivity that is 30 times lower than sodium. The equation governing the external fields, because there are no currents, is $\vec{\nabla} \times \vec{B} = 0$, implying that $\vec{B} = \vec{\nabla}\psi$. Since $\vec{\nabla} \cdot \vec{B} = 0$, ψ satisfies Laplace's equation ($\nabla^2\psi = 0$), which has solutions

$$\psi = \sum_{l,m} C_{l,m} r^{-(l+1)} P_l^m(\cos\theta) e^{im\phi},$$

(where we eliminated the solution that diverges as $r \to \infty$). Therefore,

$$B_{ext,r} = \sum_{l,m} -(l+1) C_{l,m} r^{-(l+2)} P_l^m(\cos\theta) e^{im\phi},$$

$$B_{ext,\theta} = \sum_{l,m} C_{l,m} r^{-(l+2)} \frac{d}{d\theta} P_l^m(\cos\theta) e^{im\phi},$$

$$B_{ext,\phi} = \sum_{l,m} C_{l,m} r^{-(l+2)} \frac{im}{\sin\theta} P_l^m(\cos\theta) e^{im\phi}.$$

Matching with the coefficients for the solution just inside the sodium then yields

$$T_l^m = 0, \quad \frac{\partial S_l^m}{\partial r} + \left(\frac{l}{r}\right) S_l^m = 0, \qquad \text{at } r = a. \tag{2.28}$$

For the boundary condition at the inner sphere, if we assume (unlike our typical case) the inner sphere is insulating, the analysis is similar. Except now the potential is bounded at $r = 0$:

$$\psi = \sum_{l,m} C_{l,m} r^l P_l^m(\cos\theta) e^{im\phi}.$$

After matching the field components inside and outside the inner sphere:

$$T_l^m = 0, \quad \frac{\partial S_l^m}{\partial r} - \left(\frac{l+1}{r}\right) S_l^m = 0 \qquad \text{at } r = b. \tag{2.29}$$

If we take the inner sphere to be conducting, then we have to solve the coupled equations for $\vec{B}$ for $r < r_i$, where the velocity is given by solid body rotation. Following the example of Hollerbach and Skinner [50], and equivalent to what we did before (see Sect. 2.2.1), we drop the time derivative in the induction equation by invoking the "low R_m" limit (though by our definition $R_m \sim 1$). In this limit, the induced field strength times the characteristic induced field frequency is much smaller than the applied field times the advective frequency; using our empirical relations for Ω_b $|\vec{b}_{ind}|$ we find this is satisfied. Symbolically, $|\vec{b}_{ind}|\Omega_b \sim (.01B)(.1\Omega) = O(10^{-3})B\Omega \ll B\Omega$. Furthermore, for solid body rotation: $\vec{\nabla} \times (\vec{u} \times \vec{B}_{ext}) = 0$. So the induction equation reduces to $\nabla^2 \vec{b} = 0$, and the solutions can be written in terms of spherical harmonics, as above. The magnetic field boundary condition at the inner sphere interface is then [49]:

$$\lambda \frac{\partial T_l^m}{\partial r} - \left(\frac{l+1}{r}\right) T_l^m = 0, \quad \lambda \frac{\partial S_l^m}{\partial r} - \left(\frac{l+1}{r}\right) S_l^m = 0, \tag{2.30}$$

where λ is the ratio of sodium's to the inner sphere's conductivities. At 120°, the conductivity of copper—the inner sphere material for most runs—is about five times greater

than sodium. The conductivity of stainless stainless steel, another inner sphere material used, is about 30 times lower.

2.5.1 Selection Rules

By examining the properties of the integrals $K_{\alpha\beta\gamma}$ and $L_{\alpha\beta\gamma}$ (Eqn. 2.23), Bullard and Gellman formulate the following spherical harmonic selection rules that describe which of the field-generating terms in the induction equation, and the analogous terms in the momentum equation for the Lorentz force, are nonzero. They become useful for us after we decompose our field: we can talk qualitatively about which modes can and cannot affect the dynamics, leaving only a few possibilities.

(1) $(S_\alpha S_\beta S_\gamma), (S_\alpha T_\beta T_\gamma), (T_\alpha S_\beta T_\gamma)$, which depend on K, are zero unless (a) to (d) are satisfied:

a) $\alpha + \beta + \gamma$ is even,

b) α, β and γ can form sides of a triangle (i.e., $\alpha \leq \beta + \gamma$, etc.),

c) one or more of the four expressions $m_\alpha \pm m_\beta \pm m_\gamma$ vanishes,

d) three of the harmonics have $\cos m\phi$ or one has ($m = 0$ counts as a cosine).

(2) $(S_\alpha T_\beta S_\gamma), (S_\alpha S_\beta T_\gamma), (T_\alpha S_\beta S_\gamma), (T_\alpha T_\beta T_\gamma)$ which depend on L, are zero unless (a) to (e) are satisfied:

a) $\alpha + \beta + \gamma$ is odd,

b) α, β and γ can form sides of a triangle (i.e., $\alpha \leq \beta + \gamma$, etc.),

c) one or more of the four expressions $m_\alpha \pm m_\beta \pm m_\gamma$ vanishes,

d) two of the harmonics have $\cos m\phi$ or one has ($m = 0$ counts as a cosine),

e) no two harmonics are identical.

(3) $(T_\alpha T_\beta T_\gamma)$ and $(T_\alpha T_\beta S_\gamma)$ are always zero.

Note that the rules do not depend on the radial functions $S(r,t)$ and $T(r,t)$.

2.5.2 Qualitative analysis

Because the induced field is much smaller than the applied field, to first order all the important modes should arise from an interaction with the applied field $\vec{S}^0_{1B}$.

Our primary magnetic field instability is dominated by the mode $\vec{S}^1_{1b}$. What velocities can induce this magnetic field? In other words what modes $\vec{S}_{\beta v}$ produce nonzero terms of the form $\vec{S}^0_{1B}\vec{S}_{\beta v}\vec{S}^1_{1b}$ and $\vec{S}^0_{1B}\vec{T}_{\beta v}\vec{S}^1_{1b}$ from Eqn. 2.24?

For poloidal velocity fields $\vec{S}^m_{\beta v}$, rule (1)a requires β be even; (1)b requires β be 2 or less; (1)c requires m_β be 1; and (1)d requires that the velocity and induced field modes be both cos-type or both sin-type. $\vec{S}^{1c,s}_{2v}$ (where we choose c or s to be the same type as the induced field) is the only mode that works. Likewise, the toroidal velocity modes that can interact with $\vec{S}^0_{1B}$ to produce the same magnetic field are limited by rules (2)a-e. Here the only allowable velocity is $\vec{T}^{1c,s}_{1v}$ (where c or s is the opposite type as the induced field).

For the momentum equation, the analysis is identical; only the interpretation of the modes changes. Thus the velocity modes that interact with the base magnetic field through the induction equation to produce a magnetic field mode will be in turn created by the interaction of that mode and the magnetic base state through the Lorentz force. This situation is diagrammed for the primary instability in Fig. 2.1.

Two empirical observations lead us to conclude that $\vec{S}^{1c,s}_{2v}$ interacting with the external field is the likely interaction producing the primary instability. First, our measurements suggest the toroidal $\vec{T}^0_{2b}$ field is $\lesssim 10\%$ the external field (*a priori* we might allow it to be R_m times larger). Second, in the primary instability the $\vec{S}^{1c,s}_{1b}$ and $\vec{S}^{1c,s}_{3b}$ modes have

identical dynamics (though the latter has a smaller amplitude). It appears both magnetic modes are caused by the same velocity mode. We must rule out $\vec{T}_{1v}^{1s,c}$ then—it cannot interact with the external field to produce $\vec{S}_{1b}^{3c,s}$.

2.6 Instabilities

An instability occurs when small perturbations from a steady state grow in time (as opposed to decay). In our case, where there are two coupled equations, an instability occurs when a velocity disturbance creates a magnetic disturbance (through the induction equation) which in turn generates more of the velocity disturbance (through the Lorentz force) in positive feedback. It seems only two modes with time varying coefficients are needed to model the essential dynamics of the system. We explore the possibility of this sort of truncated mode model next.

Before developing a model, we might first ask if an instability could form solely through the induction equation, without the Lorentz force. Indeed, from the selection rules above we find that some velocity modes—namely $\vec{S}_{2v}^{0}$ and $\vec{S}_{2v}^{2}$—can induce the field component $\vec{S}_{1b}^{1}$ back onto itself. An arbitrarily small $\vec{S}_{1b}^{1}$ field component could thus in principle be amplified by a preexisting $\vec{S}_{2v}^{0}$ velocity mode to become a magnetic instability, without necessarily producing a corresponding velocity disturbance (and thus we could disregard the momentum equation).

Sadly, we must rule out this possibility. It describes a dynamo, which we have not observed! The applied field is necessary to see our instabilities. Also, we empirically observe velocity fluctuations (with ultrasound) when the induced magnetic field instability is observed, further implicating the Lorentz force and the importance of the momentum equation. Incidentally, $\vec{S}_{2v}^{0}$ *is* a mode we expect as part of our base velocity state. It

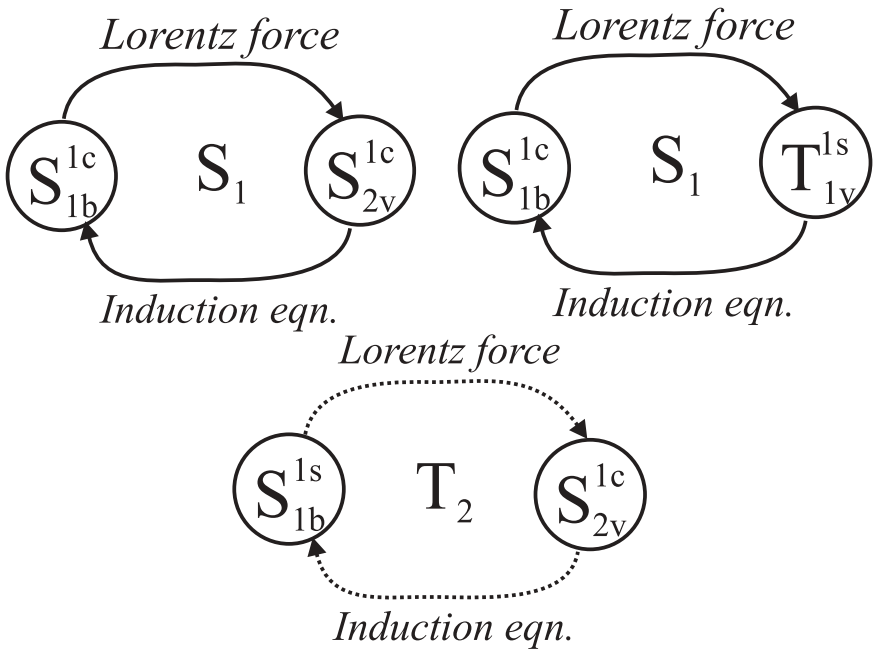

Figure 2.1: Diagram of all possible mode interactions involving the base magnetic field modes, $\vec{S}^0_{1B}$ or $\vec{T}^0_{2B}$, and the magnetic field disturbance of the primary instability $\vec{S}^1_{1b}$. Connections exist between two modes if they interact, through the Lorentz force or the induction equation, as determined by the selection rules. Three more interactions exist above except with c replaced by s and vice versa. The velocity mode $\vec{T}^0_{1v}$ (simple rotation) converts c to s and gives rise to precessing velocity and magnetic field disturbances.

consists of outflow at the equator and return flow at each pole, and should be generated by Ekman boundary layers at the inner sphere boundary.

Since we don't see a dynamo, we expect the dominant interactions to involve the applied field, which means we consider interactions coupled through the induction and momentum equations.

2.6.1 A truncated mode model

We start with the empirical observation that the primary magnetic field instability is dominated by $\vec{S}^1_{1b}$. Our velocity measurements, being along one chord, cannot determine the modal structure of the velocity disturbance. In Sect. 2.5.2, however, we argued that this disturbance is $\vec{S}^1_{2v}$. The background velocity state, neglecting turbulence, should be a combination of $\vec{T}^0_{1v}$ (simple rotation) and $\vec{S}^0_{2v}$ (outflow at the equator, return flow at the poles). For the sake of a simple model, we'll neglect $\vec{S}^0_{2v}$, as it should be substantially weaker than $\vec{T}^0_{1v}$.[3] The background magnetic field state is $\vec{S}^0_{1B}$, with $\vec{S}^0_{1B}(r) = \sqrt{\pi/3}\, r^2$ to give a constant magnetic field vector of unity magnitude in $\hat{z}$, the rotation axis.

With these assumptions, the induction equation after projecting onto $\vec{S}^{1\prime}_1$ and integrating over a sphere of radius r (Eqn. 2.22) becomes:

$$R_m r^2 \frac{\partial S^{1c,s}_{1b}}{\partial t} = r^2 \frac{\partial^2 S^{1c,s}_{1b}}{\partial r^2} - 2S^1_{1b} - V\left(S^{1c,s}_{1b} S^{1c,s}_{2v} S^0_{1B} + S^{1c,s}_{1b} T^0_{1v} S^{1s,c}_{1b}\right), \tag{2.31}$$

Likewise, the momentum equation becomes:

$$\begin{aligned} \frac{\partial S^1_{2v}}{\partial t} - \oint \vec{T}_{1v} \times \left(\vec{\nabla} \times \vec{S}^1_{2v}\right) d\sigma + \oint \vec{S}^1_{2v} \times \left(\vec{\nabla} \times \vec{T}_{1v}\right) d\sigma \\ = \frac{\nabla^2 S^1_{2v}}{Re} + \frac{N}{R_m} \oint \vec{\nabla} \times \left(\vec{S}^1_{1b} \times \vec{S}_{1B}\right) d\sigma \end{aligned} \tag{2.32}$$

After integrating the terms above, we are left with two coupled PDEs in the radial functions, which are also functions of time. Alternatively, we could assume functional forms

[3] From preliminary observations of a water-Kalliroscope spherical Couette experiment recently built in the lab, this assumption of the background velocity state appears valid [21].

for the radial functions, $S^1_{1b}(r)$ and $S^1_{2v}(r)$, and be left with two coupled ODEs.

Because we are looking for magnetically-induced instabilities, it is important that the base velocity state $\vec{T}^0_{1v}$ be centrifugally stable, else the base state might be unstable for zero applied field. We chose $T^0_{1v}(r)$ so that $\vec{u} = \sin\theta$ at $r = b$, and $\hat{\phi} \cdot \vec{T}^0_{1v} \sim r^{-3/2}$ at $\theta = 90°$, to match as closely as possible our experimentally determined profile.

We numerically solved these PDEs using MATHEMATICA for given values of R_m and S, and small initial values of $S^1_{1b}(r, 0)$ and $S^1_{2v}(r, 0)$. If after 100 turnover times the solutions decayed and remained close to zero, we determined that that pair of R_m and S were stable. If the solution grew exponentially, then the solution was unstable. In this way we've explored the (S, R_m) plane and found, in qualitative agreement with our observations, that the system is stable below some threshold Lundquist number S_c and unstable above it. However, we were unable to produce a suppression of the instability at large applied field. Furthermore, the critical Lundquist number was typically $S_c \approx 10$, which was larger than our experimental value of $S_c \approx 1$.

It should be noted that $T^0_{1v}(r)$ is a function of spherical radius, while our background flow—even neglecting poloidal motions—likely has three qualitatively distinct flow regions defined by $s \equiv r \sin\theta$: both above and below the sphere inside the tangent cylinder, and outside the tangent cylinder. We might try modifying our base state; we leave this for a future project. Kitchatinov and Rüdiger [59] performed a stability analysis using a cylindrical base state in a spherical geometry, and using spherical harmonic perturbations. They found stability diagrams that looked remarkably similar to the WKB diagrams of Ji et al., which in turn share important features with our data. Kitchatinov and Rüdiger used a magnetic Prandtl number of $Pm = 1$. We'll review the WKB calculation shortly.

2.6.2 Stability and Rayleigh criterion

In theoretical and numerical work, the magnetorotational instability is found to develop from flows that are centrifugally stable. Keplerian flows (e.g., accretion disks), where the MRI is important, are also centrifugally stable. A rotating flow is centrifugally stable if fluid particles perturbed from their orbit return to their original trajectory. This condition is met, as first shown by Rayleigh in 1917, if the specific angular momentum increases outward with cylindrical radius s:

$$\frac{d(s^2\Omega(s))^2}{ds} > 0, \tag{2.33}$$

where $\Omega(s) = v_\phi/s$ here is the azimuthal angular velocity profile (not to be confused with Ω the inner sphere rotation rate). The angular momentum, $s^2\Omega(s)$, is squared above so that the criterion does not depend on the direction of rotation. This criterion only applies to axisymmetric disturbances and inviscid flows. Including viscosity, flows unstable by Rayleigh's criterion could still be stable. Rayleigh stable flows are stable regardless of viscosity.

In the MRI literature, rotation profiles are commonly characterized by the index $\zeta \sim 2 + d \ln \Omega(s)/d \ln s$. The Rayleigh criterion is satisfied when $\zeta > 0$. For Keplerian flows, $\zeta = 1/2$. Profiles with $0 < \zeta < 2$ are predicted to be MRI-unstable, assuming a laminar base state. Our time-averaged profiles are found to be in the range $0.4 < \zeta < 0.6$. However, unlike the base states used in theoretical studies, our velocity base state has boundary layers and poloidal motions. Still, as we will see later, our phase diagrams our qualitatively, if not quantitatively, similar to the theoretically predicted phase diagrams despite these differences.

2.6.3 WKB Method

Another way to attempt a stability description of our system is through a WKB method. Here we review a calculation performed by Ji, Goodman, and Kageyama [53] for a cylindrical geometry and adapt it to our system. Their method assumes axisymmetric perturbations proportional to $\exp(\gamma t - ik_s s - ik_z z)$, so that k_s and k_z are radial and axial wavenumbers, and γ is the growth rate. In cylindrical coordinates, their base state is $\vec{v}_0 = (0, \Omega s, 0)$, $\vec{B}_0 = (0, 0, B)$, where Ω is a function of radius characterized by the index ζ (same as in previous section).

From the linearized equations of motion, Ji et al. find the following dispersion relation:

$$\left[(\gamma + \nu k)(\gamma + \eta k) + (k_z V_A)^2\right]^2 \frac{k^2}{k_z^2} + 2\Omega^2 \zeta \left(\gamma + \eta k^2\right)^2 + 2\Omega^2(\zeta - 2)(k_z V_A)^2 = 0.$$

Three relevant frequencies appear: a resistive frequency $\omega \equiv \eta k^2$, a viscous frequency $\omega_\nu \equiv \nu k^2$, and an Alfvénic frequency $\omega_A \equiv |\, k_z V_A \,|$, composed of the Alfvén velocity $V_A \equiv B/\sqrt{\rho\mu_0}$. In terms of these frequencies:

$$\left[\left(\frac{\gamma}{\omega_\eta} + \frac{\omega_\nu}{\omega_\eta}\right)\left(\frac{\gamma}{\omega_\eta} + 1\right) + \frac{\omega_A^2}{\omega_\eta^2}\right]^2 \frac{k^2}{k_z^2} + 2\zeta \frac{\Omega^2}{\omega_\eta^2}\left(\frac{\gamma}{\omega_\eta} + 1\right)^2 + 2(\zeta - 2)\frac{\Omega^2}{\omega_\eta^2}\frac{\omega_A^2}{\omega_\eta^2} = 0.$$

Ji et al. define three relevant dimensionless numbers: $P_m \equiv \omega_\nu/\omega_\eta$, $S \equiv \omega_A/\omega_\eta$, and $R_m \equiv \Omega/\omega_\eta$. In terms of these numbers and the normalized growth rate ($\gamma/\omega_\eta \to \gamma'$):

$$\left[\left(\gamma' + P_m\right)\left(\gamma' + 1\right) + S^2\right]^2 (1 + \epsilon^2) + 2\zeta R_m^2(\gamma' + 1)^2 - 2(2 - \zeta)R_m^2 S^2 = 0, \qquad (2.34)$$

where a geometry factor $\epsilon = h/(s_2 - s_1)$, composed of the height and radius difference, relates the wave numbers in the radial and axial direction, $k = k_z\sqrt{1 + \epsilon^2}$.

Ji et al. show that the necessary and sufficient condition for stability is that the

dispersion relation remain positive at $\gamma' = 0$:

$$(P_m + S^2)^2(1+\epsilon^2) + 2\zeta R_m^2 - 2(2-\zeta)R_m^2 S^2 \geq 0. \tag{2.35}$$

Their dimensionless numbers depend on both k and the ratio k_z/k_r, so linking them to our experimental parameters requires some assumptions. In the remainder of this paragraph, we denote their dimensionless parameters with primes to distinguish them from ours. First, we take the maximum fluid rotation rate in the dispersion relation Ω' to be the empirically-derived fluid rotation just outside our inner boundary layer $\Omega/3$, where Ω is the inner sphere rotation rate. If we take $ka = 1$ and assume that k is entirely in the $\hat{z}$ direction ($\epsilon = 0$), then the dimensionless numbers in the dispersion relation agree with our parameters exactly.[4] If we take $ka = 2$, then $S' \to 2S$, $R'_m \to 4R_m$ and we get a new stability relation for an instability with a wave number that is twice as large. Both stability curves are shown in Fig. 2.2. Our secondary instabilities have larger wavenumbers than the primary instability, so we might expect our experimental stability phase diagram to share qualitative features to the shapes shown. For instance, at a given Ω the system is stable at zero fields, turns unstable at a finite applied field if Ω not too small, turns unstable to higher wavenumber modes at larger applied field, and then becomes stable again at large applied field. In Chapter 4 we'll see these very features, and that there is also some quantitative agreement.

Note that this WKB analysis assumed axisymmetric perturbations. In our experiment, the instabilities are nonaxisymmetric. This difference can be understood by contrasting the different symmetries of the base states. In the cylindrical case, the base state is unchanged by an axial translation. Such situations generically show instabilites

[4] Actually, P'_m has no k dependence and agrees no matter the assumptions. Incidentally, the stability is least sensitive is changes in P_m because, at $O(10^{-5})$ as it is for us, it becomes negligible in Eqn. 2.35.

to axially periodic patterns, and are known to do so for the MRI [58, 76]. Our base state, occuring in a spherical geometry, lacks that axial symmetry, but has approximate rotational and reflectional symmetry. In these situations, instabilities generically involve rotating non-axisymmetric patterns—that is, Hopf bifurcations [62].

2.6.4 Bifurcation theory

A bifurcation, in dynamical system theory, is a qualitative change in a system's dynamics that occurs when a control parameter is increased past a critical value. Bifurcations occur in a diverse range of systems, and a considerable amount of theory has been developed to analyze them [81, 98, 41]. We review some of this theory here, in the process connecting our experiment to other systems and ultimately explaining some important features of our data.

Consider a two dimensional phase space governed by two real, first order differential equations:

$$\begin{aligned} x' &= f(x, y, \beta), \\ y' &= g(x, y, \beta), \end{aligned} \tag{2.36}$$

where x and y are phase variables, x' and y' their time derivatives, and β a control parameter. If we linearize this system around a fixed point $\vec{X}^* = (x^*, y^*)$, defined by $\vec{X}^* \equiv \vec{X}' = 0$, we can characterize the solution near $\vec{X}^*$ by the eigenvalues of the Jacobian matrix at $\vec{X}^*$:

$$\mathbf{J} = \begin{pmatrix} \frac{\partial f}{\partial x} & \frac{\partial f}{\partial y} \\ \frac{\partial g}{\partial x} & \frac{\partial g}{\partial y} \end{pmatrix}_{\vec{X}^*}.$$

$\mathbf{J}$ depends on β and consists of only real numbers (as opposed to functions), and thus the eigenvalues depend on β and are either both real or complex conjugates. In either case the real parts of the eigenvalues determine the stability near the fixed point: stable if both

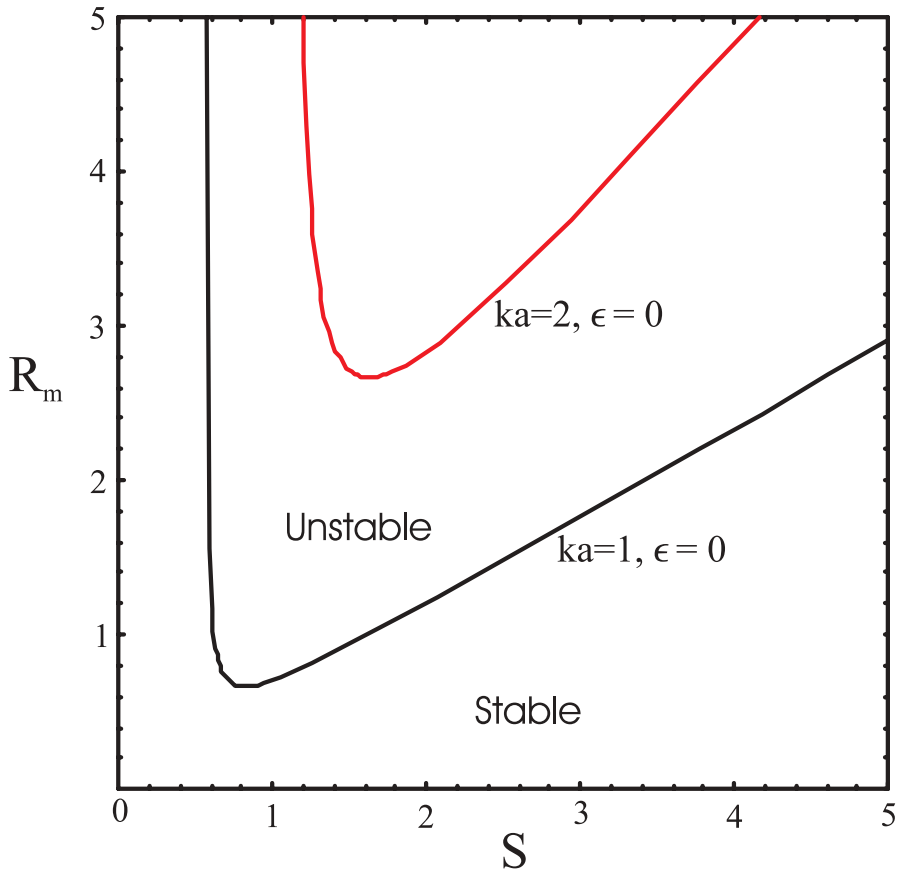

Figure 2.2: WKB stability diagram adapted from Ji et al. using $ka = 1$ (black) and $ka = 2$ (red). Both curves are for $\epsilon = 0$. We use our empirically-determined value of $\zeta = 0.5$. Our definitions of S and R_m are used (see Table 2.1).

are negative, and unstable otherwise.

Suppose we have a stable fixed point that turns unstable as β increases past β_c. If at β_c the eigenvalues are complex conjugates $\sigma = \varepsilon(\beta) \pm i\omega(\beta)$, then the instability is called a Hopf bifurcation. The time dynamics of a Hopf bifurcation are oscillatory. Below β_c, orbits spiral back toward the fixed point, and above the orbits spiral outward (see Fig. 2.3).

However, as the orbits get farther from X^*, the original linear approximation breaks down, and nonlinear terms need to be considered. Taking the next lowest term in the Taylor series expansion (making a series of suitable coordinate transformations [41]), the essential two dimensional dynamics can be cast in a generic normal form :

$$\begin{aligned} r' &= (\beta - \beta_c)\alpha r - ar^3 \\ \theta' &= \omega(\beta_c) + (\beta - \beta_c)\gamma + br^2, \end{aligned} \tag{2.37}$$

where r and θ are polar coordinates, a and b are constant coefficients, and $\alpha \equiv \frac{\partial \varepsilon}{\partial \beta}|_{\beta=\beta_c}$ and $\gamma \equiv \frac{\partial \omega}{\partial \beta}\,|_{\beta=\beta_c}$. Since the r' equation in Eqn. 2.37 separates from θ we see that there are periodic circular orbits with $r = const.$ (obtained from $r' = 0$). For $a \neq 0$ and $\gamma \neq 0$ these solutions occur at

$$r = \pm\sqrt{(-\gamma/a)(\beta - \beta_c)}.$$

The frequency θ' near the bifurcation in general depends linearly on the control parameter and linearly on the amplitude squared, but need not change at all (if γ and b are zero). Near the bifurcation, the growth rate depends linearly on the control parameter, $\varepsilon = \alpha(\beta - \beta_c)$.

Depending on the sign of a, the Hopf bifurcation is called either "supercritical" ($a > 0$) where the nonlinearity is saturating, or "subcritical" ($a < 0$) where the nonlinearity is further destabilizing. The normal form bifurcations for these two classes are diagrammed

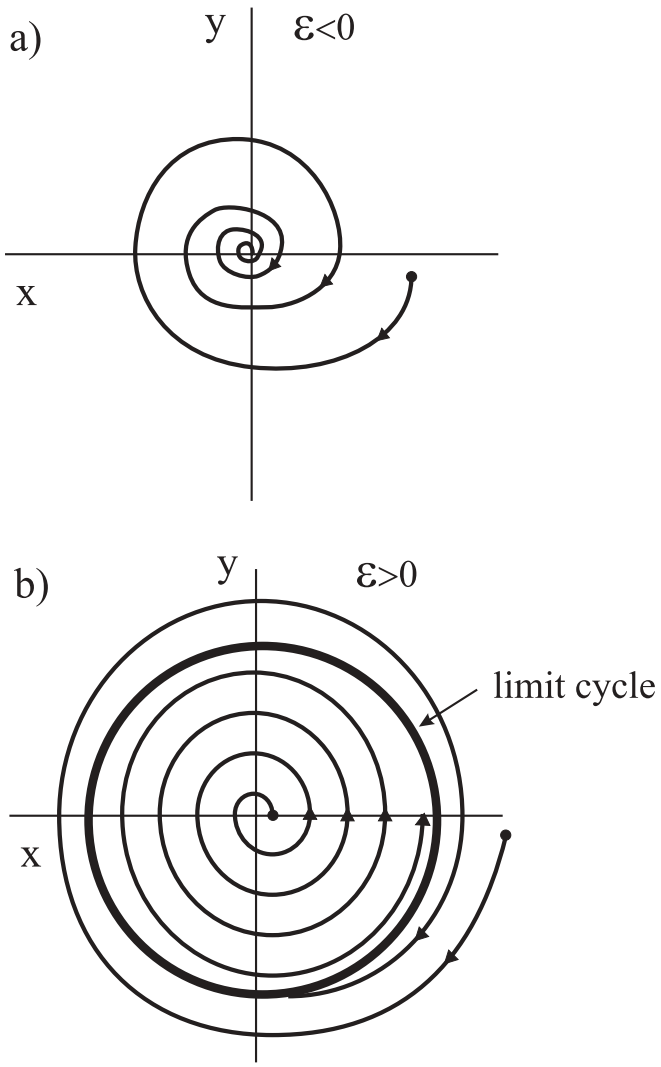

Figure 2.3: Illustration of a supercritical Hopf bifurcation below (a) and above (b) the critical value of the control parameter. The solid line in (b) represents the limit cycle occurring at a fixed value of r.

in Fig. 2.4. Subcritical bifurcations often lead to other bifurcations, as shown in Fig. 2.4b, leading to possible hysteresis.

For our system the control parameter is either the applied field or rotation rate, depending on the particular experiment (usually the former), and the relevant dynamical variables are the Gauss coefficients for the magnetic field. A Hopf bifurcation can occur in a system with any dimension greater than two, but the essential dynamics can be studied near (X^*, β_c) by restricting attention to an appropriate two-dimensional subspace of the phase space [81]. For the primary instability, for instance, we would choose as a subspace the Gauss coefficients g_1^{1c}, g_1^{1s}.

The bifurcation diagrams for real experiments often deviate from the normal forms (Fig. 2.4) because of "imperfections"—in our case, background turbulence or asymmetries in the system geometry. These deviations are accounted for by adding an imperfection parameter h to the normal form,

$$r' = (\beta - \beta_c)\alpha r - ar^3 + h$$

$$\theta' = \omega(\beta_c) + (\beta - \beta_c)\gamma + br^2,$$

which adds an asymmetry to the bifurcation diagram (Fig. 2.5), and breaks the bifurcation diagram into two pieces. We'll see in Chapter 4 that our data can be modelled reasonable well by a model of this sort.

2.6.5 Secondary instabilities

As seen in Fig. 2.2, the primary instability is suppressed for large field values. However, other modes can become unstable and might be expected to dominate at larger S. These transitions would likely be further Hopf bifurcations.

Figure 2.3 shows the possible velocity disturbances that can interact with the applied field to produce the observed dominant non-axisymmetric instabilities, as determined by

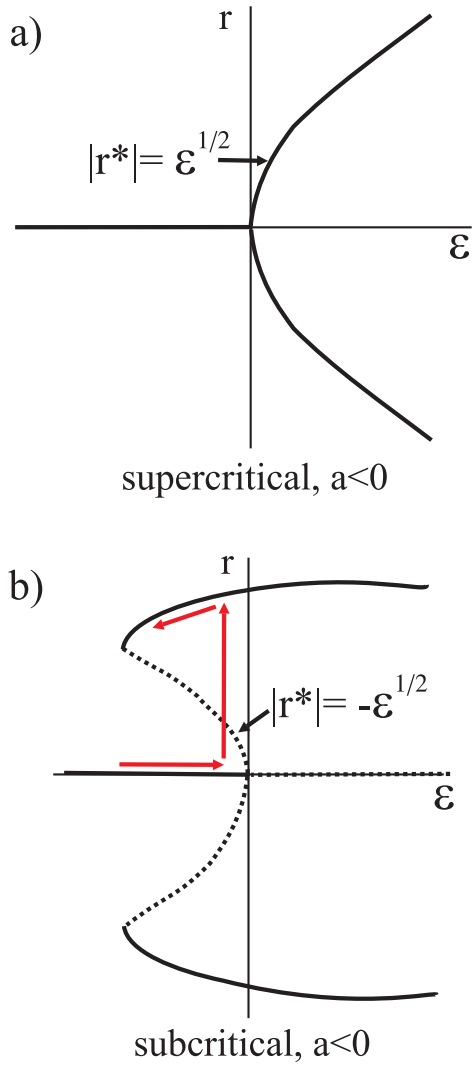

Figure 2.4: Normal forms of Hopf bifurcation diagrams for a) supercritical bifurcation and b) subcritical bifurcation. Solid (dashed) lines indicate stable (unstable) solutions. Each branch gives the amplitude r of the limit cycle; the solution also rotates in the θ direction (not shown). Stable branches from another bifurcation have been suggestively added in b), as unstable subcritical branches often lead to other stable bifurcation branches. The arrows show how hysteresis could arise.

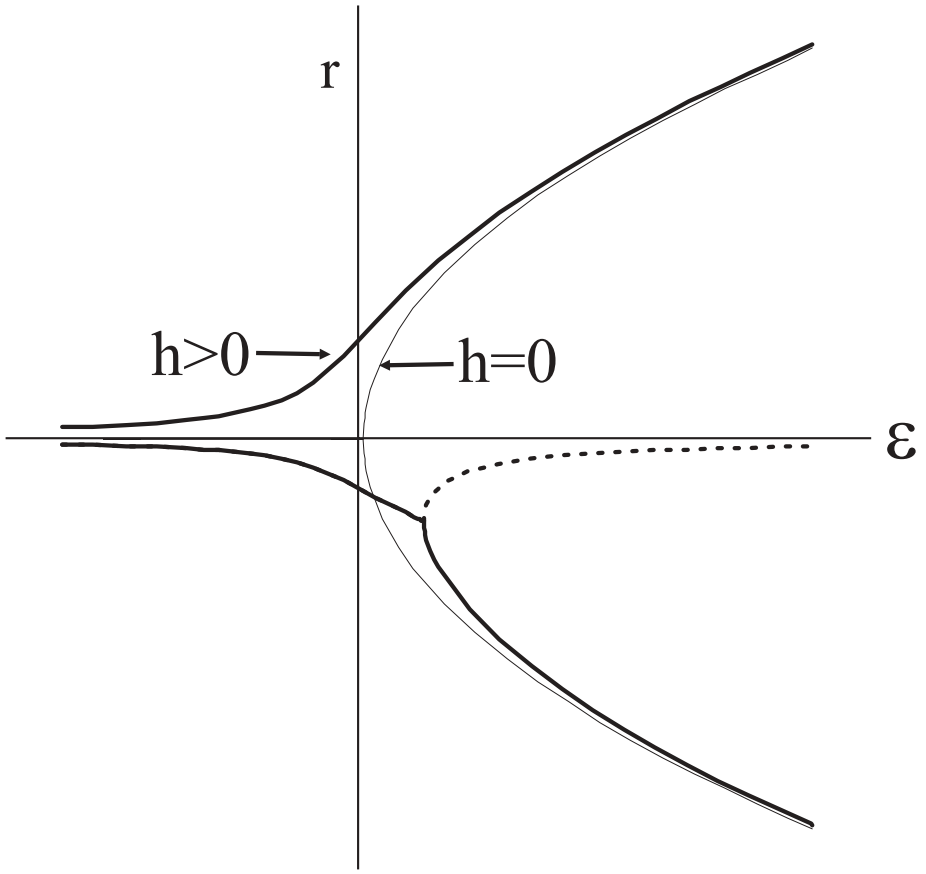

Figure 2.5: Imperfect form of a Hopf bifurcation. Shown for comparison is the perfect form, where $h = 0$.

the selection rules.

The applied field will tend to suppress velocity gradients in the $\hat{z}$ direction, and so we might expect the velocity field disturbance to change to one with a smaller z- gradient. Note that the $\vec{S}^1_{2b}$ mode, which occurs at a higher applied field than the primary instability, in fact results from a poloidal velocity mode ($\vec{S}^1_{1v}$) having a smaller z-gradient (compared to $\vec{S}^1_{2v}$ for the primary instability). For this instability, however, we can not rule out the toroidal velocity disturbance mode using the empirical arguments we used to rule out the toroidal disturbance mode for the primary instability.

2.7 Torque

In these experiments, there are two types of torque exerted on the inner sphere: Lorentz and viscous. Both tend to oppose the sphere's rotation. Together these torques times the rotation rate must cancel the total dissipation (Ohmic plus viscous) throughout the system. The Lorentz torque is not the torque caused by the applied field; the applied field affects both the Lorentz and viscous torques.

2.7.1 Lorentz torque

The Lorentz force exerts a Lorentz torque Γ_{Lor} on the inner sphere:

$$\vec{\Gamma}_{Lor} = \frac{1}{\mu_0} \iiint_{r=0}^{b} \vec{x} \times \left(\vec{J} \times \vec{B} \right) dV. \tag{2.38}$$

In our experiment, the only torque that does work is along $\hat{z}$ (since the shaft is constrained to rotate in that direction only), so we restrict ourselves to that component, and drop the vector arrow:

$$\Gamma_{Lor} = \frac{1}{\mu_0} \iiint_{r=0}^{b} r \sin\theta (J_\theta B_r - J_r B_\theta)\, dV, \tag{2.39}$$

where again the integral is throughout the inner sphere only.

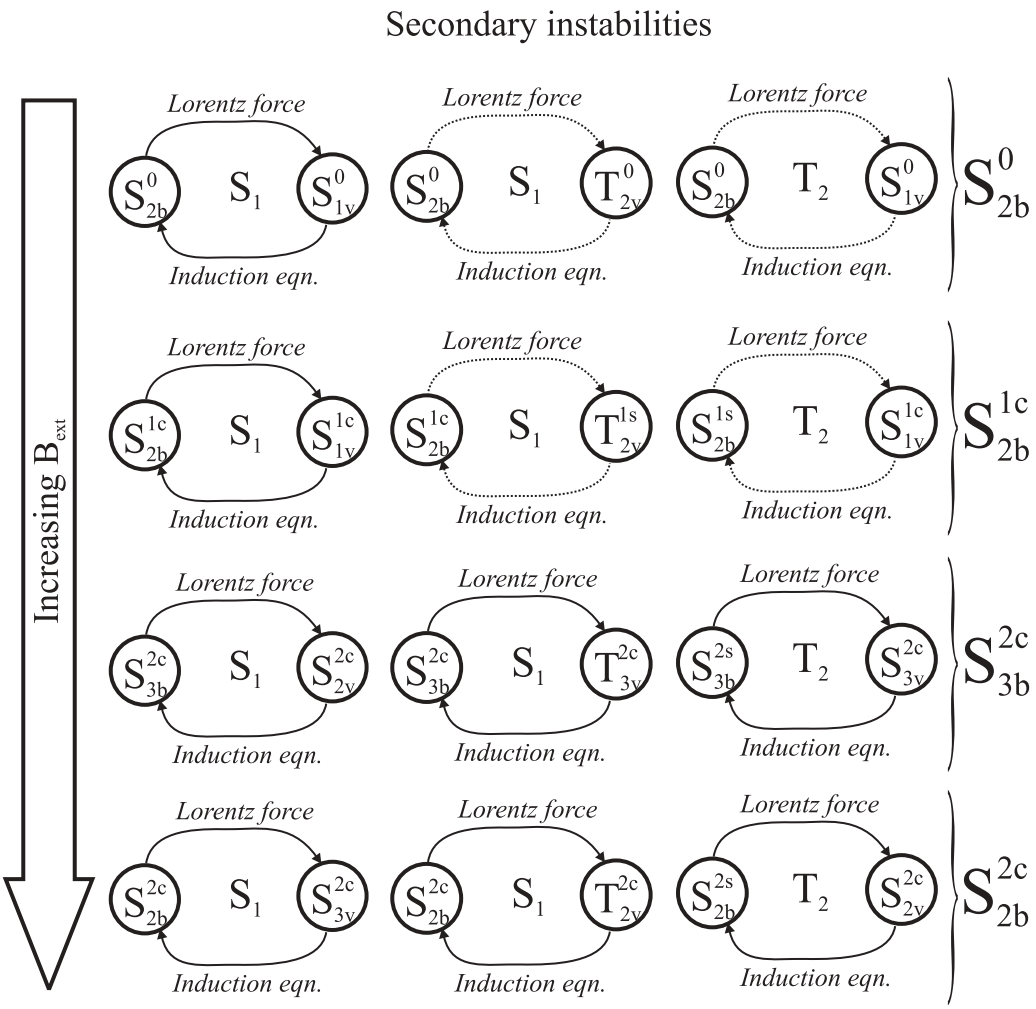

Figure 2.6: Diagram of all possible mode interactions involving $\vec{S}^0_{1B}$ or $\vec{T}^0_{2b}$ and the observed secondary magnetic field disturbances, in the order they are seen as the applied field is increased. Connections exist between two modes if they interact, through the Lorentz force or the induction equation, as determined by the selection rules.

By recognizing that the Lorentz force is the divergence of the Maxwell stress tensor and then applying the divergence theorem, this volume integral can be expressed as [87]:

$$\Gamma_{Lor} = \frac{b^3}{\mu_0} \iint_{r=b} B_r B_\phi \sin^2\theta \, d\theta d\phi, \tag{2.40}$$

Comparing to 2.13, we can see this expression is indeed the $r\phi$- component of the Maxwell stress tensor integrated over the surface of the sphere. We now have the Lorentz torque expressed in terms of the magnetic field only. In our experiment, we have limited knowledge about the azimuthal field at the inner sphere boundary; from measurements of the torque and poloidal field, this expression might allow us to estimate B_ϕ.

Note that the Lorentz torque does not occur for an insulating inner sphere, since currents do not flow through it, making Eqn. 2.39 zero (or equivalently, since the azimuthal field at the inner sphere boundary is zero, making Eqn. 2.40 zero).

The solid analogue of spherical Couette

Bullard [6] studied the solid analogue of our experiment—replacing the liquid sodium by a solid spherical shell. We review his result briefly here because it serves to isolate the Lorentz torque from more complicated fluid effects. As in our experiments, his system also has a solid conducting spherical rotor and a constant applied field parallel to its axis of rotation. In his calculation, the spherical shell has the same conductivity as the outer shell. The torque, which can be solved for analytically, is:

$$\begin{aligned} \Gamma &= \frac{8\pi}{75} B_{ext}^2 b^5 \sigma \Omega (1 - b^5/a^5) = \frac{4}{15\mu_0} B_{ext} B_\phi(max.) b^3 \\ &\sim \Omega B_{ext}^2 \end{aligned} \tag{2.41}$$

where B_ϕ(max.) is the maximum value of the azimuthal field in the system, which in this case occurs at $r = b$ and $\theta = \pi/4, 3\pi/4$. The azimuthal field B_ϕ is generated from B_{ext}

by differential rotation, dv_ϕ/dr. Here differential rotation is entirely localized at the inner sphere boundary, concentrating B_ϕ for maximum torque (see Eqn. 2.28).

When the outer shell is a conducting fluid, as in our experiment, the differential rotation gradients are smaller, as the azimuthal velocity becomes zero only at the outer sphere boundary. Thus B_ϕ(max) in our experiment is smaller, and correspondingly, the Lorentz torque should be smaller than above. The first equality in Eqn. 2.41 should give upper limit on the Lorentz torque in our experiment. Note that in this problem, the torque needed to spin the sphere times the rotation rate must cancel the Ohmic dissipation. There is no viscous dissipation nor viscous torque.

Fluid effects

Two major differences between our fluid experiment and the solid analogue are that the fluid can generate currents (which the solid outer shell obviously cannot) and that the Lorentz force can modify the fluid flow. Both can impact viscous and Ohmic dissipation, and thus the torque. Note that the Lorentz torque expression (Eqn. 2.39) only includes currents that enter the inner sphere; however, the fluid can create currents that need not enter the inner sphere—in fact *will not* in the case when the inner sphere is an insulator.

The Ohmic dissipation is due to induced currents throughout the system. Some fraction of the total torque, what we'll call Γ_J, supplies the energy of this loss:

$$P_{Ohm} = \Gamma_{Ohm}\Omega = \frac{1}{\sigma\rho}\iiint J^2\, dV.$$

Γ_{Ohm} is not necessarily Γ_{Lor}, nor is it the Lorentz torque integrated throughout the entire system. The latter, in fact, is zero in the small-R_m limit. Consider Eqn. 2.38 after using identity A.9:

$$\Gamma_{Lor,sys} = \iiint_{r=0}^{a} \hat{z}\cdot\left[\left(\vec{x}\cdot\vec{B}\right)\vec{J} - \left(\vec{x}\cdot\vec{J}\right)\vec{B}\right] dV.$$

Invoking the small-R_m approximation, the first term is zero, since Ohm's law becomes $\vec{J} = \vec{u} \times \vec{B}_{ext}$, which implies $\vec{J} \cdot \vec{B}_{ext} = 0 = \hat{z} \cdot \vec{J}$, leaving, after using identity A.5 and that $\vec{J}$ is divergenceless:

$$\Gamma_{Lor} = \frac{-B}{2} \iiint_{r=0}^{a} \vec{\nabla} \cdot (x_\perp^2 \vec{J}) dV.$$

From the divergence theorem, this integral is zero, because at the outer sphere $\vec{J} \cdot d\vec{\sigma}$ is zero. Thus for Γ_J to not exactly cancel Γ_{Lor} there must be nonzero Lorentz torques in the directions perpendicular to $\hat{z}$ that couple viscously to the inner sphere to produce a torque in the direction of rotation.

The Ohmic dissipation in the solid analogue increased as B_{ext}^2. With a fluid outer shell it changes in a more complicated way as the Lorentz force modifies the fluid flow. We saw in Sect. 2.3.1 that the Lorentz force suppresses gradients in the direction of the field and leaves the other directions unaffected, thus increasing the ratio of length scales parallel and perpendicular to the applied field $l_\parallel / l_\perp$. This ratio affects the Ohmic dissipation, as we'll now show.

First take the curl of Ohm's law:

$$\vec{\nabla} \times \vec{J} = \sigma \left(\frac{\partial \vec{B}}{\partial t} + (\vec{B}_{ext} \cdot \vec{\nabla}) \vec{u} \right), \tag{2.42}$$

where Faraday's law has been substituted for the first term and identity A.4 has been used on the second. Proceeding as before, we neglect the Faraday term because the induced field is much smaller than the applied field and the characteristic induced field frequency is much smaller than the advective frequency, $b_{ind}\Omega_b \ll B_{ext}\Omega$. By dimensional analysis, Eqn. 2.42 leads to:

$$J \sim \sigma B_{ext} \left(\frac{l_\perp}{l_\parallel} \right) U.$$

Substituting into the expression for Ohmic dissipation then gives

$$P_{Ohm} = \Gamma_{Ohm}\Omega \sim \sigma B^2 \left(\frac{l_\perp}{l_\parallel}\right)^2 U^2. \tag{2.43}$$

Thus the torque needed to cancel Ohmic dissipation has the same scaling with applied field and rotation rate as the solid analogue except that it is modified by the ratio of length scales in the flow.

Davidson [26] and Moreau [74], from considering decaying turbulence, argue that the flow will evolve diffusively in time toward

$$N \left(\frac{l_\perp}{l_\parallel}\right)^2 \sim 1, \tag{2.44}$$

on the time scale $\tau = (\sigma B^2/\rho)^{-1}$, called the magnetic damping time. That is, the applied field causes the length scale ratio $l_\parallel/l_\perp$ to grow to $N^{1/2}$ as $(t/\tau)^{1/2}$. However, if τ is large compared to Ω, i.e., if $N \ll 1$, then $l_\parallel/l_\perp$ will remain of order unity (assuming an isotropic initial condition).

Thus, for a fixed rotation rate, we might anticipate two regimes of electromagnetic coupling. For small N, the torque will scale as $\Gamma \sim B_{ext}^2$, and for large N become independent of applied field. The transition should occur somewhere near $N = 1$ and will happen over some finite range of N.

However, though we see changes in the torque curves near $N = 1$, we don't see the torque becoming independent of applied field. There are at least two possibilities why. First, the instability could change the development of length scale separation from the decaying turbulence prediction (Eqn. 2.44). Second, the dissipation in the boundary layers could become significant at large field. The Ohmic dissipation in the boundary layer near the poles is given by Eqn. 2.43, where $l_\parallel$ now is the thickness of the boundary layer and $l_\perp$ is approximately b. The effect of this dissipation on the torque will be weighted by

the volume fraction of the boundary layer to the bulk—approximately $l_\parallel/l_\perp$. Thus, the torque due to Ohmic dissipation in the boundary layer scales as

$$\Gamma_{Ohm,BL} \sim \sigma B^2 \left(\frac{l_\perp}{l_\parallel}\right) U.$$

As we'll see shortly, the boundary layer perpendicular to the applied field thins because of the Lorentz force. Also, the viscous dissipation could be affected by the Lorentz force. We look at viscous effects next.

2.7.2 Viscous torque

The viscous torque is due to the wall shear stress $\vec{\tau}_w$ at the inner sphere boundary:

$$\Gamma_{mech} = \hat{z} \cdot \iint_{r=b} \vec{x} \times \vec{\tau}\, d\sigma.$$

In general, the wall shear stress is $\vec{\tau}_w \equiv \rho\nu|\frac{\partial}{\partial r}\frac{u_\phi}{r}|_{r=a}\,\hat{\phi}$. In our experiments, where at the smallest rotation rates $Re \sim 10^5$, the wall shear stress should be described by a standard turbulent mechanical drag law:

$$\vec{\tau} = \rho C_D |\vec{u}|\vec{u},$$

where $\vec{u}$ is the fluid velocity outside the boundary layer, and C_D is the empirically-derived dimensionless drag coefficient. This law gives for the viscous torque

$$\begin{aligned} \Gamma_{mech} &= \iint_{r=b} r\sin\theta(\rho C_D r^2 \sin^2\theta\,\Omega^2)\, d\sigma \\ &= \frac{3\pi^2}{4}\rho C_D \Omega^2 b^5. \end{aligned} \tag{2.45}$$

That is, assuming fully developed turbulence and no external fields the torque should increase quadratically with the rotation rate.

However, C_D is not necessarily constant in practice, even at $Re \sim 10^6$ [65]. A model, developed by Grossmann and Lohse, accounts for this discrepancy from a Kolmogorov turbulent prediction by splitting the torque into a bulk contribution, where Kolmogorov

theory holds, and a laminar boundary layer contribution where the drag coefficient depends weakly on Reynolds number, $C_D \sim Re^{-1/2}$. That is:

$$G = c_1 Re^{3/2} + c_2 Re^2, \tag{2.46}$$

where $G = \Gamma/2\rho\nu^2 L$ is the dimensionless torque, and c_1 and c_2 are constants to be determined by experiments. However, the confounding errors from the seals and packing ultimately prevent us from applying this model usefully, and we revert to assuming a $G \sim \Gamma \sim \Omega^2$ dependence.

Applied fields can affect viscous coupling

The mechanical torque expression (Eqn. 2.45) does not include effects of the applied field, however, which will modify the boundary layers and thus the mechanical coupling. (Boundary layers modified by applied fields perpendicular to the boundary are called Hartmann layers, after Hartmann who first observed this effect in duct flow.) The thickness of a Hartmann layer δ_{Ha} is the length scale where viscous forces cancel the Lorentz force,

$$\delta_{Ha} = (\rho\nu/\sigma B_\perp^2)^{1/2} = (Re\, N)^{-1/2} L, \tag{2.47}$$

where $B_\perp$ is the magnetic field component perpendicular to the boundary.

The effects of applied fields on the boundary layers will only be noticeable if the Hartmann layers are comparable or smaller in length than the viscous and Ekman boundary layers. For the first, the balance of the advective term and the viscous force, $\left(\vec{\nabla}\cdot\vec{u}\right)\vec{u} \sim \nu\nabla^2\vec{u}$, gives:

$$\delta \sim (\nu L/u)^{1/2} \sim Re^{-1/2} L. \tag{2.48}$$

For the second, the balance of Coriolis and viscous forces, $2\vec{\Omega}\times\vec{u} \sim \nu\nabla^2\vec{u}$, gives:

$$\delta_{Ek} \sim (\nu/2\Omega)^{1/2} \sim 0.2 Re^{-1/2} L. \tag{2.49}$$

Though our outer vessel is non-rotating, Coriolis forces are nonetheless relevant. For instance in the reference frames of the fluid near both poles of the inner sphere—which are tied to the sphere because of the no-slip boundary conditions—a Coriolis force is felt that drives flow away from the equator. This effect is known as Ekman pumping; in our system it drives a weak secondary $\vec{S}^0_{2v}$ flow.

From the above estimates, in particular Eqns. 2.49 and 2.47, we might estimate for our system that Hartmann layer effects will only become important when $N \gtrsim 25$. However, in turbulent flows (e.g., the ocean) the Ekman layer is often found from measurements to be thicker than expected (from an analysis like the above) [82]. There is no known general theory that predicts the thickness of these Ekman layers from system to system, so here we can only mention that Hartmann layers may become important before $N \approx 25$. When they do become important, we might expect the torque to increase with an increasing applied field according to a Grossmann-Lohse type model [102], where viscous as well as Ohmic dissipation in both the boundary layers and bulk is considered.

2.7.3 Putting it all together

The total torque exerted on the inner sphere will be a combination of viscous and Lorentz torques, and their sum times the rotation rate will cancel the total (viscous and Ohmic) dissipation:

$$\Gamma_{total} \sim \frac{U^2}{l_\perp} + \frac{\sigma}{\rho}\left(\frac{l_\perp}{l_\parallel}\right)^2 UB^2, \tag{2.50}$$

where the terms on the right represent the torque from the viscous and Ohmic dissipation respectively. Above, the dissipation in the boundary layers, which depend differently from dissipation in the bulk, has been assumed to be negligible.

In experiments where B is ramped up while Ω is fixed, the above relation together

with an assumption for the length scale separation (Eqn. 2.44) predicts the torque will: (*i*) be roughly constant while $N \ll 1$, (*ii*) increase quadratically in B while N is less than 1 but moderate, and (*iii*) then become independent of B for $N \gg 1$, transitioning between (*ii*) and (*iii*) in an unknown way at $N \sim 1$. Prediction *iii* is never observed, however. At large field, either the length scale separation assumption (which did consider instabilities) does not hold or dissipation in the boundaries becomes important. Lastly, a sudden change in the length scale ratio—which might happen when an instability suddenly turns on or off—might incur sudden changes in torque. Such length scale changes are reflected in the data.

Chapter 3

Measurement techniques and experimental detail

3.1 Magnetic field measurements

3.1.1 The Hall array

We developed an array of Hall probes (the "Hall array") to measure and decompose the induced field into spherical harmonics—the $\vec{S}$'s from Chapter 2. (The $\vec{T}$'s are confined inside the sphere and can't be measured from outside.) The design, construction, and analysis of measurements taken from this array form the heart of this dissertation.

A single Hall probe measures the magnetic field at one position and in one direction. As its name suggests, this probe uses the Hall effect[1]: charge carriers moving through a piece of semiconductor are deflected by a magnetic field perpendicular to their velocity, producing a voltage difference (the Hall voltage) proportional to the current and magnetic field. The Hall voltage is typically very small, so each probe needs an amplifier. The Hall voltage is also proportional to the number of charge carriers, which in turn depends strongly on temperature. Thus, probes either need to be kept at a constant temperature, or be compensated for temperature. Also, each probe needs a constant current source.

[1]The Hall effect—and by association the Hall probe, Hall voltage, and (now) Hall array—is named after E.H. Hall, who discovered it in 1879. Despite the special name, it's a straightforward effect of the Lorentz force.

The probes we chose to use in the array—Honeywell SS94A1F (see Fig. 3.1)—have these electronics built-in. Though not having optimal noise characteristics, being self-contained they are the most convenient. We were also already familiar with these probes, having used them in several other experiments, and they are relatively inexpensive.

The measurement range of the probes is ± 100 G, meaning the probes have to be aligned perpendicular to the applied field—that is, in the cylindrical r or cylindrical θ directions. Axisymmetric poloidal modes (which we want to measure) have no component in the latter, however, so we aligned the probes radially. In this alignment the probes measure components of both spherical r and spherical θ. The induced field is never larger than 20 G, so the only problem with saturation would be due to misalignment (from either the probes or the field coils). There are probes with higher ranges available (even in the same Honeywell line), but by using those, the freedom of choosing alignment would be offset by a higher noise floor and a lower resolution.

The more probes we have in the array, the better we can describe the field. The maximum number of probes in the array design was limited by our analog-to-digital acquisition card, which has 32 inputs. One input is used to measure the applied field and another to measure the torque, leaving 30 channels to be used in the array.

Decomposing the field consists of finding the Gauss coefficients[2] for the modes. The number of coefficients scales with the maximum order l of the spherical harmonics according to:

$$\#\text{ of coefficients} = l(l+2) \tag{3.1}$$

To have sufficient information, we need to have at least as many measurements as coef-

[2]After the mathematician Carl Friedrich Gauss, who first developed the least squares technique. He used it to fit the Earth's field to spherical harmonics. He was also the first to measure magnetic field in absolute units: what we now call the Gauss (1 Gauss = 10^{-4} T).

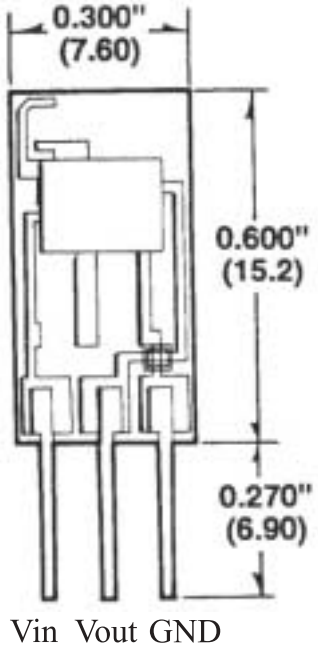

Figure 3.1: Schematic of a Honeywell SS94A1F Hall probe used in the Hall array. The chip includes an amplifier, a constant current source, and a temperature compensation circuit. Its measurement range is ± 100 G.

ficients. It is better to have all the modes of a given order—and also better to have an overdetermined problem—so our 30 probes constrains us to $l_{max} = 4$, having 24 coefficients.

3.1.2 Decomposing the measured field: Least squares

We need to find the 24 Gauss coefficients that best fit the 30 magnetic field measurements.

The least squares technique finds this best fit by minimizing the squared difference, or error, of the measured field $B_{meas}(x_p)$ and the decomposed model field $B_{model}(x_p) = \sum_c g_c f_c(x_p)$ at probe position $x_p = (r, \theta, \phi)$, summed over all probes:

$$\begin{aligned} \sum_{probes} B_{err}^2 &= \sum_{probes} \left[B_{meas}(x_p) - B_{model}(x_p)\right]^2 \\ &= \sum_{probes} \left[B_{meas}(x_p)^2 - 2B_{model}(x_p)B_{meas}(x_p) + B_{model}(x_p)^2\right] : \end{aligned} \tag{3.2}$$

The f_c's are the basis functions to which we are trying to fit—in our case the poloidal spherical harmonic modes (see Sect. 2.5). In our experiments, the probes are aligned in the cylindrical r direction, so we take as our basis the cylindrical r component of the $\vec{S}'s$:

$$f_n(r, \theta, \phi) = (\sin\theta\hat{r} + \cos\theta\hat{\theta}) \cdot \vec{S}_l^m \tag{3.3}$$

where the radial functions are $S(r) = Ar^{-n}$. The constant A is chosen to yield the Schmidt normalization—the standard for publishing Gauss coefficient values for the Earth. The explicit forms for the f's are given in the appendix. The f's have only one index whereas the $\vec{S}_l^m$s have two (l and m) plus c and s; we chose f1, f2, f3, f4, etc. to correspond to $\vec{S}_1^0, \vec{S}_1^{1c}, \vec{S}_1^{1s}, \vec{S}_2^0, etc.$ Note that, though we are fitting to spherical harmonics in only the cylindrical r direction, the best-fit coefficients give us the best-fit field in all three directions.

The summed squared error, being positive definite and quadratic in each coefficient,

will have a zero second derivative at only one point, its minimum. Thus, the best least square fit satisfies

$$\frac{\partial\left(\sum_{probes} B_{err}^2\right)}{\partial g_c} = 0 = \left[\sum_{probes} \left(-2B_{meas}(x_p)f_c(x_p) + 2B_{model}f_c(x_p)\right)\right],$$

for all coefficients g_c.

Substituting for B_{model} with Eqn. 3.1 we obtain, in matrix form, the following system of equations:

$$\vec{Bf} = \mathbf{M}\vec{g} \tag{3.4}$$

where

$$\vec{Bf} = \begin{pmatrix} \sum_{probes} B_{meas}(x_p)f_1(x_p) \\ \sum_{probes} B_{meas}(x_p)f_2(x_p) \\ \vdots \\ \sum_{probes} B_{meas}(x_p)f_{24}(x_p) \end{pmatrix}, \quad \vec{g} = \begin{pmatrix} g_1 \\ g_2 \\ \vdots \\ g_{24} \end{pmatrix}, \tag{3.5}$$

and

$$\mathbf{M} = \begin{pmatrix} \sum_{probes} f_1(x_p)f_1(x_p) & \sum_{probes} f_1(x_p)f_2(x_p) & \dots & \sum_{probes} f_1(x_p)f_{24}(x_p) \\ \sum_{probes} f_2(x_p)f_1(x_p) & \sum_{probes} f_2(x_p)f_2(x_p) & \dots & \sum_{probes} f_2(x_p)f_{24}(x_p) \\ \vdots & \vdots & \ddots & \\ \sum_{probes} f_{24}(x_p)f_1(x_p) & \sum_{probes} f_{24}(x_p)f_2(x_p) & \dots & \sum_{probes} f_{24}(x_p)f_{24}(x_p) \end{pmatrix} \tag{3.6}$$

However, to find the coefficients we need to invert this equation:

$$\vec{g} = \mathbf{M}^{-1}\vec{Bf}. \tag{3.7}$$

This inversion is possible of course only if M is invertible. Moreover, to make the inversion sufficiently insensitive to error the ratio of its smallest to largest eigenvalues needs to be

sufficiently close to one. This ratio is called the condition number, and it quantifies how sensitive the inversion is to errors in measurement and probe location. The matrix $\mathbf{M}$ depends only on the spatial locations of the probes x_p.

In the final implementation, the above procedure was programmed in C. The inverse matrix $\mathbf{M}^{-1}$ was found using MATHEMATICA and was read from a file.

3.1.3 Array configuration design

The problem was to find a configuration of 30 probe positions that gives an acceptable condition number. Qualitatively, we might expect the configuration to be evenly spaced around the sphere—or at the least not highly-clumped together. It is analogous to fitting a line over a range of an independent variable: an even distribution of measurements over the extrapolating range produces a better fit than clumped measurements. The difference here is that the independent variable is not a single parameter space, but the space spanned by the spherical harmonics.

The first design constraint, as mentioned above, was that the probes be aligned in the cylindrical radial direction. Another constraint was that the configuration be easily assembled and disassembled, since the sphere is periodically disassembled. The procedure therefore has to be repeatable: the probe positions have to be the same from run to run. We also want the probes as close to the sphere as possible to increase the signal-to-noise ratio. However, the sphere reaches 120° C—and the heaters even higher temperatures—while the probes are only rated for 100° C, meaning we should keep the array some distance from the sphere. Also, two extra shaft ports (shown in Fig. 3.2, but used only in experiments not reported here), along with (somewhat haphazardly) protruding electric cartridge heaters and copper hexane-filled cooling lines limit where the rings can go, and

where they can get to. The final and most obvious constraint is that the arrangement be (hopefully easily) buildable.

The first design stage was to determine condition numbers, using MATHEMATICA, for a variety of probe configurations. A number of basic design shapes were considered, including pole-to-equator arcs, equatorial half-arcs, rings, and, for comparison, randomly distributed probes. The number of rings, arcs, etc. were varied, along with their size, distance from the sphere, and number and spacing of probes on each. Most configurations, including many of the random distributions, produced poor condition numbers ($< O(10^{-5})$)—some very poor condition numbers ($< O(10^{-12})$).

After much trial-and-error exploring, four latitudinal rings—two near the equator on opposite sides, and one near each pole, with probes spaced evenly on each ring—was determined to be the most promising configuration. That this design shape works well is perhaps not surprising, as qualitatively it does cover the outer sphere evenly. Furthermore, rings could be easily machined to high precision using a mill and a rotating table, and precisely positioned outside the sphere. Even with this basic design shape, however, the condition number ranged widely. The condition number was improved by having slightly more probes on the rings near the equator, and for the probes on these equatorial rings to be offset by an azimuthal angle with respect to each other, to increase the azimuthal coverage there[3]. Further trial-and-error exploration of ring diameters and distances from the equator, subject to the constraints above, determined the final design (see Fig. 3.2). The final condition number was 0.05. The probe positions are listed in Appendix B.2.

The chosen material for the rings is a high-temperature phenolic—cotton fiber embedded in epoxy. Besides being temperature-resistant, it is also electrically insulating, so

[3]The condition number was insensitive to the azimuthal offset of the rings near the poles relative to the other rings.

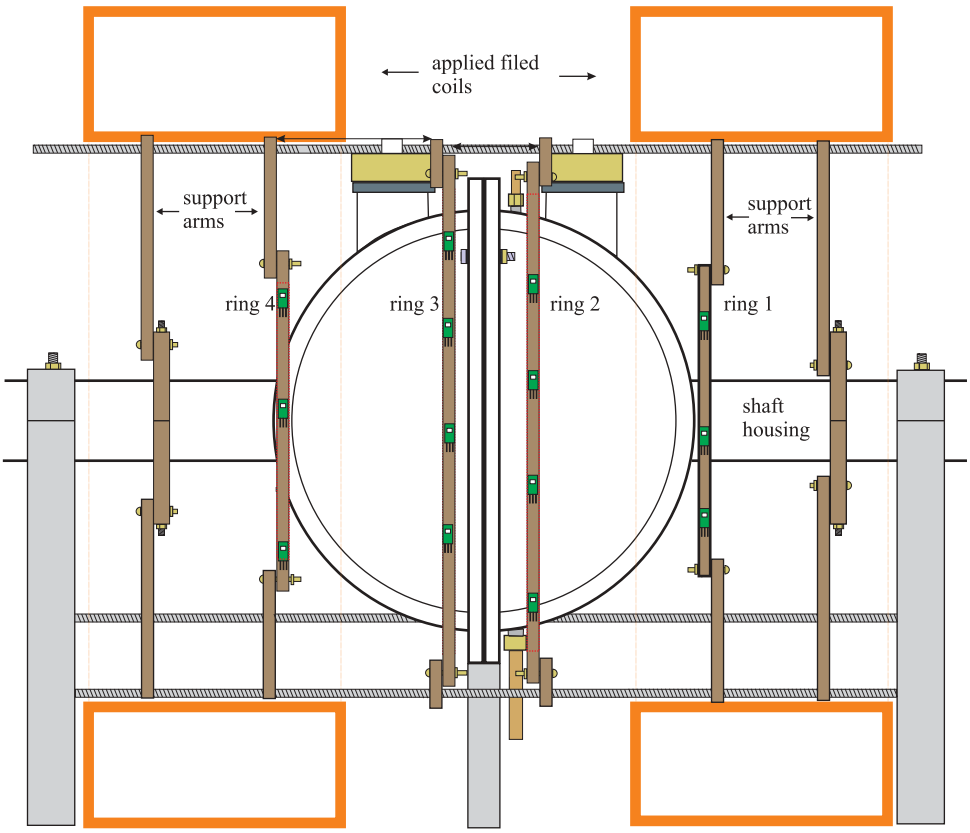

Figure 3.2: The Hall array shown as it is positioned in the experimental apparatus. The rings attach to three non-magnetic stainless steel threaded rods by support arms that bolt to each ring. The rods are held in place by two three-armed supports that clamp to the shaft housing. The rings are $3/8''$ thick, and have an inner-outer radius difference of $1/2''$.

the probes are not magnetically shielded. It is also durable and (relatively) easily machinable. The probes were fixed to the rings with superglue. This glue, however, is brittle and becomes unstable at high temperatures, and a few probes came off in the course of the runs. These probes were reattached using RTV.

We machined the rings using a mill and a rotating table, allowing the ring diameters and centers to be within ± 0.001 in (± 0.0254 mm) the design specification. The azimuthal angles of each probe could be placed to within about 0.5°. We also machined two three-armed holders, which clamped to the shaft housing and held three $1/2''$ stainless steel threaded rods at a radius slightly bigger than the biggest ring's radius. Each ring had three removable arms that attached each ring to the three rods. The rings are fixed in place along the rods with nuts.

An error estimate

The condition number gives a measure of how good a configuration is, but is only so useful. The condition number of the final configuration, for example, is 0.05, which seems possibly acceptable, but is it good enough? There are two sources of error that can be amplified by an imperfect probe distribution: errors in probe positions, and noise. We get an estimate of the errors in the system with the following technique. Take a coefficient vector $\vec{g}_n$ with 1 as the n-th component and the rest zeroes (e.g., $\vec{g}_3 = (0, 0, 1, 0...0)^T$) and multiply by $\mathbf{M}_{true}$, constructed with the actual probe positions, to produce $\vec{Bf}_n$:

$$\vec{Bf}_n = \mathbf{M}_{true}\vec{g}_n.$$

The true probe positions will differ from the expected positions (where we think the probes are). Next add random noise to $\vec{Bf}_n$ to simulate electronic and magnetic noise from the probes. Finally, obtain the simulated measured coefficients with the inverse matrix using

the *expected* probe positions, $\mathbf{M}_{exp}^{-1}$, by multiplying it and ($\vec{Bf}_n$+ noise). Note that further problems could occur if the perturbed (actual) matrix has a worse condition number than $\mathbf{M}_{exp}$.

Figure 3.3 shows the result of this technique using the chosen probe locations. We estimated that the error in the probe positions would be primarily due to errors in separation distance from the equator z_{err}, since the rings must be repositioned in z every time the system is disassembled. Spacer bars that also located the center were machined to make this process consistent. There would also be some error because the rings are out of center x_{err} and y_{err}, either from slight bowing in the rods or misplacement of the holes locating the holders. We took $|z_{err}| = 1$ mm, and $|x_{err}| = |y_{err}| = 0.5$ mm. For the noise, we estimated $B_{noise} = 0.05$ G, from a time series without rotation or applied field. Different trials, where the sign of the error for each ring was randomly chosen to be in the positive or negative directions, produced qualitatively similar results. Doubling the error roughly doubled both the number of noticeable spurious coefficients and their magnitude of error.

3.1.4 Reconstructing the induced field

Once the coefficients were found, a best-fit induced field could be reconstructed for all points outside the sphere. Shown in Fig. 3.5 is the cylindrical radial component of several modes on the surface of a sphere, using an equal area projection (see Fig. 3.4). By summing weighted averages of frames like these for each sample time, movies of the radial induced field can be made. Several snapshots of such movies appear in Chapter 4.

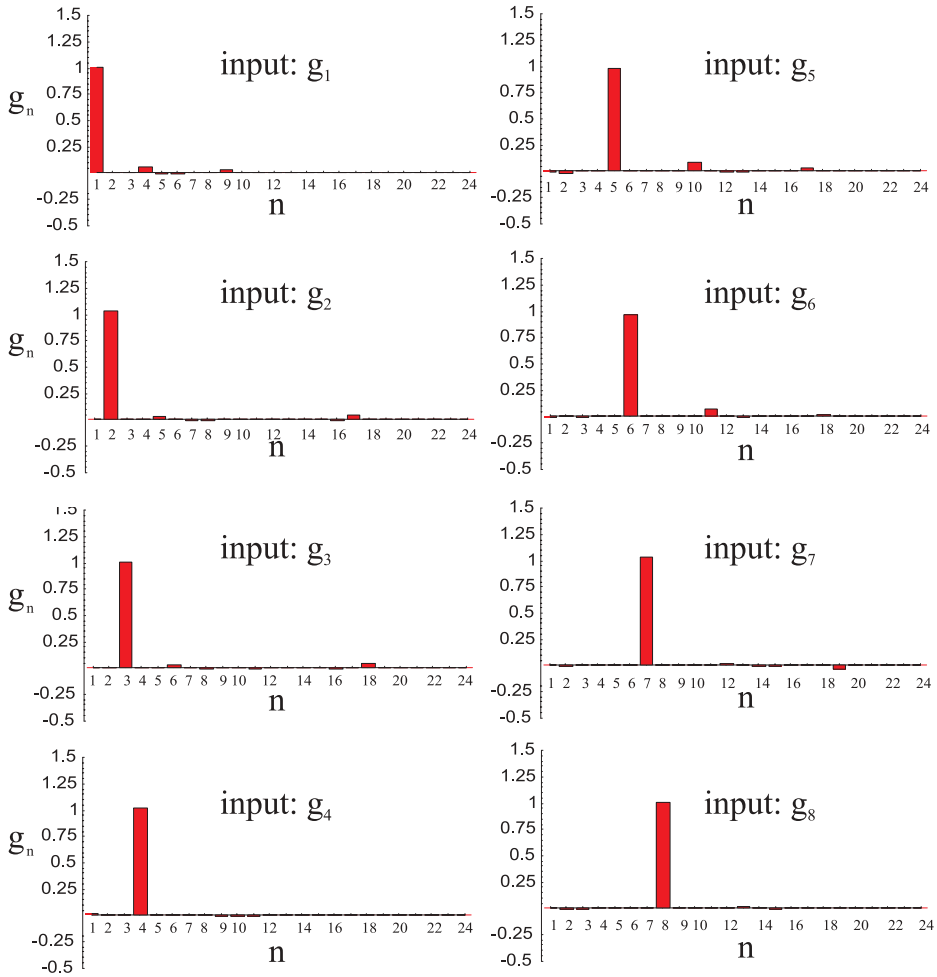

Figure 3.3: Simulated effect of Hall probe noise and probe positioning error. A pure input—the projection of one mode (having unity amplitude) onto the Hall probes—was subjected to noise and then inverted back to coefficient space using an inverse of a matrix constructed from "expected," but erroneous, probe positions. This output is shown for the first eight coefficients; the remaining 16 are qualitatively similar. No spurious coefficients were greater than 0.25. Here, $z_{err} = +1$ mm, and $x_{err} = y_{err} = +0.5$ mm.

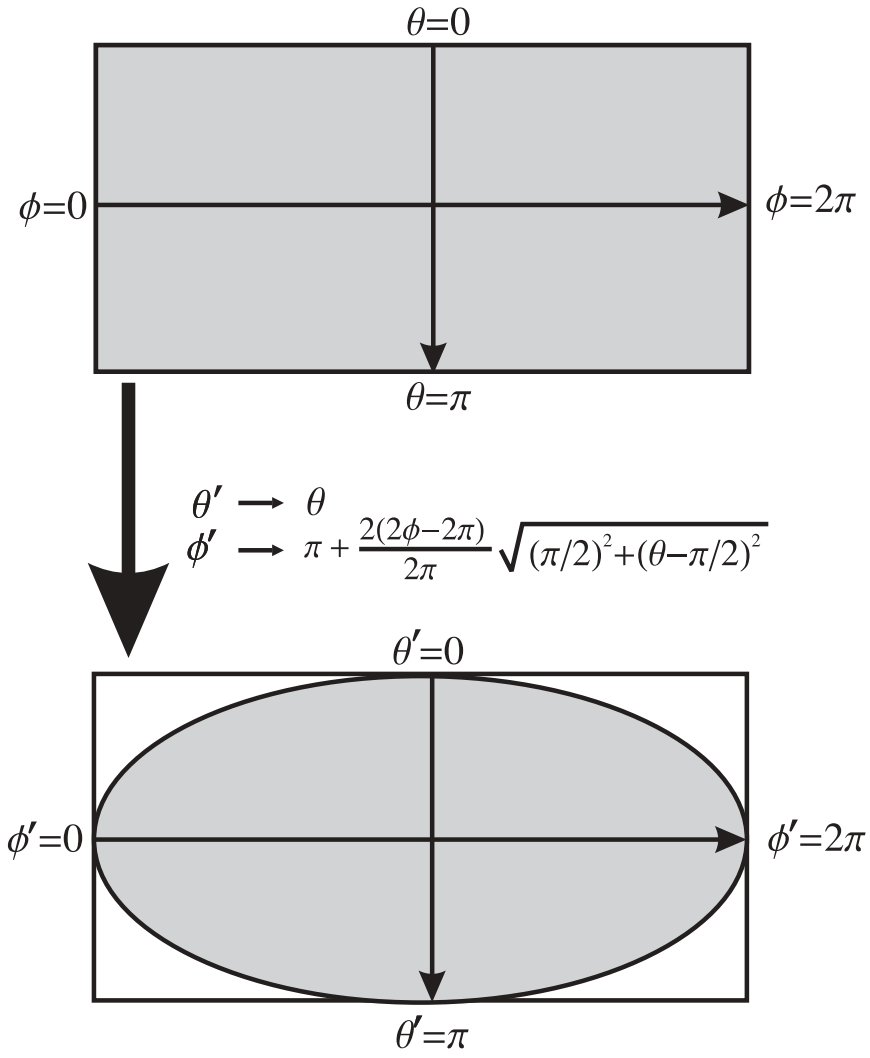

Figure 3.4: Equal area projection used to display radial component of induced field at the surface of a sphere. The angles $\theta, \phi, \theta', \phi'$ are all in spherical polar coordinates. To perform the projection start with the projection on top—ϕ, θ plotted as though Cartesian coordinates. Then transform to ϕ', θ', as shown, plotting ϕ', θ' (again) as Cartesian coordinates.

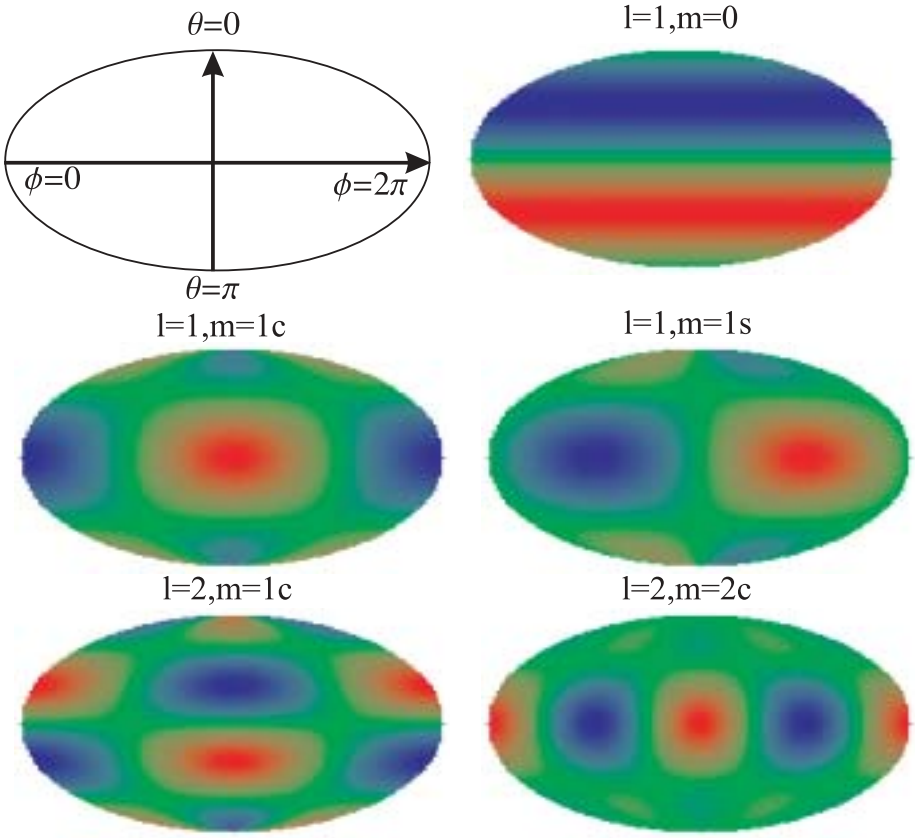

Figure 3.5: Cylindrical radial component of several coefficients on the surface of a sphere, in a equal area projection. Color represents intensity: red (positive), blue (negative), green (null).

3.1.5 Toroidal fields

Induced fields, which necessarily originate inside the sphere, must have a nonzero radial component to be seen outside the sphere. Therefore the array will only measure poloidal field components and to observe toroidal fields we need to place a probe inside the sodium. For a couple runs, we placed a hollow 1/2" stainless steel sheath inside the sodium with a Hall probe inside. The sheath enters the outer sphere through the same port as the ultrasound measurements, reaching close to the tangent cylinder, a few inches away from the equator. This sheath of course perturbs the flow—both globally and especially near where we're measuring.

3.2 Motor torque

The motor drives, by monitoring the electrical power used by the motors, report the torque needed to spin the shaft at the specified rotation rate. The power P is simply the torque Γ times shaft angular velocity Ω. Our drives report torque as a percentage of the nominal maximum torque, defined as $\Gamma_{nom.max} = P_{max}\Omega_{nom.}$, where, for our motors, $P_{max} = 7.5\text{kW}$ and $\Omega_{nom.} = 2\pi \times 60$.

Because the motors and the outer vessel are fixed in the laboratory frame, the torque is equivalent to the angular momentum transport in the system. It depends on the electromagnetic and mechanical coupling between the inner sphere and the sodium, and the sodium and the outer wall, as described in Chapter 2.

However, the torque reported will necessarily include friction from a combination of the shaft seals, the graphite packing, and the bearings. (The seals prevent sodium from leaking out the shaft; the packing keeps the seal in place and the shaft aligned and damps vibrations; the bearing align the shaft.) The friction is roughly constant with rotation

rate so its effect will be less important at higher rotation rates, where electromagnetic and hydromechanical torques dominate. The friction can change in time, however. For instance, if the shaft reaches a mechanical resonance and vibrates, the bearing can be strained and bearing will rotate less freely. Also, the packing can reorient or change shape, and the seals or bearing can get bits of leaked sodium or metal powder (from the shaft) stuck in them. Again, these changes are more likely to be noticed at lower rotation rates. These changes are also more likely to occur after the rotation rate is changed. In the runs, we waited after changing the rotation rate for the torque to settle. Also, when sodium leaks past the seals it eventually reacts and produces oxide, which creates different friction from day-to-day (until the sphere is disassembled, when the seals and packing get changed).

In short, care has to be taken in comparing torques from different runs, and in interpreting features in torque curves.

3.3 Ultrasound velocimetry

3.3.1 Basic principle

By reflecting sound from impurities (bits of sodium oxide, etc.) that travel with the flow the velocity component in the transmission direction can be determined as a function of depth [99]. Pulses of ultrasound are emitted into the fluid and then the echoes are recorded. The time delay between the pulse and each echo determines the depth of a particle. The velocity of each particle is determined by tracking particles. One profile is constructed using 32 pulses.

3.3.2 The transducer

The heart of the transducer is a piezo-electric crystal. The crystal changes its shape with an applied electric field, and conversely, produces electric fields when its shape changes. Thus sound (shape-altering vibrations) can be converted into an electric signal and vice versa.

There are two main difficulties in adapting an ultrasound transducer for use in sodium. First is temperature. Sodium experiments operate around $100°C$, which is close to or above the Curie temperature of many piezo-electric materials. The Curie temperature is the temperature above which the material loses its piezo-properties, directly analogous to the Curie temperature of ferromagnetic materials (above which the domains are lost). Piezo-crystals with high Curie temperatures are available commercially. The second difficulty—a far greater challenge—is coupling the transducer acoustically to the sodium. The front of most commercial ultrasound transducer is made of an organic epoxy that would be eaten by sodium. Also problematic, many of the materials that are inert to sodium do not wet sodium. Wetting of the transducer by the fluid is necessary to transmit sound into the sodium.

The ultrasound transmission is also controlled by the acoustical impedances of the crystal, housing, and fluid. The acoustical impedance, analogous to the index of refraction in optics, is related to the material sound speed c and compressibility γ: $Z = 1/c\gamma$. Equivalently the impedance can be expressed in terms of the density $Z = \rho c$. In general the transmission will be best if the intermediate material (the housing) has an acoustical impedance intermediate between the crystal and the fluid. To maximize transmission, the intermediate housing material should be an integer quarter-wave length, so that wave reflecting off the front and then back of the intermediate material constructively interfere

with waves that pass directly through.

The crystal we used has a resonate frequency of 4 MHz—the operating frequency of our processing unit[4]. The transducer housing was made of polytetrafluoroethylene (PTFE), commonly known by its trademark, Teflon. This housing material was chosen because it is electrically insulating (so as not to short the electrical connections on the crystal), capable of resisting high temperatures, inert to sodium, and having a similar acoustical impedance to sodium (to minimize mismatch losses). PTFE wets poorly to sodium however. We discovered that a thin layer of RTV (a silicone rubber adhesive) to the front surface wets sodium and allows coupling from the transducer to the sodium.

In the process of designing the transducer, we learned a lot about what *doesn't* work. The original hope was that sodium would wet the PTFE directly. Though claims of poor sodium-PTFE wetting have been made in the literature [32], it was not clear this was ever tested. Sodium is used to etch PTFE surfaces, through a self-arresting reaction—that is, sodium reacts with the first monolayer of PTFE and then stops. The hope was that this reaction would produce wetting, though it didn't. A thin black layer was apparent on the surface of the PTFE in spots after contacting sodium. Other materials that we tried, which wetted poorly were: copper, brass, stainless steel, aluminum, and gold-plated aluminum. Borosilicate glass (Pyrex) seemed to wet well, but it was difficult to construct a transducer housing with it. Some trials were performed with a thin Pyrex disk glued to the front of the PTFE housing, but the transmission was worse than with RTV only.

The wetting experiments, which sometimes overlapped with the magnetic field measurements, consisted of immersing the front of the transducer in sodium. We determined that a material wet sodium if (1) a layer of sodium was left on the surface after removing

[4]Graciously on indefinite loan to us by Yasushi Takeda.

the transducer, and (2) the transducer received echoes. Condition (1) was only necessary and not sufficient, as sometimes materials that appeared to wet did not transmit ultrasound. It did allow us to rule out some materials.

Besides having a good acoustical coupling to the sodium, there has to be particles in the flow to reflect sound. For good scattering, the diameters of these particles need to be of the order of the wavelength, which for 4 MHz ultrasound in sodium (c=2500 m/s) is $\lambda = 625\mu m$. Of course if the particles are too big, they won't trace the flow well. The concentration of particles needs to be large enough so that, on average, there is a particle at each depth along the measurements chord, but not so large that all the sound is scattered before reaching the maximum depth.

We tried adding glass tracer particles, but it turned out that the bits of oxide, dirt, bugs (!), etc. that occur inevitably in our sodium are adequate scatters. In fact, it seems there were *too* many of them—in many trials, velocities past some depth could not be measured. This problem could also be due to impartial wetting, since the overall sensitivity would then be lower. The way we solved the problem, however, suggests the problem was too many scatterers. As shown in Fig. 3.6, by tilting the storage tank at an angle, so that denser particles will slide down toward the bottom corner and away from the intake tube, the sodium transferred to the sphere should be cleaner. With this cleaner sodium, we could measure velocities at larger depths than we could by transferring with the tank placed flat.

3.3.3 Transducer placement

We wanted to measure both radial and azimuthal velocities near the equator (where the biggest induced fields were), but had only one transducer. Therefore, we placed the

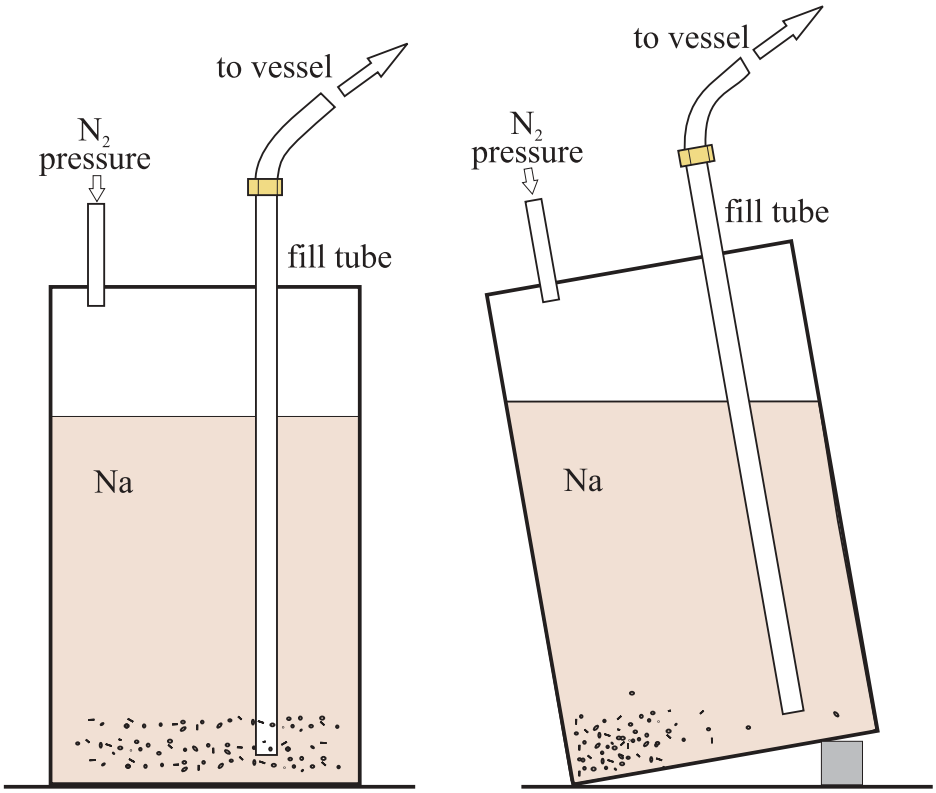

Figure 3.6: Hypothesized picture for why tilting the storage tank before transferring sodium produced better ultrasound measurements. Presumably the better ultrasound is due to a smaller (and closer to optimal) amount of impurity particles entering the sphere.

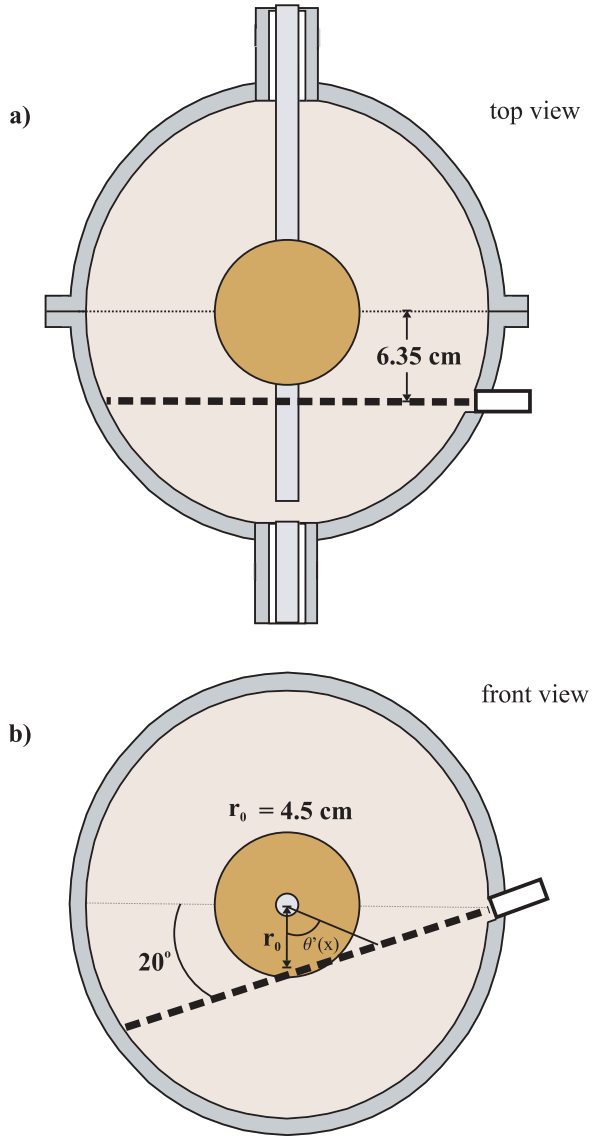

Figure 3.7: The location of the ultrasound measurements, which were along one chord. The angle $\theta'(x)$ is used to calculate the cylindrical radial and azimuthal components.

transducer to point above the rotation axis as shown in Fig. 3.7.

3.3.4 Reconstructing the flow using symmetries

The ultrasound probe measures velocities along a chord offset from the central axis of rotation. Thus the measured velocity, $v_m(x)$, includes both azimuthal and cylindrical radial velocities. The time-averaged toriodal and radial velocity profiles can be separated by decomposing the profile along a chord into its symmetric and anti-symmetric parts. The even part gives the azimuthal velocity, $v_e = v_\phi \cos\theta'(x)$, and the odd part gives the cylindrical radial velocity $v_o = v_r \sin\theta'(x)$. $\theta'(x)$ is the angle between r_0 (the shortest line connecting the rotation axis to the chord) and the line connecting the rotation axis to the chord position x, as shown in Fig. 3.7. We can express the two trigonometric relations as:

$$\cos\theta'(x) = r_o/\sqrt{r_o^2 + (x - L/2)^2},$$

$$\sin\theta'(x) = \sqrt{r_o^2 + (x - L/2)^2},$$

where $L = 29$ cm is the chord length. The rotation axis along x is at $L/2$.

3.4 The experiments

The liquid sodium is contained in a 31.2 cm hollow sphere of 304 (nonmagnetic) stainless steel. We studied flows driven by: (1) co-rotating impellers, and (2) a rotating inner sphere. In (1) the impellers were titanium and had 12.7 cm diameters. They were of opposite helicity and entered the sphere from either pole (see Fig. 3.8). In (2), three different 10 cm dia. spheres were used: solid copper, a hollow copper shell of thickness ≈ 3 mm, and a stainless steel shell. The shafts in all experiments were made of nonmagnetic stainless steel and were 2.54 cm dia. each was belt-driven by a 7.5 kW electric motor.

Two coils in near-Helmholtz configuration supply the external field concentric to the axis of impeller rotation. The applied field varies approximately 10% from the center of the sphere to the outer edge, decreasing away from the center along the axis of rotation, and increasing in the other two perpendicular directions. A Hall probe just outside the sphere next to one shaft measured the field in the direction parallel to the applied field.

For the impellers runs, three somewhat crude Hall arrays—different from the Hall array described in Sect. 3.1—were used: a 15 cm dia. ring (6 probes) encircling one pole azimuthally, a pole-to-pole arc (8 probes), and an equatorial arc (7 probes) all of which measure fields perpendicular to the applied field (see Fig. 3.8). The equatorial array was augmented by two single Hall probes, one of which was offset slightly from the equator.

Table 3.1 shows relevant experimental parameters for our system. More detail regarding the experimental apparatus can be found in Peffley et al. [83].

We perform experiments both with baffles and with smooth walls. The baffles are thin stainless steel plates that run from pole to equator in each hemisphere. They extend 5% of the sphere diameter. These baffles increase the ratio of poloidal to toroidal flow, as originally motivated by Dudley and James's study [31] of simple velocity fields in a spherical geometry and their ability to self-generate. We found in Peffley et al. [83] that a trend toward self-generation using pulse decay measurement was only possible with these baffles in place. In this experiment, the baffles' role is to create topographic variation at the vessel wall, analogous to topographic variation at the Earth's core-mantle boundary.

Experimental runs were performed using the following procedure. The impellers were spun at a fixed rotation rate, and the field was incrementally increased through its full range. The maximum field obtainable was 2×10^3 G. However, the magnets heated throughout the day and thus lowered the maximum obtainable field value. For each field

value, data were taken for several seconds (typically sixteen seconds).

3.4.1 Contribution of author

The author took the lead in most aspects of running the experiments, including cleaning, maintaining, deciding which measurements to make, and analyzing the data. The author also designed and built the Hall array (with some machining assistance) and developed the least squares software. For the experiments presented in Chapter 4, the author worked together with Nicolás Mujica. The two also worked together in the wetting experiments that ultimately allowed the ultrasound transducer to transmit in sodium. Applying the WKB analysis of Ji, Goodman, and Kageyama was first performed by Bill Dorland but reproduced independently by the author. The simple model in the truncated model in Chapter 2 was the idea of Dan Lathrop, and was implemented in various carnations by him and others, including the author.

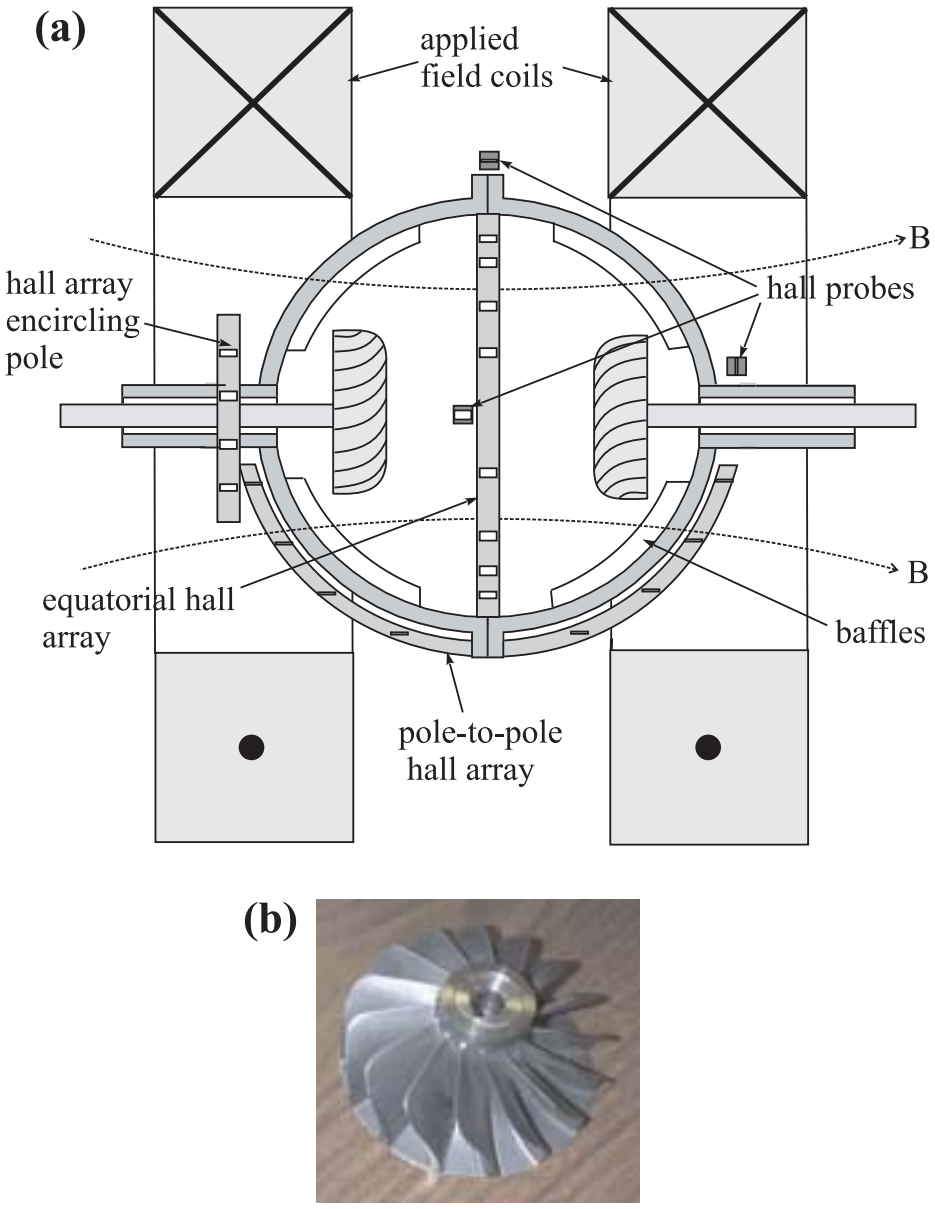

Figure 3.8: Impeller flow experimental apparatus, showing the spherical vessel, Hall probes, the coils that supply the external field, and the impellers driving the flow. The Hall arrays in these runs are cruder than the array used in spherical Couette experiments.

Symbol	Description	Value
b	Impeller radius	6.35 cm
b	Inner sphere radius	5 cm
a	Vessel radius	15.6 cm
η	Sodium magnetic diffusivity	830 cm^2/s
ν	Sodium kinematic viscosity	7.39×10^{-3} cm^2/s
ρ	Sodium density	0.927 g/cm^3

Table 3.1: Important dimensional parameters for the experiment and sodium at 120°C. The meaning of b depends on the experiment, spherical Couette or impeller-driven, being performed.

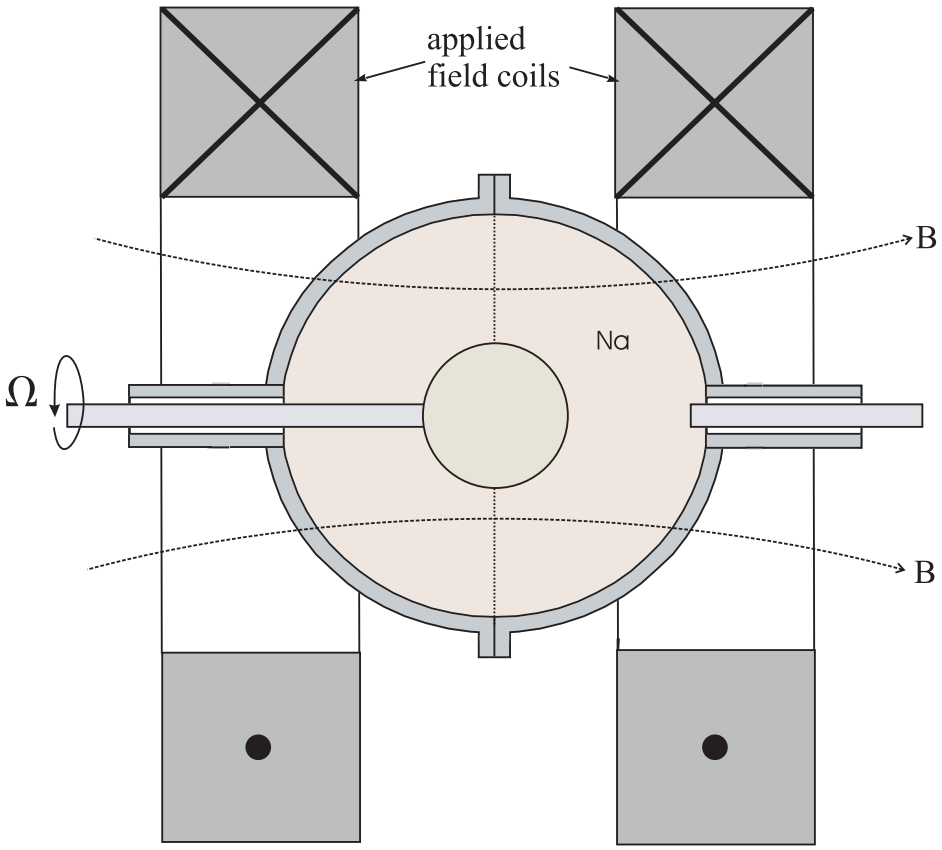

Figure 3.9: Spherical Couette experimental apparatus, showing the spherical vessel, the coils that supply the external field, and the rotating inner sphere that drives the flow.

Chapter 4

Spherical Couette Results

4.1 Evidence for the MRI

Though the rich dynamics exhibited by these experiments are interesting in their own right, they are most notable for their resulting from the magneto-rotational instability (MRI). We begin, therefore, with the evidence that the MRI is in fact what we observe.

4.1.1 Magnetically-induced instabilities

Our primary observation, consistent with what is known about the MRI, is that above some threshold external magnetic field B_c, oscillations are spontaneously excited in the coupled magnetic and velocity fields. Compare, for instance, the two induced field time series in Fig. 4.1, taken at the same rotation rate but below and above B_c. Below B_c (Fig. 4.1a), the induced field is featureless and turbulent, while above (Fig. 4.1b) it consists of a precessing $m = 1$ pattern. Ultrasound Doppler velocimetry measurements show that the oscillations are coupled to the velocity, as seen in Figs. 4.2 and 4.4. We refer to the onset and saturation of these oscillations as our primary instability.

Note in Fig. 4.1 how the $\vec{S}^1_{1b}$ coefficients have identical time dependence to the $\vec{S}^1_{3b}$ coefficients. From the selection rules in Chapter 2, both modes are allowed from the postulated $\vec{S}^1_{2v}$ velocity disturbance interacting with the applied field. From now on we

take modes with the same m and same parity with respect to reflection about the origin to be part of the same mode, denoted by Om for odd and Em for even modes. The $m = 0$ (axisymmetric) modes often vary independently from their same parity counterpart, so we sometimes specify the l value there.

Also consistent with the MRI—indeed, key to its astrophysical importance—is that at the instability onset the torque needed to spin the inner sphere increases, as increased amounts of angular momentum are carried from the inner sphere to the fixed outer sphere. Figure 4.3 shows the torque increase along with the variances for all the modes for a fixed rotation rate as the applied field is increased. The increase in the torque occurs at the same external field as the increase in the $O1$ variance.

In addition to turning on at a finite applied field (for systems with finite diffusivity) the MRI is also known to turn off at high fields. This feature is seen in Fig. 4.3 also, where, for instance, the $O1$ variance crashes at $B_{ext} \approx 1000$ G. When one mode disappears, other modes come to dominate. Figure 4.5 shows time series of the Gauss coefficients for these secondary instabilities, which occur at larger applied field.

Which mode dominates depends on both the applied field (Lunquist number S) and rotation rate (magnetic Reynolds number R_m). By independently varying the rotation rate and external field, we have navigated the (S, R_m) parameter plane and determined the regions where different modes dominate (Fig. 4.6). Rough conversions from dimensionless numbers to real units:

$$B(G) = S \times 200, \qquad \Omega/2\pi(Hz) = R_m \times 2.$$

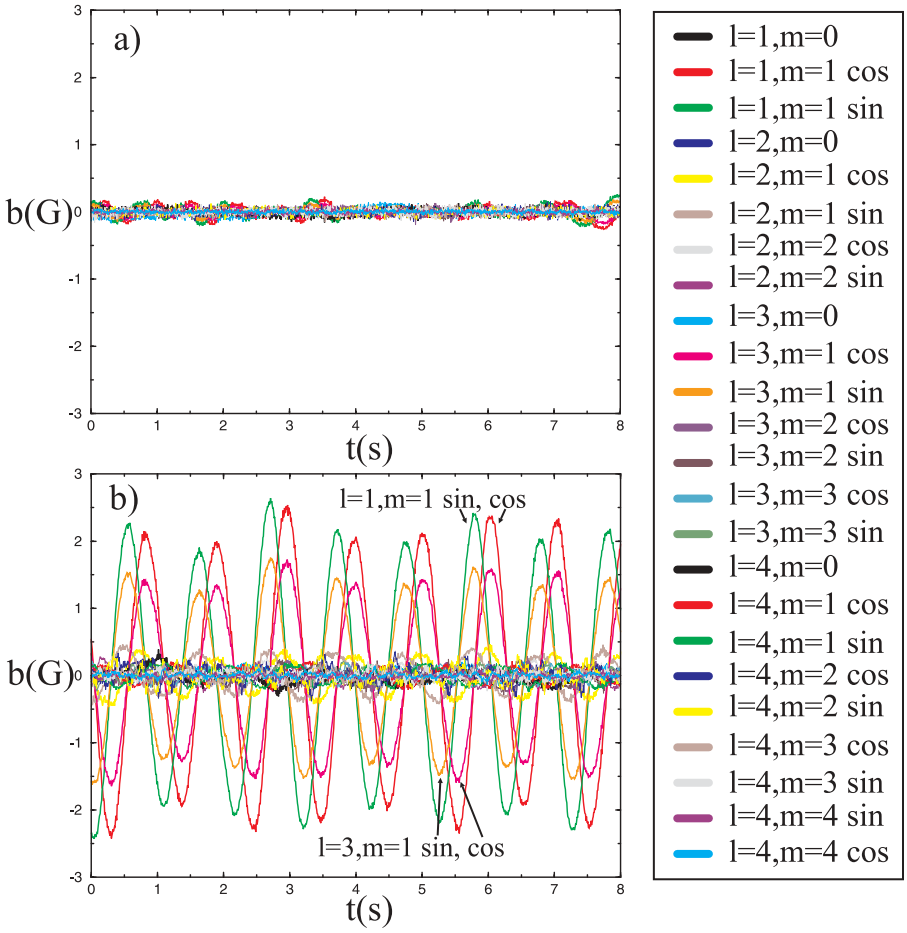

Figure 4.1: Time series of Gauss coefficients before and after the primary instability. For the same rotation rate, $\Omega/2\pi = 20$Hz, at (a) $B_{ext} = 93$ G, the magnetic field is largely broadband and turbulent with fluctuations of amplitude $< 0.1\%\, B_{ext}$ while at (b) $B_{ext} = 388$ G, the magnetic field is characterized by larger ($\sim 1\%\, B_{ext}$), regular $\vec{S}^1_{1b,3b}$ fluctuations. The cos and sin components are out of phase by 90°, indicating that the $m = 1$ pattern is precessing.

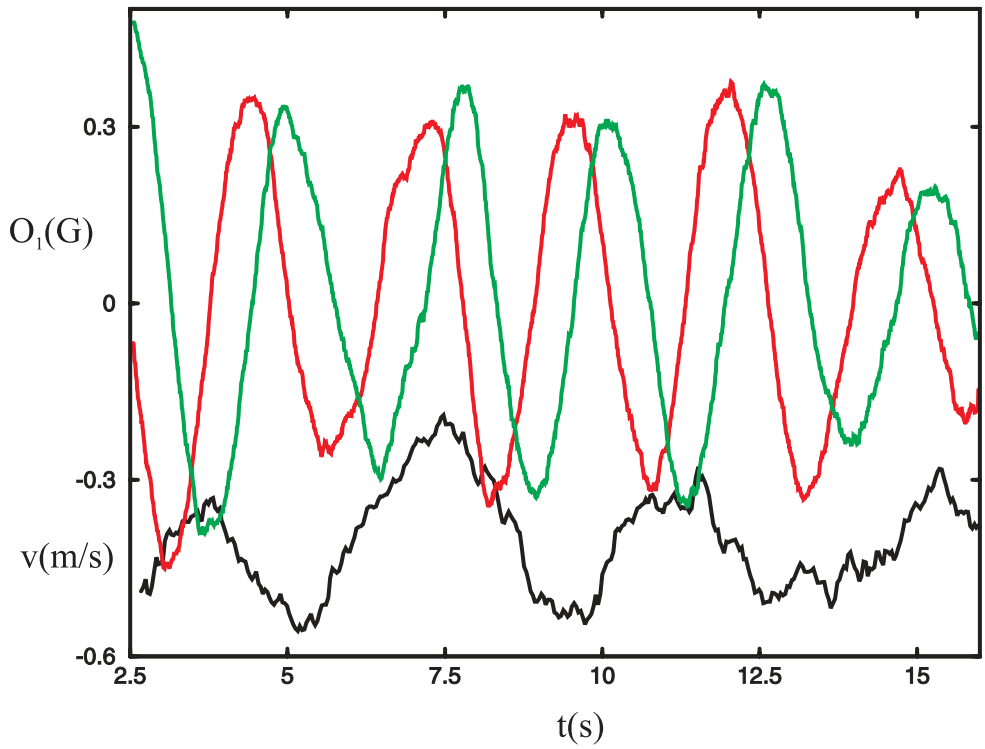

Figure 4.2: Time series of the $O1$ coefficients and the velocity at a point in the sphere. The red and green curves represent the cos- and sin- coefficients. The velocity and magnetic fields have the same frequency, showing the dual nature of the instability.

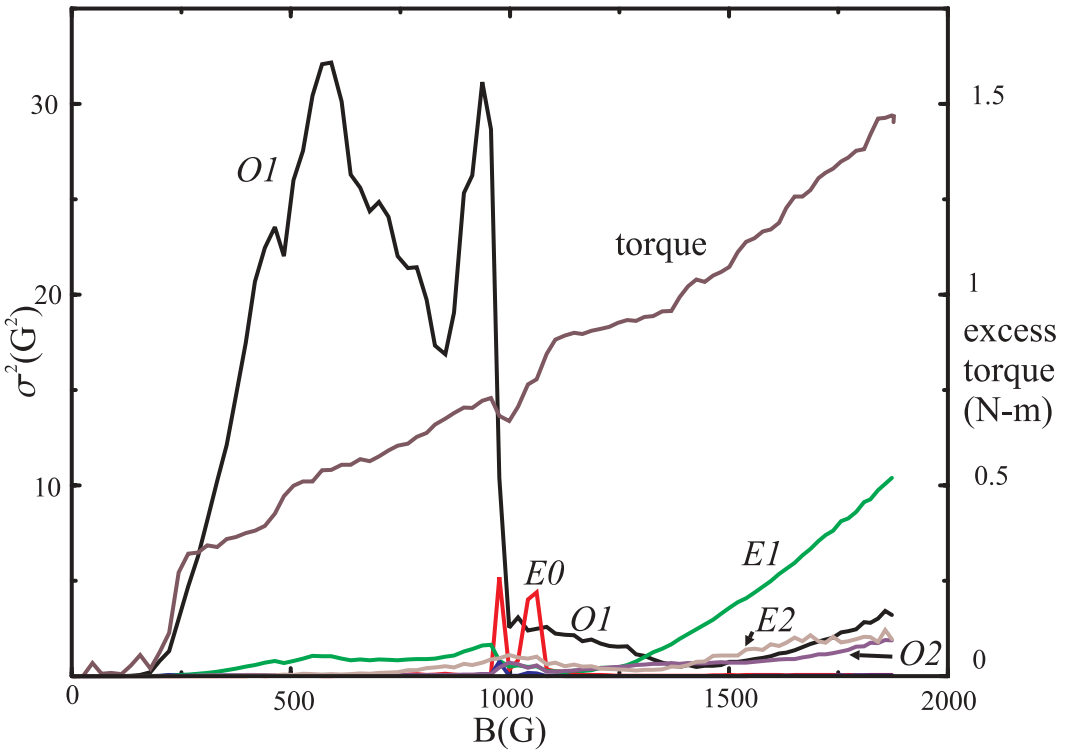

Figure 4.3: Excess torque and variance of the induced field Gauss coefficients for a fixed rotation rate $\Omega/2\pi = 30$Hz as the applied field is varied. The variance quantifies the fluctuation about the mean: $\sigma_b^2 = \langle (b - \langle b \rangle)^2 \rangle$, where $\langle . \rangle$ denotes time averages.

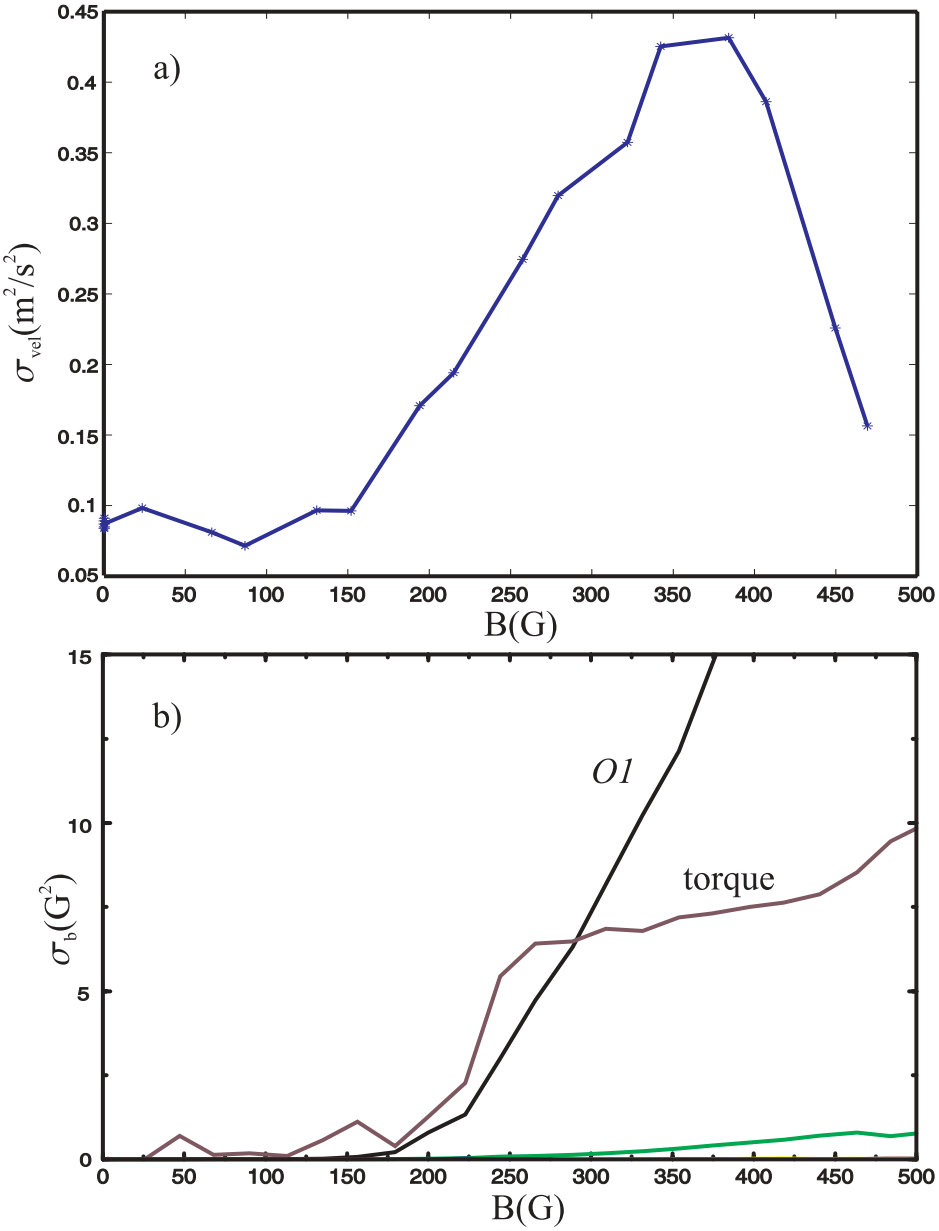

Figure 4.4: Velocity variance increases with the induced field variance and torque. The velocity in a) was taken at a depth of 15 cm (near the tangent cylinder), at $\Omega/2\pi = 30$ Hz. The velocity fluctuations at this depth decrease before the induced field fluctuations. b) shows the same data as in Fig. 4.3, which was also at $\Omega/2\pi = 30$ Hz.

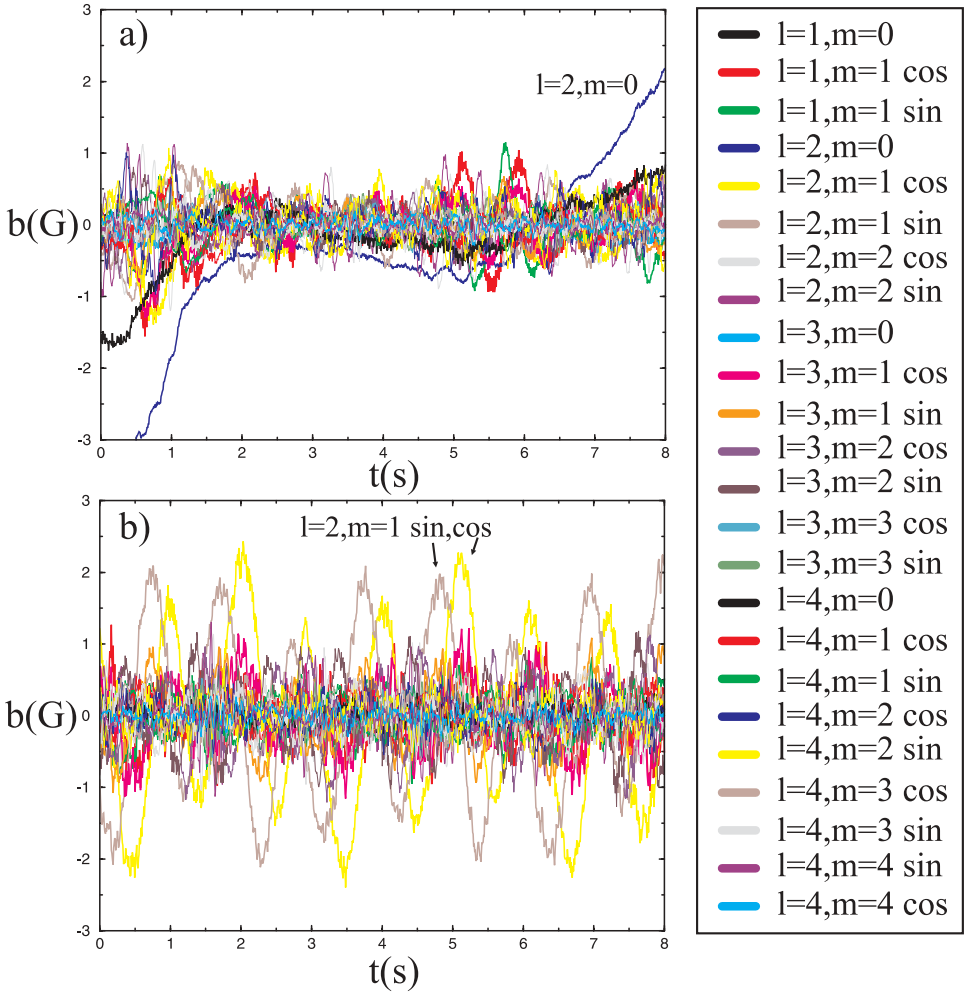

Figure 4.5: Time series of Gauss coefficients for two secondary instabilities. For the same rotation rate as Fig. 4.1, $\Omega/2\pi = 20$Hz, at (a) $B_{ext} = 881$ G, the dynamics are characterized by largely-aperiodic fluctuations in the $\vec{S}^0_{2b}$ coefficient, and at (b) $B_{ext} = 1430$ G, by regular fluctuations in $\vec{S}^1_{2b}$.

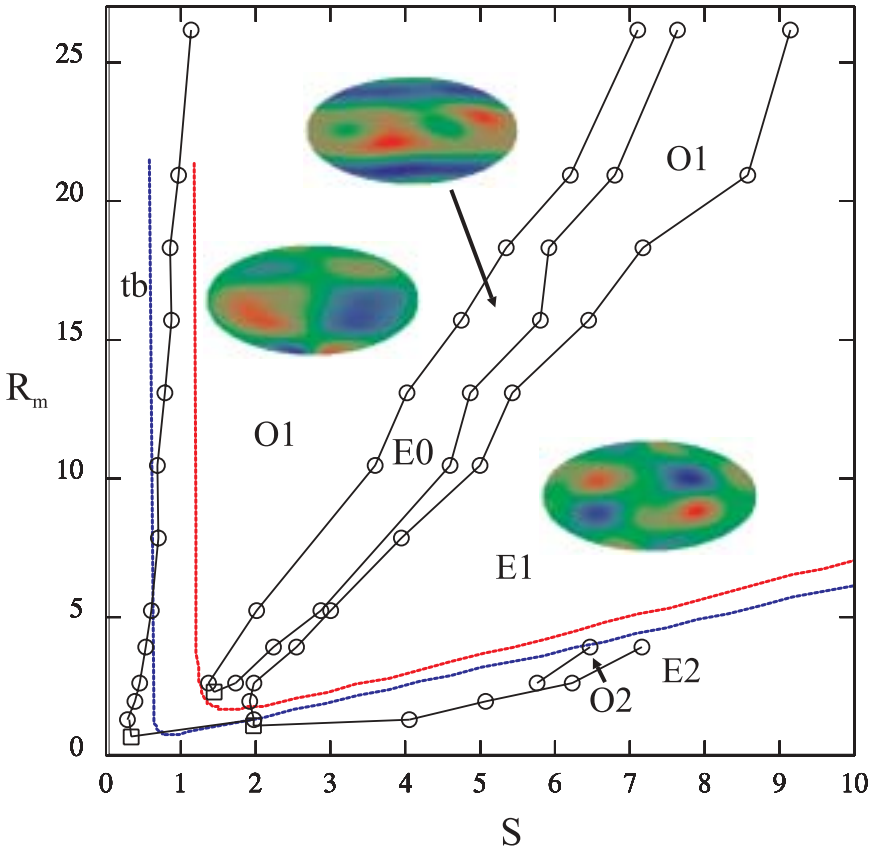

Figure 4.6: Phase diagram of saturated states. Regions are defined by the mode with the largest variance (see Fig. 4.3). Some secondary instabilities show hysteresis; these data are for increasing Lunquist number S, for fixed magnetic Reynolds number R_m. The lowest magnetic Reynolds number R_m and Lundquist number S for these states (□) is obtained by extrapolation, as described in Fig. 4.9. Also shown are theoretical stability boundaries for the longest wavelength (red) and second longest wavelength (blue) instabilities, calculated from the local MRI dispersion relation (see Chapter 2). Also shown for some regions are representative cylindrical radial component of induced field at one time reconstructed from Gauss coefficients. Color indicates intensity: red (positive), green (null value), blue (negative).

4.1.2 Base state has the right average properties

For the MRI to occur, the flow has to have a rotation rate profile that decreases with cylindrical radius. For the flow to be centrifugally stable, the angular momentum profile must *not* decrease with cylindrical radius. Both conditions are contained in the requirement: $0 < \zeta \sim 2 + \partial \log \Omega / \partial \log r < 2$. As seen in Fig. 4.7, this condition is met in our experiments, as $\zeta \sim 0.4 - 0.6$, except in thin boundary layers (see Sect. 4.2.1 for discussion of error). Thus our flow has a profile quite close to a Keplerian profile, where $\zeta = 0.5$.

On this note, there is a major departure between our base state and the base state of theoretical and numerical studies: ours is turbulent. Indeed, the MRI is important astrophysically precisely because it provides the turbulence that would be otherwise missing, and without which the accretion models would not work.

This discrepancy is double-edged. While the turbulence in the base state makes identifying the dynamics in our experiment with the MRI less straightforward, it also makes our results potentially more interesting. They provide strong evidence that the MRI—and the associated increase in angular momentum transport—occurs in the presence of preexisting hydrodynamic turbulence.

Other features in our experiment that differ from theoretical studies are the induced toroidal field and poloidal motions in the base state.

4.2 More detailed results

From here on, we provide more detail to the results above. Some of the results, however, only lead to more questions. We begin with a discussion of errors.

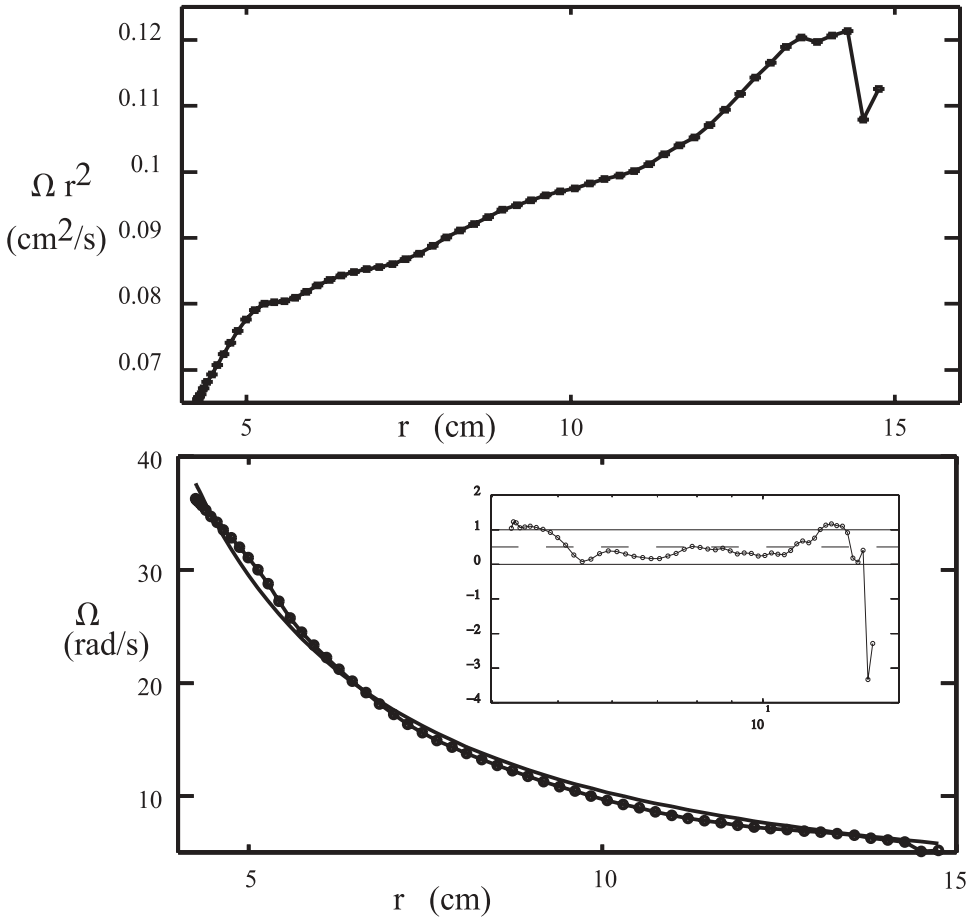

Figure 4.7: Zero field angular momentum and angular velocity profiles from ultrasound velocimetry measurements. The mean angular momentum density (a) shows that except for thin boundary layers the system is stable to centrifugal instabilities. The rotation curve (b) decreases with cylindrical radial difference from the center, a necessary condition for the base state to be unstable to the MRI. A $\Omega \sim r^{-3/2}$ Keplerian profile is shown for comparison. The inset shows the index ζ, with the Keplerian value $\zeta = 0.5$ indicated by a dashed line. These measurements were made for an inner sphere rotation rate of $\Omega/2\pi = 30$ Hz.

4.2.1 Errors

The errors in the Gauss coefficient amplitudes are estimated to be less than 10%. This estimate comes from comparing standard deviations at the same rotation rate for runs before and after the sphere and array were rebuilt. As mentioned in Sect. 3.1.3, the largest errors in Gauss coefficients come from the probes being in different locations than the probe locations in the matrix $\mathbf{M}$. The variation in placement from rebuild to rebuild gives an estimate of this error. This is likely an overestimate as there are dynamical differences from run to run as well (that is, two consecutive runs without rebuilding are not identical).

The error estimate in the torque data is also around 10%, but is more difficult to asses due to the confounding friction losses in the seals, packing, and bearings. The estimate is for the higher rotation rates and becomes worse at lower rotation rate. An indication of the torque error in Fig. 4.3 is given by the fluctuations before the instability onset.

In the velocity data, the number of ultrasound pulses per profile (32) gives a statistical basis to assess error; however, the largest source of error comes from decomposing the profiles into azimuthal and radial parts, which is more difficult to quantify. In particular, the largest error in the azimuthal velocity-based profiles occurs near the outer wall, where the measured velocity component is almost entirely in the radial direction. The sharp deviations in the angular momentum and ζ profiles (Fig. 4.7a and inset) near $r = 15$ cm are likely due to this. Other errors in the profiles are related to the signal quality deteriorating with depth along the chord. The asymmetry of the velocity with respect to the center, which can be seen in the velocity space-time diagrams (Fig. 4.24, described below), is due to this.

4.2.2 Defining regime boundaries

The amplitude, or standard deviation, of the instability—if it is a Hopf bifurcation—should increase as the square root of the applied field past critical $\sqrt{B - B_c}$. However, because of background turbulence (and possibly geometric imperfections), this transition is made imperfect. As we saw in Chapter 2, away from transition the effect of imperfections should disappear and the amplitude should converge to the "perfect" $\sqrt{B - B_c}$ dependence. We define the critical magnetic field for the primary instability as the applied field where this perfect trend reaches zero variance, as shown in Fig. 4.8. The fitting range should be neither too close to transition (where imperfections dominate) nor too far from transition (where Hopf bifurcation predictions break down). This procedure works best at high rotation rates, where the induced field is stronger and the rise occurs over a wider range of applied fields. Note how this definition produces a B_c that looks too high—that is, noticeable oscillations occur for $B_{ext} < B_c$. The procedure does provide a quantitative definition for onset, however. Furthermore, using this choice of B_c the data can be fit reasonably well using an imperfect bifurcation model (Fig. 4.8b), as in Chapt. 2.

We had a minimum obtainable rotation rate set by the motors and motor drives that was higher than the rotation rate below which no instabilities would be found. We nonetheless determined this minimum rotation rate by extrapolation, as shown for the $O1$ state in Fig. 4.9. The slope s from the σ^2 vs. B_{ext} plots (Fig. 4.8) is found to increase as Ω^3, as reflected in Fig. 4.9a. This dependence is consistent with the induced field energy ($\sim$ variance) being a fixed fraction of the viscous dissipation ($\sim \Omega^3$ for a turbulent flow) for a given fluid-field state; that is, the variance curves nondimensionalized by the interaction parameter and scaled by $\Omega^{3/2}$ collapse to a single curve (see Chapter 5). The critical external field value is found to increase linearly with rotation rate (Fig. 4.9). This finding

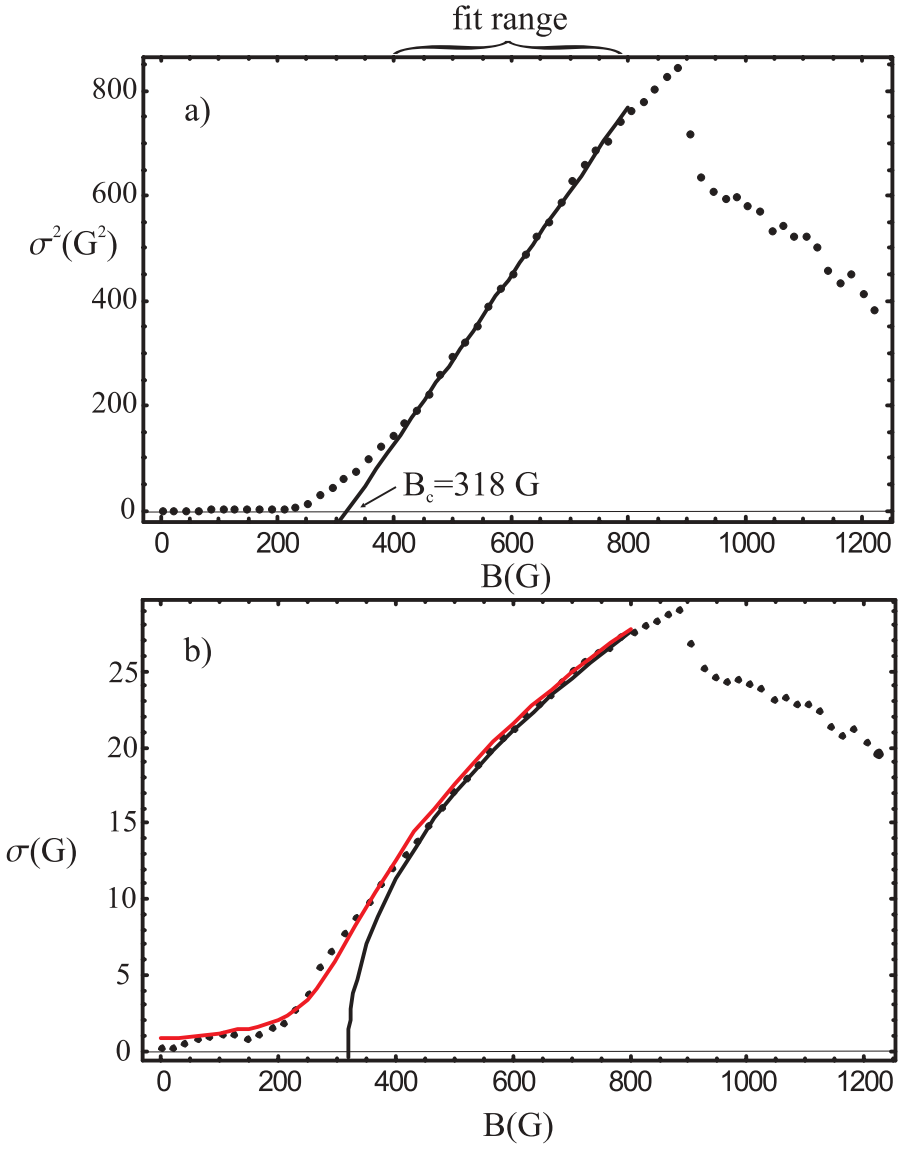

Figure 4.8: Defining B_c for the primary instability, for $\Omega/2\pi = 50$Hz. (a) Extrapolating the linear fit over the range shown to zero variance defines the critical external field value where onset occurs. In (b) the standard deviation (i.e., instability amplitude) is used in place of variance. Also shown is the best fit to an imperfect Hopf bifurcation, found from solving $0 = sB - B^3 + h$, where $s = 1.6$ is the slope from (a) and h was varied to minimize the error.

is in contrast to the local WKB analysis of Ji et al. [53], where B_c was independent of R_m.

Hysteresis

As mentioned earlier, some secondary instabilities show hysteresis. We always define the regimes by increasing the field for fixed rotation rate. Figure 4.10 shows the variances when the field is ramped down: the secondary instabilities occur at different external field values. In a coming section, we'll also see that hysteresis occurs when the field is held constant and the frequency increased.

4.2.3 Precession

Here we demonstrate more clearly to what extent precession occurs. Above B_c, the modes grow and reach a fairly clean limit cycle (Fig. 4.11b), the radius of which is approximately the expected value: $\sqrt{2}$ times the standard deviation σ. At fields significantly greater than B_c, though still within the $O1$ regime, the phase portrait (Fig. 4.11c) deviates from the limit cycle. In this subregime, a time series of the coefficients (not shown) shows substantial modulation of the $O1$ coefficients; the frequency of modulation is incommensurate[1] with the primary precession frequency. The modulation begins where the standard deviation deviates from the $\sqrt{B - B_c}$ trend. Apparently here is where higher order nonlinearities (than included in the normal form) control the saturation.

Just below B_c, the phase portrait (Fig. 4.11a) is consistent with a slowly decaying mode that is periodically excited by the turbulence. We might model the amplitude using the bifurcation normal form (Eqn. 2.37), with a negative growth rate and h replaced by

[1]Modulation by an incommensure frequency is called quasi-periodicity and occurs, among other places, in a supercritical regime of hydrodynamic Taylor-Couette flow.

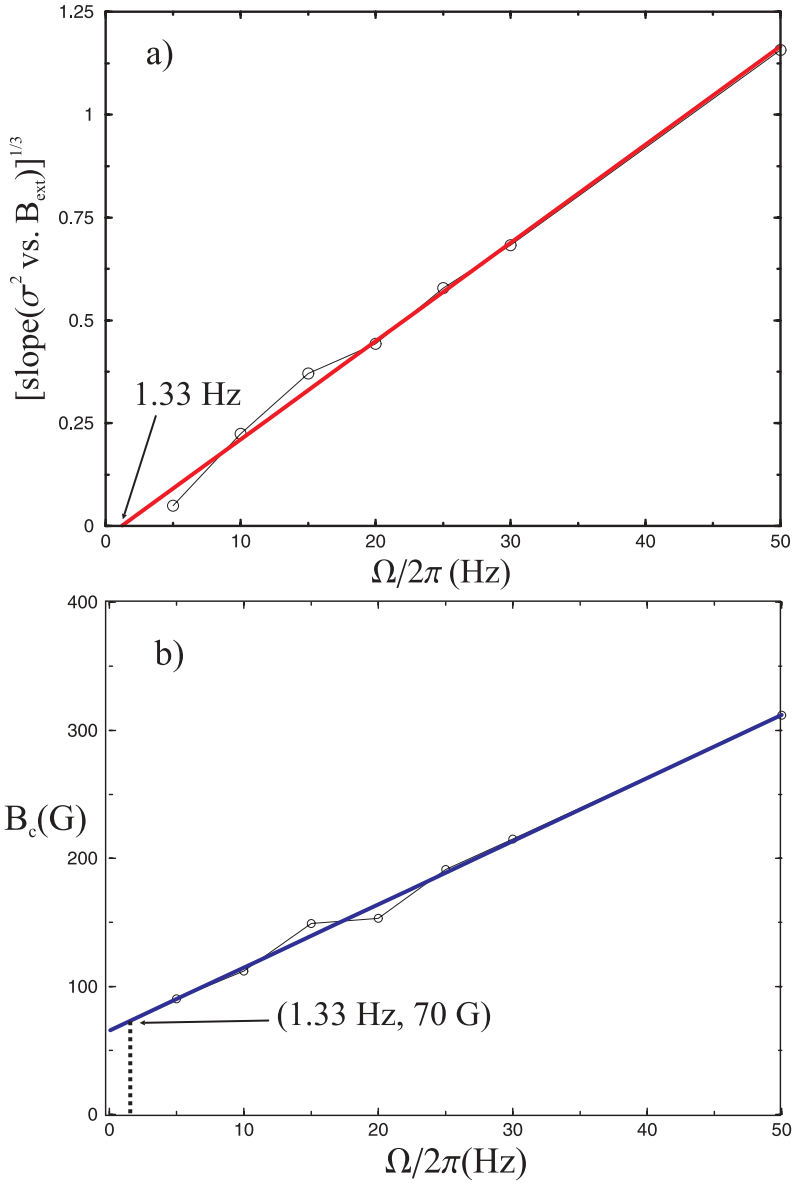

Figure 4.9: Extrapolation to find the bottom of the $O1$ region in the stability diagram (Fig. 4.6). (a) The slope s from Fig. 4.8a increases as Ω^3. Extrapolating the linear trend of $s^{1/3}$ vs. Ω to zero slope gives $\Omega/2\pi = 1.33$ Hz, below which the instability presumably doesn't exist. (b) The critical applied field increases linearly with Ω. Extrapolating the linear trend to $s = 1.33$ Hz gives a critical applied field value of 70 G at the lowest rotation rate where the instability occurs.

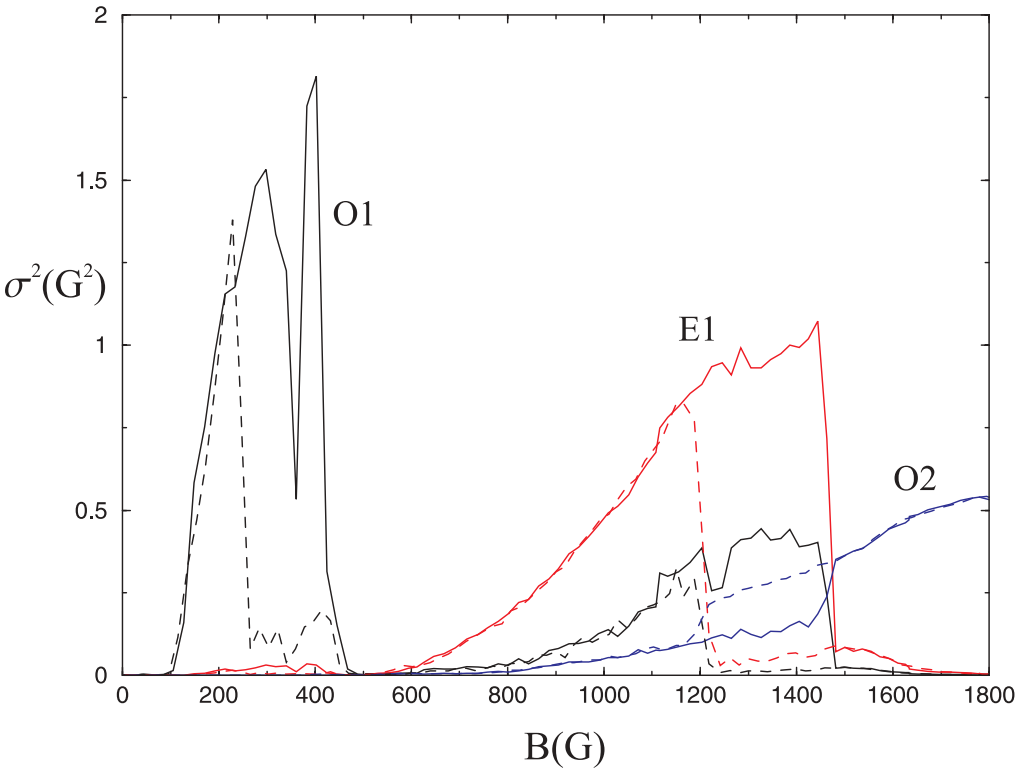

Figure 4.10: Mode variances showing hysteresis. At $\Omega/2\pi = 7.5$Hz, the applied field was ramped up (solid curves) and then ramped back down (dashed curves), showing that past the primary instability, the transition to states depends on the path taken. Color indicates the mode.

a random variable, perhaps having a stretched exponential distribution that is typical of velocity gradients. Though not shown, we tried such a model and found loose qualitative similarity to the time series of the $O1$ mode energy (Fig. 4.12). In that figure, the $O1$ amplitude is modulated by the background turbulence in all regimes, but to varying degrees.

Precession below onset

Surprisingly, in some runs, near zero external field the dynamics are better represented by Fig. 4.11b—modulated $m = 1$ precession. One would of course expect no precession below onset. The standard deviation below B_c in these runs increases linearly (though weakly) from zero applied field and then noses over before increasing sharply at onset. The effect is small enough to not be noticed when the variance is plotted (Fig. 4.3), but in the time series it is plainly evident. A frequency peak can be seen in the ultrasound measurements too for no applied field, but only near the tangent cylinder. The frequency peak gets suppressed at larger field and then reappears at onset—and at all depths.

The runs where the zero field precession appears have two qualities that are different from the others: the sphere is slightly off-center, and the shaft does not continue past the end of the sphere, as it does in Fig. 3.9. The sphere was off-center in these earlier runs because the shaft was too long; the fix was to move the sphere down from the end of the shaft, exposing more shaft into the flow. One run was performed with the sphere off center but with the current shaft configuration. The precession was markedly decreased there, but still more evident than with the sphere at the end of the shaft. Another difference is that with the sphere in the middle of the shaft, a hexagonal brass nut was exposed at the end of the shaft. With the sphere at the end, the nut was recessed in a circular

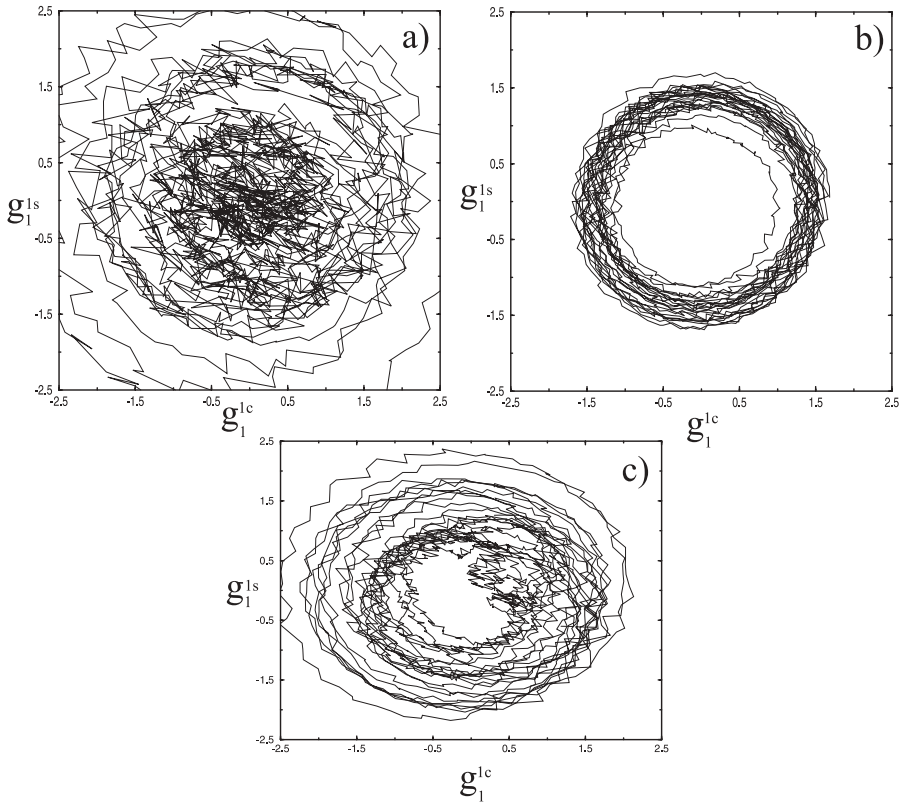

Figure 4.11: Phase diagrams of g_1^1 coefficients, at $\Omega/2\pi = 30$Hz. (a) Below critical $B_{ext} =$ 84 G, orbits spiral in toward and out from the fixed point at (0,0); in (b) $B_{ext} = 417$ G, the applied field is above critical and the orbit is nearly circular, indicating precession; in (c) $B_{ext} = 606$ G, substantially past critical (though still in $O1$) the orbit is more complicated, deviating from the limit cycle in (b). The units are standard deviations.

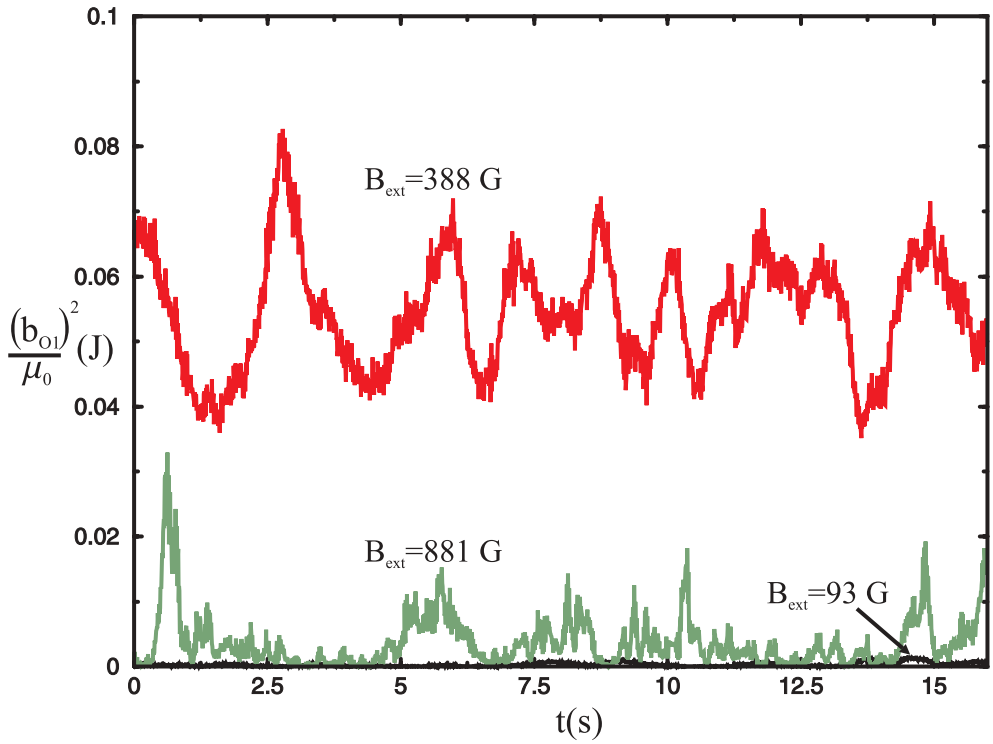

Figure 4.12: Magnetic energy density time series of the $O1$ mode for three values of external field. The states are the same as in Fig. 4.1a (black), Fig. 4.1b (red), and Fig. 4.5a, which were at the rotation rate $\Omega/2\pi = 20$Hz. The sine and cosine parts were squared and added together. The fluctuations result from the underlying turbulence.

indentation on the sphere. The precession is presumably related to these differences, but its cause remains a mystery.

Mode precession rates

Figure 4.13 shows the power spectra for the various induced field modes versus applied field for a fixed rotation rate of $\Omega/2\pi = 30$ Hz. There, over the range of applied field only three different modes have the largest variance: $O1$, $E0$, and $E1$. Some other modes have pronounced peaks—for instance the $E3$ spectra has a peak near $f = 5$ Hz at high field, and the $O2$ spectra at high field has a peak at $f = 2.5$ Hz. Both are m multiples of the main $E1$ peak.

The highest power spectra peaks for the $E1$, $O2$, and $E2$ spectra (Fig. 4.13)are shown in Fig. 4.14. Not seen in the previous figure (because it was outside the frequency range shown) is a peak of the $E2$ mode occurring at large field. Curiously, the frequency of this peak is not an integer multiple of the $O1$ frequency, is uncharacteristically large compared to other frequencies seen in our system, and is highly modulated, as seen in the inset.

Also notice that in a narrow band of field around $B_{ext} = 1000$—the $E0$ regime in the phase diagram (see Figs. 4.11, 4.1)—all the frequencies change considerably. This change is evident in Fig. 4.13 as well. The peaks correspond to highly modulated precession, though the modulation is more irregular than in the inset of Fig. 4.14. The modulation in those time series occurs on a time scale close to the $m = 0$ oscillations. In a movie of the reconstructed induced field taken from the $E0$ regime, this modulated precession is quite striking—for brief periods, a streak of $m = 2$ vortices at the equator whiz across the screen and then disappear. The frame for the $E0$ mode in Fig. 4.11 is taken from such a

segment of the time series. The $m = 0$ modes are one of the more interesting states in our system. We will return to them later.

4.2.4 Axisymmetric induced fields

Modes with azimuthal wave number $m = 0$ will not precess, and thus they typically do not have significant variances (with the exception of $E0$). The axisymmetric modes do have average values that change with rotation rate and applied field, however. Figure 4.15 shows the average values of the axisymmetric coefficients for a fixed rotation rate, as the applied field is increased. These values are prone to offset errors as discussed in Sect. 4.2.1, but the structural features are reliable. Note that when the $O1$ instability crashes the axisymmetric $l = 2$ and $l = 4$ components increase sharply and then at slightly larger external field decrease, and that the $l = 3$ component decreases.

4.2.5 Hysteresis revisited: frequency ramps

As mentioned above, the state of the system will depend on what path it was reached. We already showed the difference between increasing the field versus decreasing. Here we examine a run where the field is held constant and the frequency increased (Fig. 4.16). We draw attention to the points A and B in the figure.

At point A the torque increases sharply as the $O1$ amplitude increases, just like the instability onset for the external field ramps. But at point B the $O1$ amplitude increases again—an even larger increase—yet the torque is unaffected. Both average values for the axisymmetric modes change sharply at A and B as well. Furthermore, though the changes in the modes at A are in the same direction as B, the amplitude of change are not in proportion. The changes at A and B are clearly somehow connected, but the causal relation is not obvious!

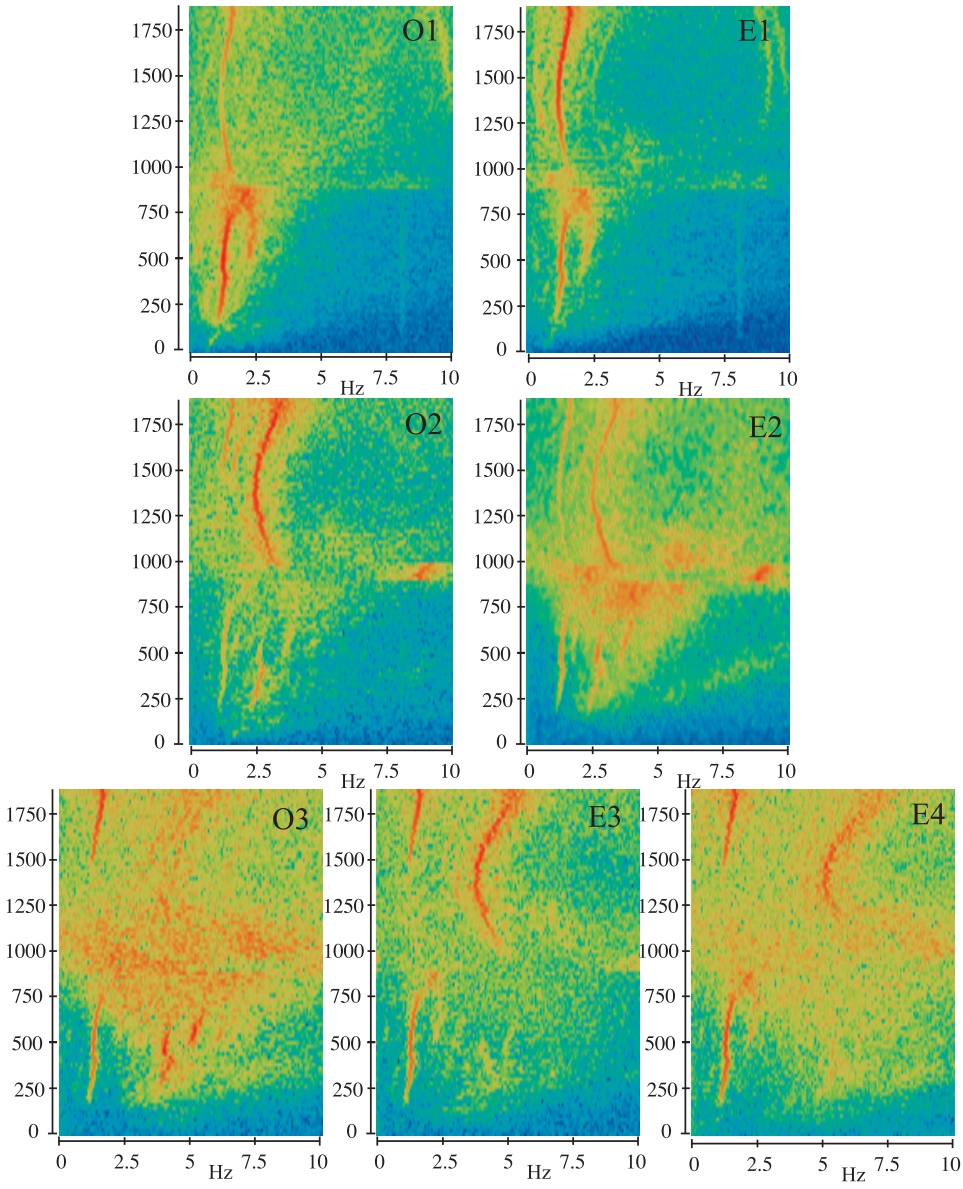

Figure 4.13: Power spectra of nonaxisymmetric induced field modes versus applied field at $\Omega/2\pi = 30$Hz. Each horizontal line in the figure is an induced field power spectrum, where color indicates intensity, from highest to lowest: red, green, blue. The scale is logarithmic. The $m = 0$ spectra are not shown because they are largely featureless—even the $E0$ mode, which over a range of external field is the mode with the largest variance.

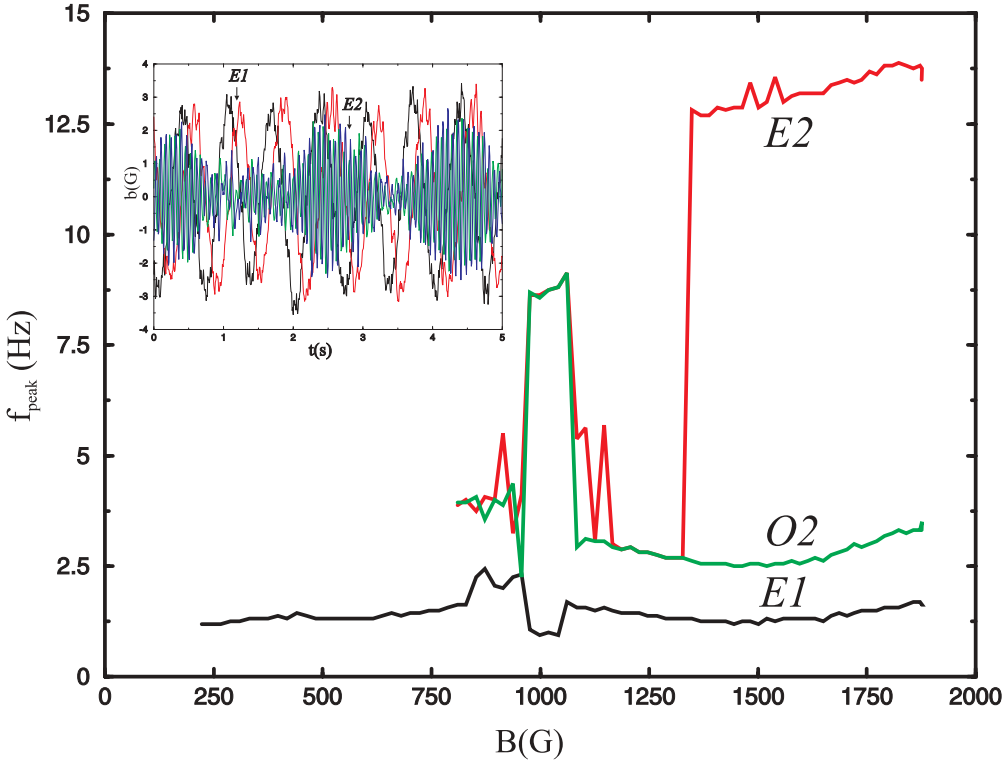

Figure 4.14: Power spectra peak frequencies versus applied field for $\Omega/2\pi = 30$ Hz. The inset shows a time series of the $E2$ and $O1$ modes at $B_{ext} = 1750$ G: both modes are precessing, but the $E2$ mode is highly modulated. The $O1$ frequency (not shown) is the same as $E1$.

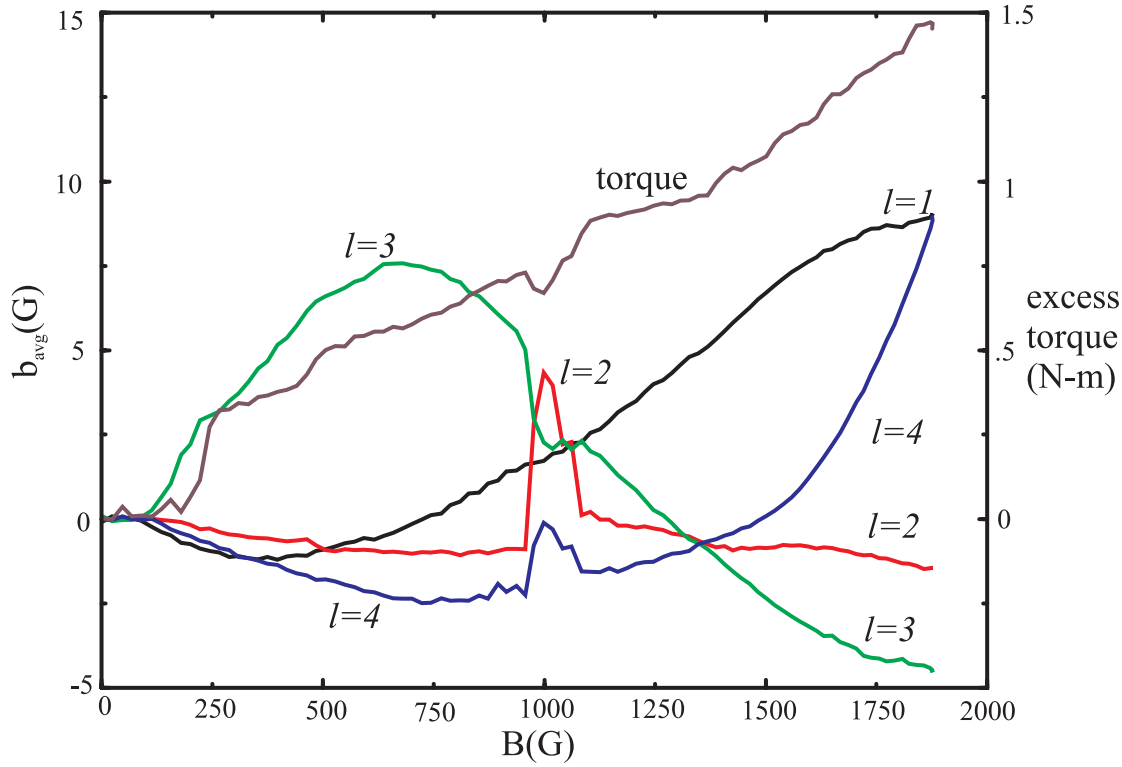

Figure 4.15: Time-averaged coefficients of axisymmetric states versus applied field for $\Omega/2\pi = 50$. Even for no flow, the coefficients have nonzero averages because the external field is not exactly perpendicular to the array; here we subtract an extrapolated trend for each coefficient fit from the range 0-100 G.

One might also wonder why at A the $O1$ primary instability increases in amplitude though it is already the dominant mode. This feature, however, is more readily explained. Consider a typical standard deviation curve at fixed rotation rate and ramped field (e.g., Fig. 4.3). After the $O1$ instability turns on, the amplitude rises as a Hopf bifurcation $\sqrt{B - B_c}$, but then deviates from this trend as the oscillations become modulated. This point of deviation occurs at larger fields for larger rotation rate. So the increase in $O1$ amplitude we see here is presumably where the system crosses from modulated oscillations into a pure Hopf region. It seems another sort of crossover happens again at point B.

Point B happens to correspond to a decrease in precession frequency, such as in Fig. 4.17. There, however, the external field was smaller and the transition to slower precession occurs at a lower rotation rate than in Fig. 4.16.[2] Not shown in Fig. 4.17 is the $E0$ standard deviation, which peaks at $\Omega/2\pi \approx 25$ Hz, near where it occurs on the phase diagram (defined as before); at only one point is the $E0$ standard deviation larger than $O1$, and only by ~ 1 G.

4.2.6 Toroidal field

As mentioned earlier, probes outside the sphere can only measure the poloidal component of the magnetic field. We placed a hollow cylindrical sleeve housing a Hall probe into the sodium to measure the toroidal field near the tangent cylinder, a few inches away from the equator.

Figure 4.18 shows the average toroidal field in the sleeve and its standard deviation for $\Omega/2\pi = 30$, as the applied field is ramped. For small values of applied field, the Lorentz force is presumably too small to alter the flow. The average toroidal field linearly becomes more negative as the applied field is increased. Over this range, it seems a differential

[2]The peaks are better defined there too, which is why we chose a different external field for that figure.

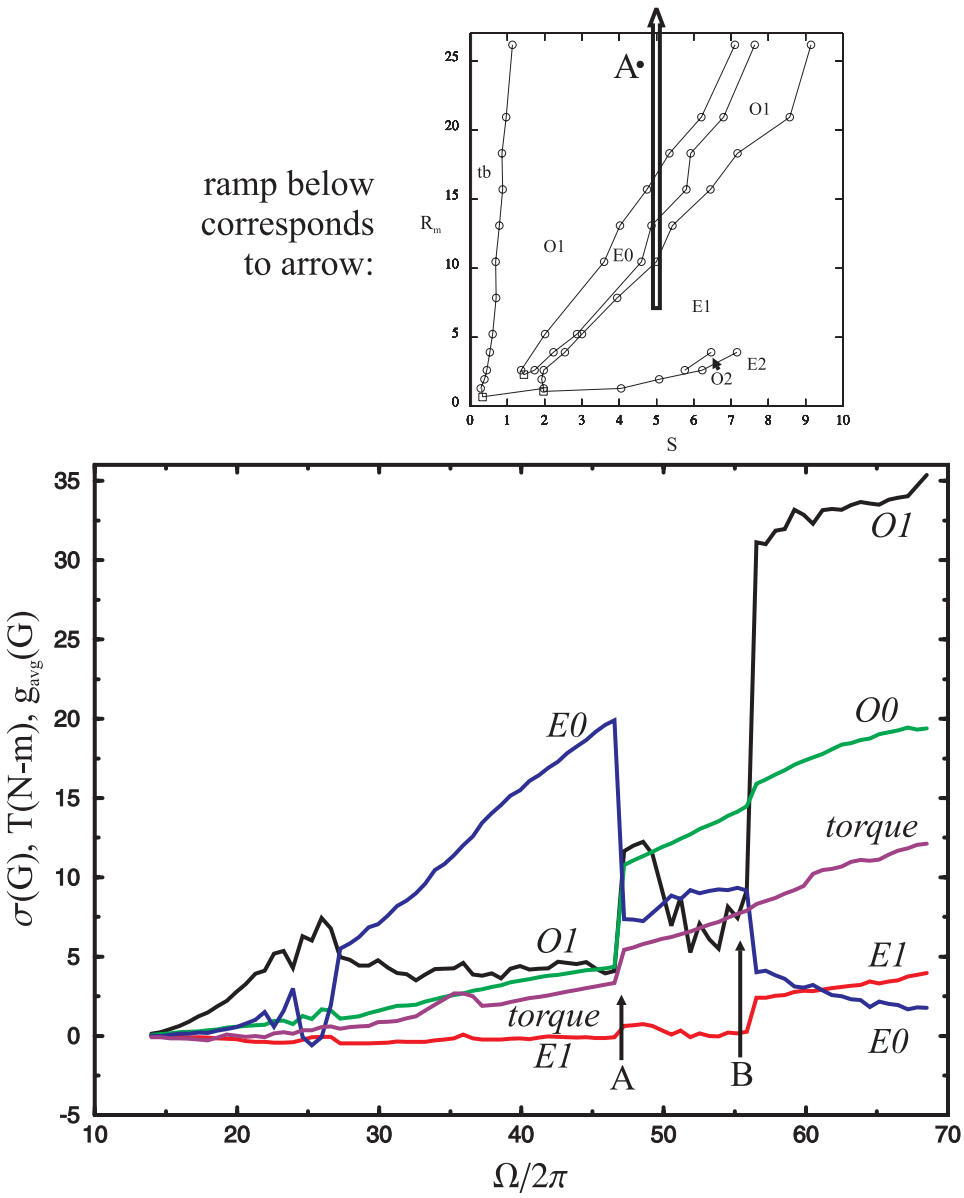

Figure 4.16: Torque, mode standard deviation (for $m \neq 0$), and mode average value (for $m = 0$) versus rotation rate for $B_{ext} = 1000\ G$. At the starting rotation rate (14 Hz), all values have been artificially set to zero. The field was turned on and then the motors. The field decreases approximately 50 G over the ramp due to coil heating.

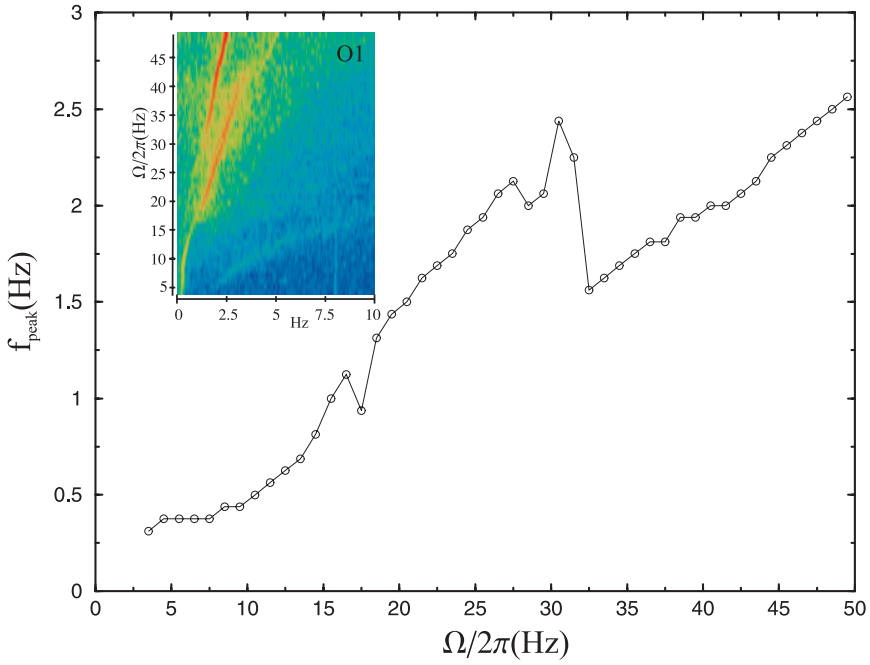

Figure 4.17: Power spectra peak frequency versus rotation rate at $B_{ext} = 700$ G for the $O1$ mode. The inset shows the full power spectra as a function of external field. There is a range of applied field where two incommensurate frequencies appear with comparable amplitude.

rotation profile converts a fraction of the external field into toroidal field. Note that at the instability onset (B_{ext} = 200 G), the trend becomes slightly more negative. Near $B_{ext} = 500$ the trend stops altogether and then reverses, only to turn sharply back toward (though still less negative than) the trend at $B_{ext} = 1000\ G$. Again, curious things happen at the $E0$ regime where the primary instability crashes. Past $\sim$ 1100 G, the toroidal field is roughly independent of applied field.

From the slope of the linear region in Fig. 4.18, the toroidal field in our sleeve is approximately 1/20 the applied field. From dimensional analysis, we would expect the ratio of induced toroidal field to applied field to be of order R_m. At a rotation rate of $\Omega/2\pi = 30$, the magnetic Reynolds number is $R_m = 15$, so we find our observed toroidal field is 300 times smaller than this prediction. This finding lends further justification to the small-R_m approximation we use in several places in Chapter 2.

Figure 4.19 is similar to Fig. 4.18 except the field is fixed ($B_{ext} = 300$ G) while the rotation rate is ramped. For an applied field of B_{ext} = 300 G, the average toroidal field strength increases linearly with rotation rate. Throughout the ramp the regime is $O1$. The slope of the time-averaged induced toroidal field for B_{ext} = 300 G is -0.65 G/Hz. From this slope, we obtain an empirical relation for the toroidal field in terms of the magnetic Reynolds number:

$$B_{tor}/B_{ext} = 4.3 \times 10^{-3} R_m. \tag{4.1}$$

4.3 Torque

With no field, the torque is quadratic in Ω, as seen in Fig. 4.20. For the run in this figure, we went to much higher rotation rates than any other run (though unfortunately we took no magnetic field data). These high rotation rates produce better torque measurements

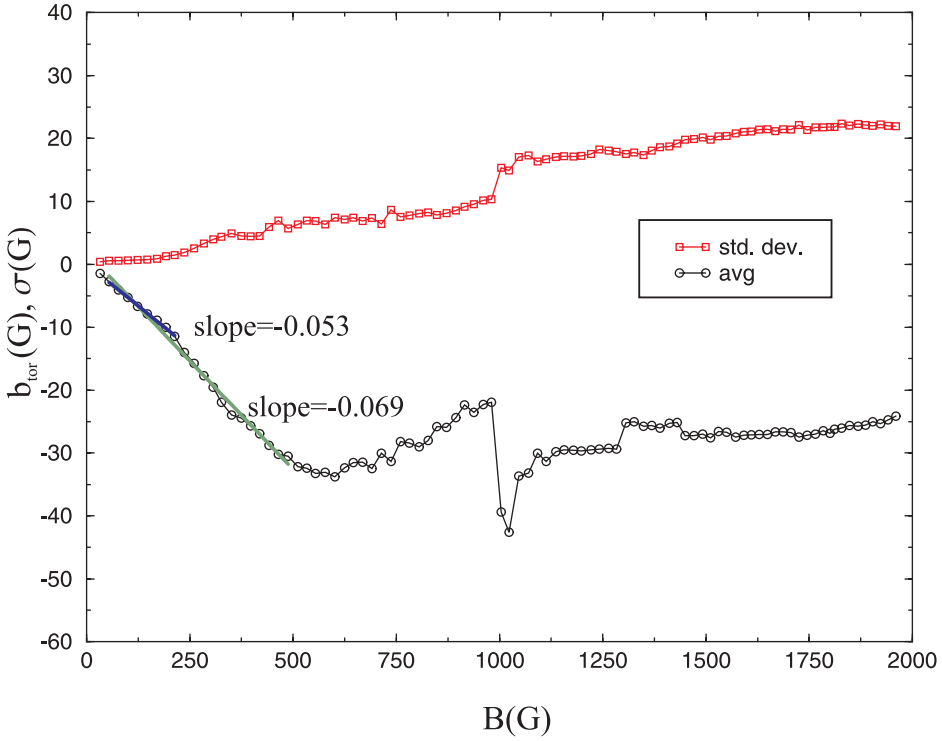

Figure 4.18: Toroidal induced field versus applied field for $\Omega/2\pi = 30$ Hz. Up to $B_{ext} = 500$ G, the time-averaged toroidal field increases approximately linearly with applied field. After the instability onset ($B_{ext} = 200$ G), the average toroidal field trend becomes slightly more negative, as can be seen by comparing the green and blue lines.

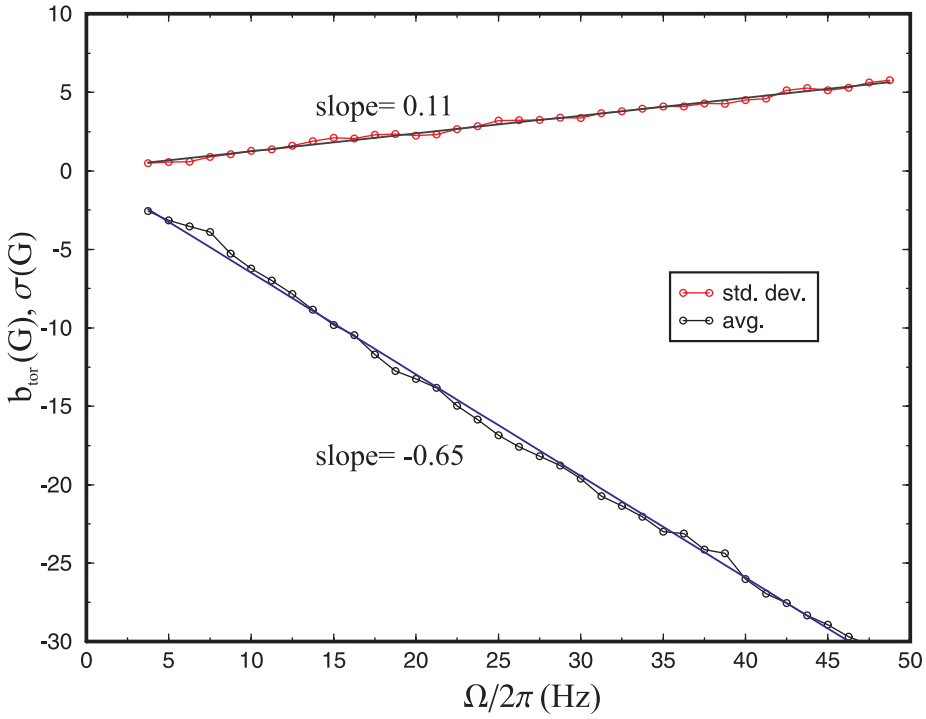

Figure 4.19: Toroidal induced field versus inner sphere rotation rate with an applied field of B=300 G. At all points the system was in the $O1$ regime.

because the friction from the packing and seals is a smaller percentage of the total torque. The quadratic torque increase seen with no field seen here is consistent with the standard turbulent drag model in Chapter 2 (Eqn. 2.45). Computing a skin friction coefficient C_D we find that it is of the order typical for when the boundary layers are turbulent [40]. The torque measurements are not precise enough to distinguish between a quadratic model and a model with logarithmic corrections due to laminar boundary layers.

We test the torque prediction at the end Chapter 2. In Fig. 4.3 we saw for $\Omega/2\pi =$ 30 Hz the torque increasing sharply as the primary instability turns on, decrease slightly when it crashes, and increasing in between. In Fig. 4.21 we look at at a higher rotation rate—the highest rotation rate where we ramped the magnetic field—where the effects of the seals will be a smaller fraction of the total torque. The prediction (Eqn. 2.50) holds at small fields: the torque increases as $\sim B_{ext}^2$ and then deviates from this trend near $N = 1$. However, the torque scaling thereafter is not independent of applied field as predicted. For a range of external field past $N = 1$, as seen in Fig. 4.21, the torque scales as $\sim B_{ext}$. This feature remains to be explained. The likely discrepancy is that the ratio of length scales $l_\parallel/l_\perp$ does not increase as $N^{1/2}$, the result from decaying turbulence (Eqn. 2.44). The torque does appear affected by the ratio of length scales: when the primary instability crashes (near $B_{ext} = 1500$ G) and the length scale perpendicular to the external field $l_\perp$ decreases (as no relatively large $m = 1$ vortices exist), the torque decreases.

Why, however, is there no sharp increase in torque at onset, as there was for $\Omega/2\pi =$ 30 Hz? It could be that at larger rotation rates the smooth quadratic torque increase with applied field comes to dominate over the torque increase due to the changing length scale (see second term in Eqn. 2.50). We have only limited quantitative measure of the changing length scale ratio (through the ultrasound measurement) and no quantitative prediction

of how the length scale ratio affects the torque relative to basic electromagnetic coupling. Further confounding matters, the torque curves for other runs at the same rotation rate look somewhat different in detail from Fig. 4.21.

4.3.1 Velocity measurements

We measure the velocity along a chord, as shown in Fig. 3.7. By time averaging the profile we can extract the radial and azimuthal components, from the anti-symmetric and symmetric components respectively, as described in Sect. 3.1.4. Figure 4.22 shows the angular velocity and angular momentum profiles as a function of cylindrical radius. We see that as the external field is increased the fluid close to the inner sphere becomes increasingly coupled to the inner sphere rotation rate.

Figure 4.24 shows space-time diagrams of the ultrasound data for $\Omega/2\pi = 2.5$ Hz. The direction is along the chord of measurement; decomposing the velocity into v_s and v_ϕ is only possible for average profiles. At $B_{ext} = 41$ G (Fig. 4.24b), notice that the flow seems to organize even before the primary instability. Also notice in Figs. 4.24c-f how the oscillations gradually become focused on the boundary of the tangent cylinder.

4.3.2 Transition states: axisymmetric oscillations

When the system transitions between the primary instability and the first secondary instability—the "$m = 0$ state" in Fig. 4.6—more complicated dynamics result. Unlike the other saturated states, which have periodic magnetic and velocity fields, the dynamics in this state seem to flip aperiocially between two distinct states. The characteristic time of this flippling is much longer than the period of the other saturated states, as in Fig. 4.25. The torque time series is correlated (or anti-correlated) with all the axisymmetric modes, as seen more clearly in Fig. 4.26.

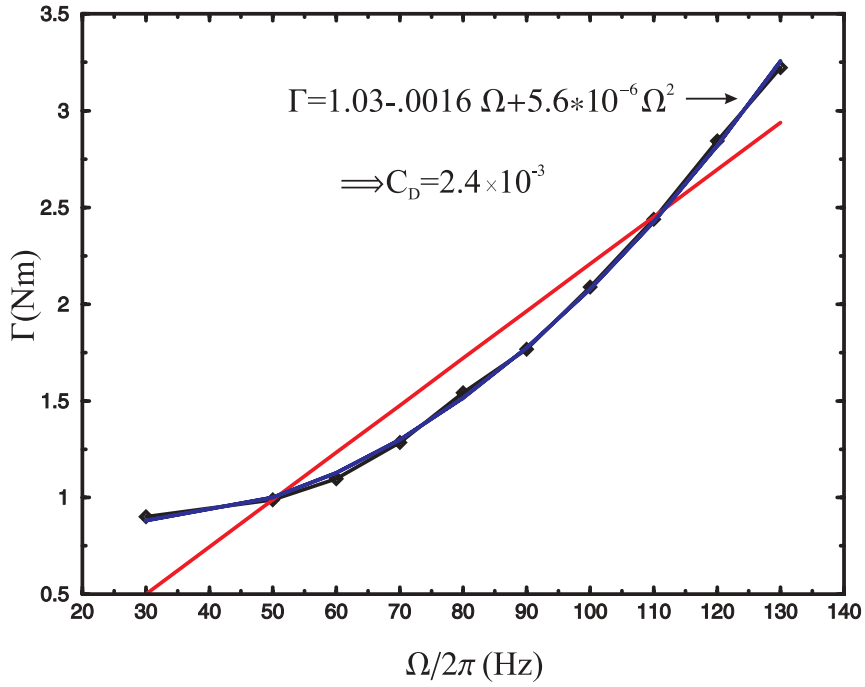

Figure 4.20: Torque versus rotation rate with no applied field, with quadratic and linear fits. Without applied fields the torque increases as the rotation rate squared, consistent with a standard turbulent drag model. The equation for the quadratic fit is shown. Assuming the non-quadratic parts are due to frictions from the seal and packing, the drag coefficient is $C_D = 2.4 \times 10^{-3}$.

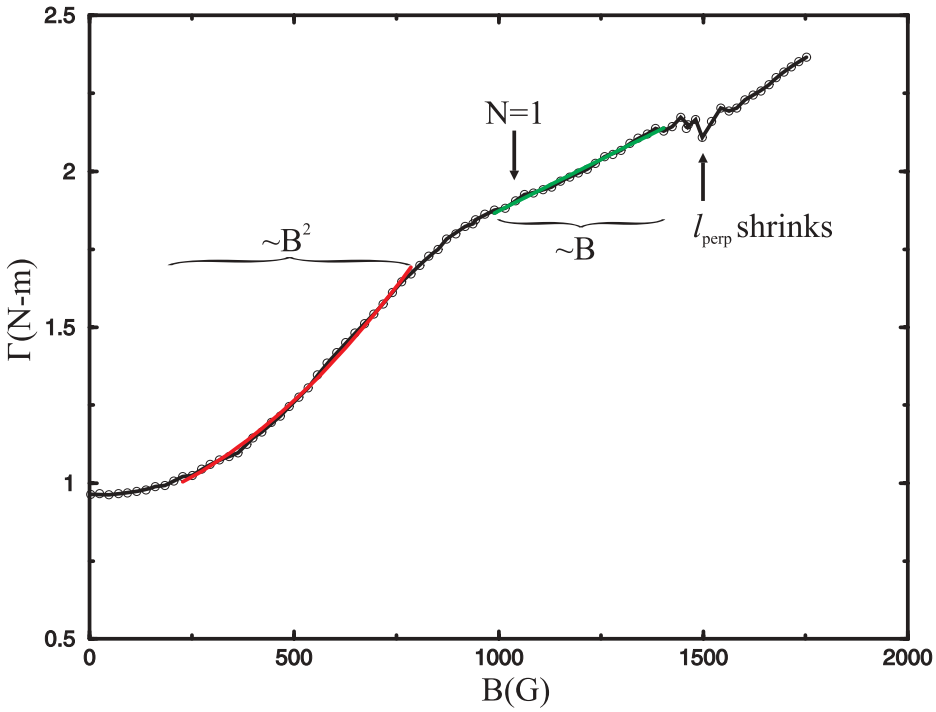

Figure 4.21: Torque versus applied field at $\Omega/2\pi = 50$ Hz. Quadratic (red) and linear (green) fits are shown. The torque changes scaling near $N = 1$.

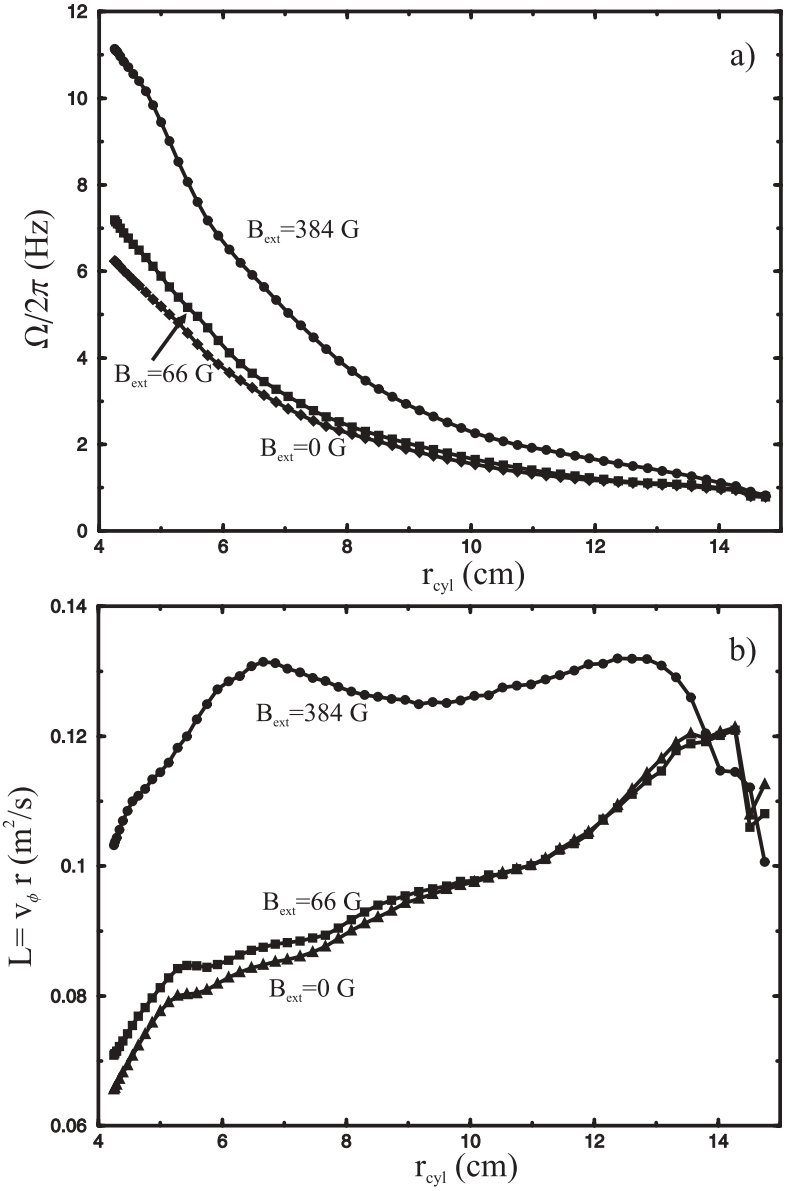

Figure 4.22: Velocity profiles for $\Omega/2\pi = 30$ Hz, for three values of applied field. a) shows the angular velocity and b) the angular momentum.

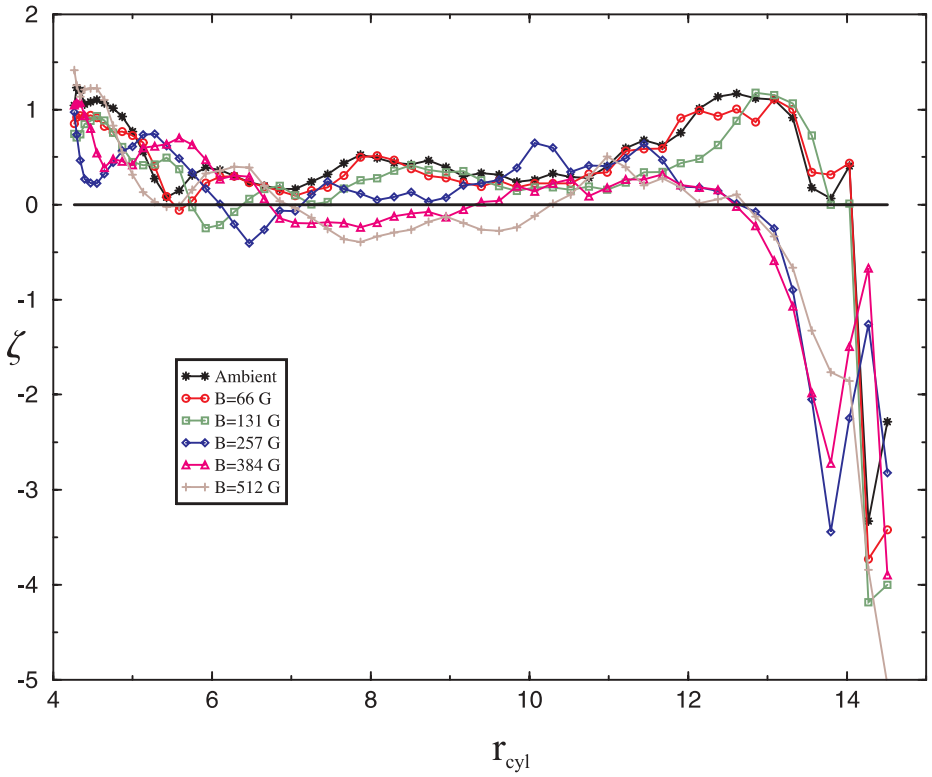

Figure 4.23: Profiles of the index $\zeta \sim 2 + d\ \ln\Omega(s)/d\ \ln s$ for $\Omega/2\pi = 30$ Hz, for five values of applied field. As the applied field increases, the ζ profiles make more frequent excursions below $\zeta = 0$, the threshold for centrifugal stability.

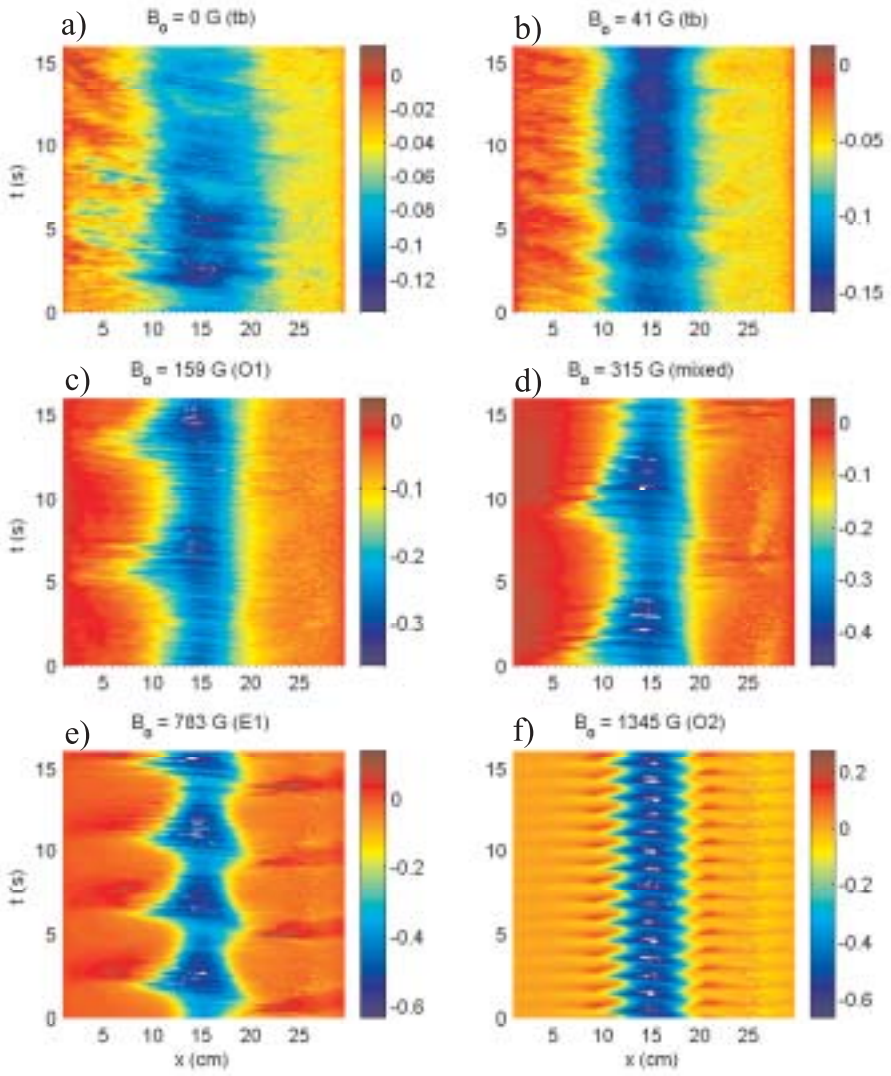

Figure 4.24: Space-time diagrams of ultrasound data. The horizontal axis is distance along the chord in Fig. 3.7, and color represents velocity component in the same direction. The cylinder tangent to the inner sphere is between $x = 10$ and 20 cm.

Are these axisymmetric induced field fluctuations causally related to the torque oscillations? The Lorentz torque at the inner sphere interface (Eqn. 2.40) provides a possible causal mechanism. The fluctuating axisymmetric poloidal modes cause a fluctuating torque through the (presumably) fixed toroidal field, which should be $\vec{T}^0_{2B}$. However, only the odd axisymmetric poloidal modes can couple with this mode; the $l = 2$ and $l = 4$ integrals vanish. Perhaps there is another toroidal mode? $\vec{T}^0_{3b}$ is the only toroidal mode that could couple to both $l = 2$ and $l = 4$ poloidal magnetic modes. To first order in the external field, $\vec{T}^0_{3b}$ could only be produced by $\vec{S}^0_{3v}$ or $\vec{T}^0_{2v}$. The latter would amount to super- and (possibly) counter- rotating jets near the tangent cylinder.

Estimating B_ϕ from torque oscillations

We might try to estimate the size of the toroidal field for the state shown in Fig. 4.25 from the relative magnitudes of the torque fluctuations in time ($\Delta\Gamma \sim 1$ N-m, see Fig. 4.25) and the $l = 3$ axisymmetric fluctuations at the inner sphere boundary. To estimate the latter, we require a radial dependence $S^0_{3b}(r)$ for the poloidal mode inside the sodium, for which we have no *a priori* estimate. As an upper estimate, we take the vacuum dependence r^{-5}, which produces a field $(a/b)^5 \sim 200$ times larger than the field fluctuations at the outer sphere $\Delta b \sim 1$ G (see Fig. 4.25)—what we might take for a lower estimate. In between these estimates would be an estimate assuming the magnetic field is well mixed within the sodium, $B_p \sim r^{-2}$. With this last estimate, Eqn. 2.40 gives:

$$B_\phi \sim \frac{\Delta\Gamma\mu_0}{2\pi(b/a)^3(a/b)^2\Delta b} \sim 50.$$

This estimate is close to the measurements of B_ϕ that we make with an immersed probe (Sect. 4.2.6).

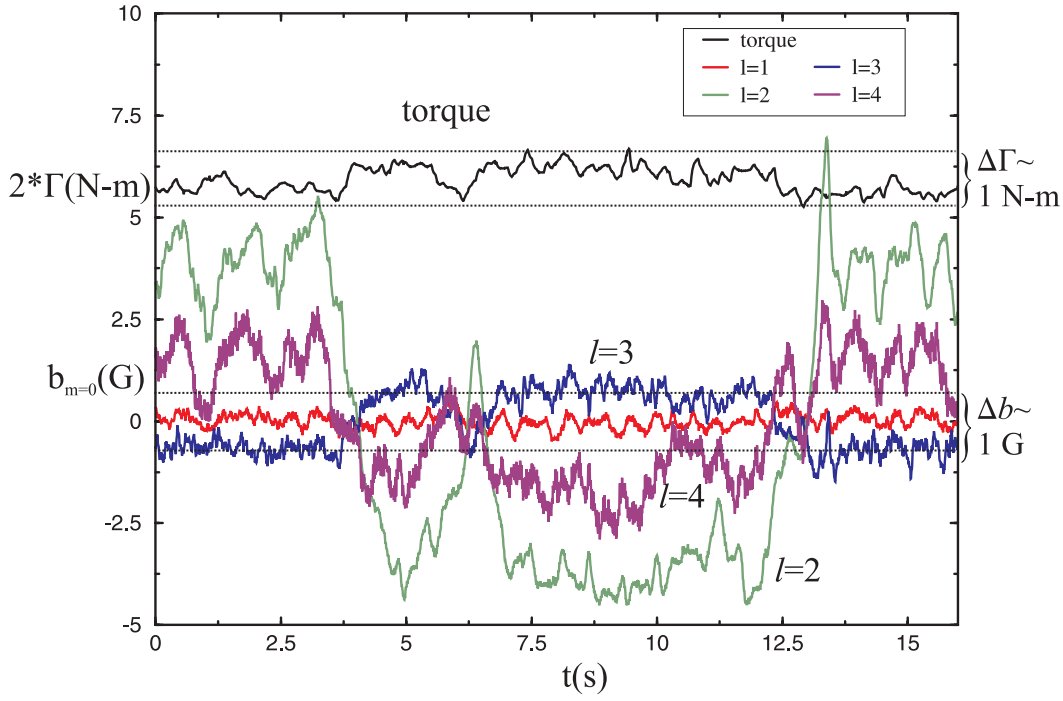

Figure 4.25: Time series of torque and coefficients of axisymmetric modes for a "transitional" state. The torque is correlated with the Gauss coefficients of axisymmetric modes (see Fig. 4.26), allowing us to make an estimate for the toroidal field. The rotation rate is $\Omega/2\pi = 40$ Hz.

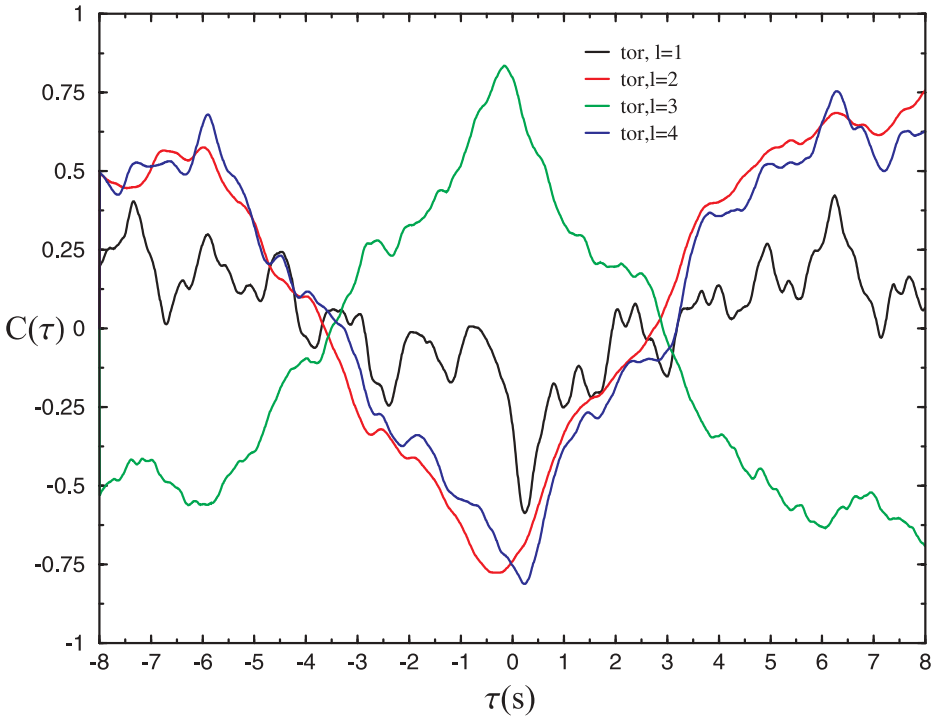

Figure 4.26: Cross-correlation function between torque and $m = 0$ coefficients, for $\Omega/2\pi =$ 40 Hz. The $l = 3$ state is strongly correlated, while the $l = 2$, $l = 4$ states are strongly anti-correlated. No strong correlations exists between the torque and any other observed Gauss coefficients. Furthermore, at other parameter values the torque is only very weakly correlated ($C < 0.25$) with all the Gauss coefficients.

4.4 Other boundary conditions

In addition to a solid copper inner sphere, we performed experiments with a hollow copper spherical shell and a (hollow) stainless steel sphere. For the hollow copper sphere, the magnetic field boundary conditions at the inner sphere interface are the same, but currents cannot flow through the sphere. For the stainless steel sphere, the boundary conditions are essentially insulating, having a conductivity 30 times lower than sodium.

One effect of having an insulating inner sphere is that the Lorentz torque is eliminated. The viscous torque alone must balance Ohmic and viscous dissipation. As seen in Fig. 4.28, the torque for the stainless steel sphere increases with applied field (and thus so must the dissipation). Presumably the increasing viscous torque is from thinning Hartmann layers, but a more complicated viscous coupling could be at work.

We should also not rule out the Lorentz torque just yet, as stainless steel, having a conductivity only 30 times lower than copper, is certainly not a perfect insulator. Might the torque increase in Fig. 4.28 be accounted for by the finite conductivity of stainless steel? Comparison to the hollow copper sphere, which has the same shell geometry as the stainless steel sphere, makes this unlikely. The Lorentz torque is proportional to the toroidal field, which in turn should be proportional to the conductivity, but the difference in torque is only a factor of two or so, not a factor of 30. Nonetheless it might be worthwhile to redo the experiments using a better insulator, like PTFE.

The insulating inner sphere experiments isolate the fluid effects from the processes in Bullard's solid analogue (see Chapter 2), which are present in the solid copper inner sphere runs. Of course with a conducting inner sphere the additional currents giving rise to the Lorentz torque affect the fluid. The conducting inner sphere case cannot be understood by adding the Lorentz torque and Ohmic dissipation of Bullard's solid analogue to the

insulating inner sphere case!

For instance, the different spheres produce quite different induced field dynamics, as shown by the standard deviation (Fig. 4.27). There barely is a primary instability with either hollow sphere. Also, as labelled in Fig. 4.27 the azimuthal wave numbers at large field are different for the stainless steel sphere ($m = 2$) than for both copper spheres ($m = 1$) at this rotation rate. Incidentally, the state for $N > 1$ was also $m = 2$ with co-rotating impellers. We turn to this geometry in the next chapter.

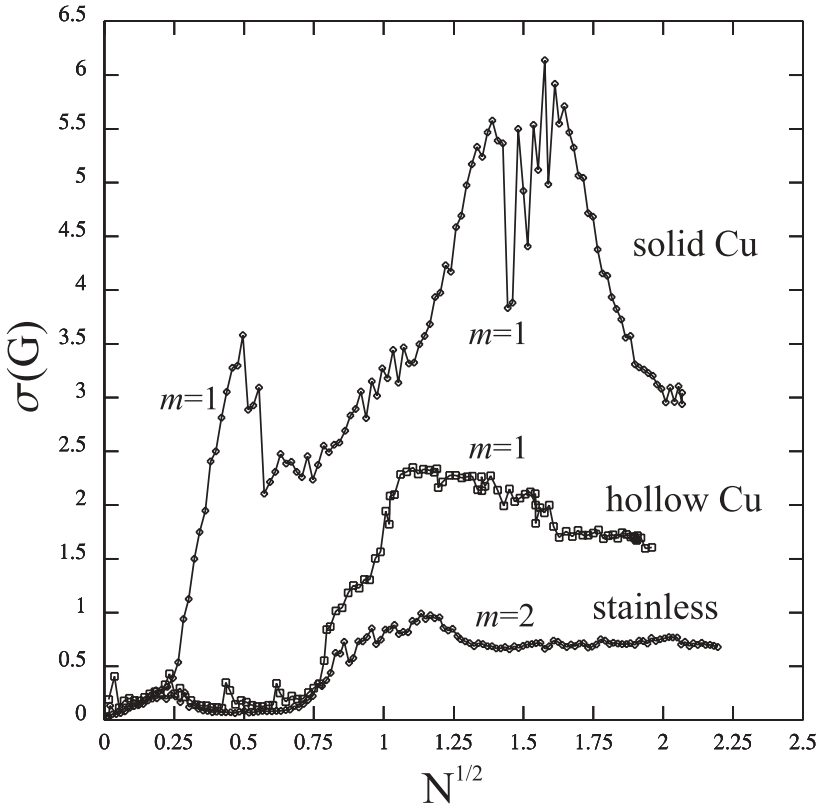

Figure 4.27: Standard deviation of induced field as a function of applied field (made dimensionless using the interaction parameter) for $\Omega/2\pi = 40$ Hz, for three types of inner sphere. Magnetic field measurements were made (before the Hall array in Chapter 3 was built) at one point outside the sphere near the equator. The same measurements for the solid copper sphere are presented for comparison. The azimuthal wave number, found from correlations in a crude array, are shown.

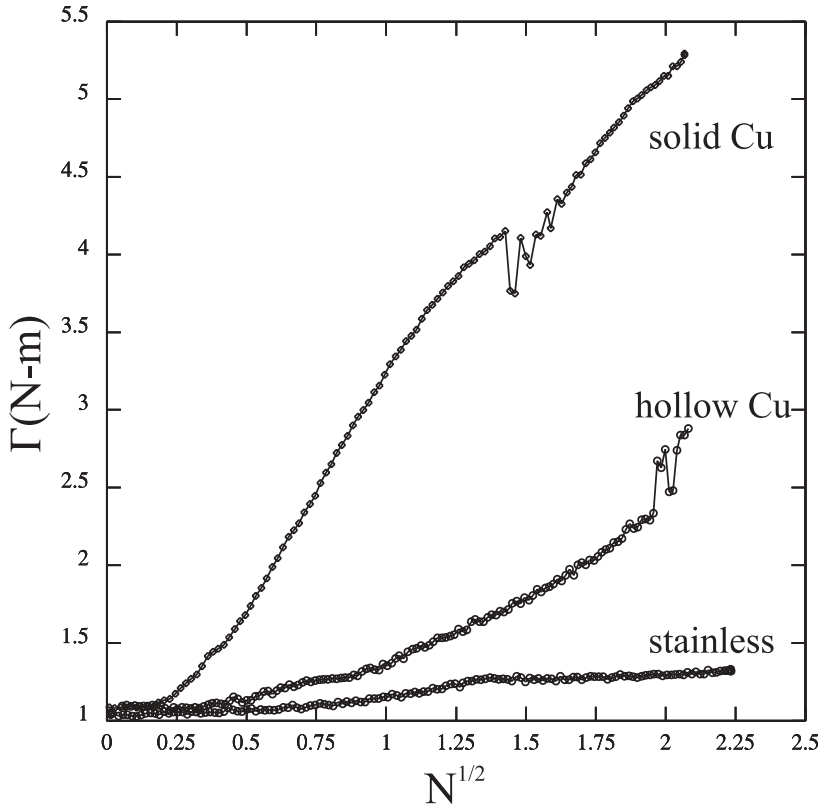

Figure 4.28: Torque as a function of applied field (made dimensionless using the interaction parameter) for $\Omega/2\pi = 40$ Hz, for three types of inner sphere. Curiously, the torque for the hollow sphere case increases abruptly at large field.

Chapter 5

Discussion

5.1 Co-rotating impellers results

This section describes the results of an experiment where co-rotating impellers replace the inner sphere. These experiments predate the Hall array and the ultrasound, so the measurements are limited. The results have already been published [91], hereafter called Paper I. We present some of the results and discussion here, and later relate them to the present findings.

Because we didn't have the Hall array for these experiments, we couldn't define regimes by the mode with the largest variance, as we do for the spherical Couette experiments. Instead we chose regimes based on a combination of the induced field standard deviation (Fig. 5.1) and the induced field power spectra frequency (Fig. 5.2), as summarized in Table 5.1.

Several things changed with this different forcing. First, with co-rotating impellers, the precession frequency was higher, and changed differently with applied field, as seen in Fig. 5.3. Also seen there, the $m = 2$ mode occurs at lower interaction parameter. On that note, all the states—to the extent we can compare them to the spherical Couette results with the Hall array—occurred at different parameter values. There were only two regimes that can be compared directly: an $m = 1$ state with an $l = 2$ poloidal correlation, and an

$m = 2$ state that had an $l = 3$ poloidal correlation (see Fig. 5.5).

The cross-correlations allow us to determine the spherical harmonic. The cross-correlation is defined as: $C(x) = \langle A(t)B(t)\rangle / \sqrt{\langle A(t)^2\rangle\langle B(t)^2\rangle}$ where $A(t)$ and $B(t)$ are magnetic field time series with time averages subtracted, from Hall probes separated by an angle x; brackets indicate time averages. In the three arrays in Paper I, cross correlations were computed relative to one probe, giving correlation as a function of angular separation. In the poloidal array the probe nearest one pole was chosen as a reference, since that permitted the largest angular separation. In the array encircling a pole, the reference probe was chosen arbitrarily (the results are independent of reference).

Though not mentioned in Paper I, we can conclude that Regime I* was, in terms of spherical harmonics, an $l = 1$, $m = 1$ mode. The cross-correlation produces an $l = 2$ correlation (not $l = 1$) because the probes are aligned in the cylindrical (as opposed to spherical) r direction. We can see this in Fig. 3.5, which shows the cylindrical r component of the $l = 1$, $m = 1$ mode on the surface of the outer sphere. Likewise, the $l = 3$, $m = 2$ correlation in regime IV corresponds to the $l = 3$, $m = 2$ spherical harmonic. That the l of the correlation and the spherical harmonic is the same here is somewhat coincidental. We would expect the number of nodes (the correlation l number in the spherical r direction) to be the spherical harmonic order l minus m—which here would be 5. The cylindrical r component has more nodes than the spherical r component, however, so the two correspond.

In regime III the state was $m = 2$ but had an ambiguous poloidal correlation. This state was likely a combination of states. With the current Hall array we would be able to determine its structure; redoing the experiment with the Hall array might be of interest for a future experiment.

Note that the collapse in Fig. 5.6 is consistent with the extrapolation used in Fig. 4.9, where we took the slope s of σ^2 vs. B_{ext} for the primary instability to increase as $s \sim \Omega^3$. In both of these scalings, the power in the induced field ($\sim \sigma^2$) at a given interaction parameter is a fixed fraction of the viscous dissipation.

5.1.1 The effect of baffles

With co-rotating impellers, we performed experiments with baffles on the inside of the outer sphere—a variation we never attempted with spherical Couette flow. With or without baffles the overall dynamics are quite similar. Note, for example, the similarity in the two cases in Figs. 5.2, 5.4, 5.1.

However, there are four main effects produced by the baffles. Most significant is how the torque changes with applied field for a fixed rotation rate (Fig. 5.7). With baffles the torque decreases with applied field, and without baffles the torque increases. The magnitude of the corresponding changes are different too: torque decrease with baffles is larger than the increase without. Second, the baffles suppress the $m = 1$ oscillations that emerge in the intermediate range of interaction parameter. It appears this state is sensitive to the boundaries. Third, the range of N values for regime III is increased, beginning at smaller N and ending at larger N (see Table 5.1). Thus the baffles apparently suppress the formation (or precession) of the instability, and better lock the precession rate to half the impeller rotation rate. The latter effect is evident in Fig. 5.4, where the induced field frequency peak is one half for large interaction parameter with baffles but only approaches one half without.

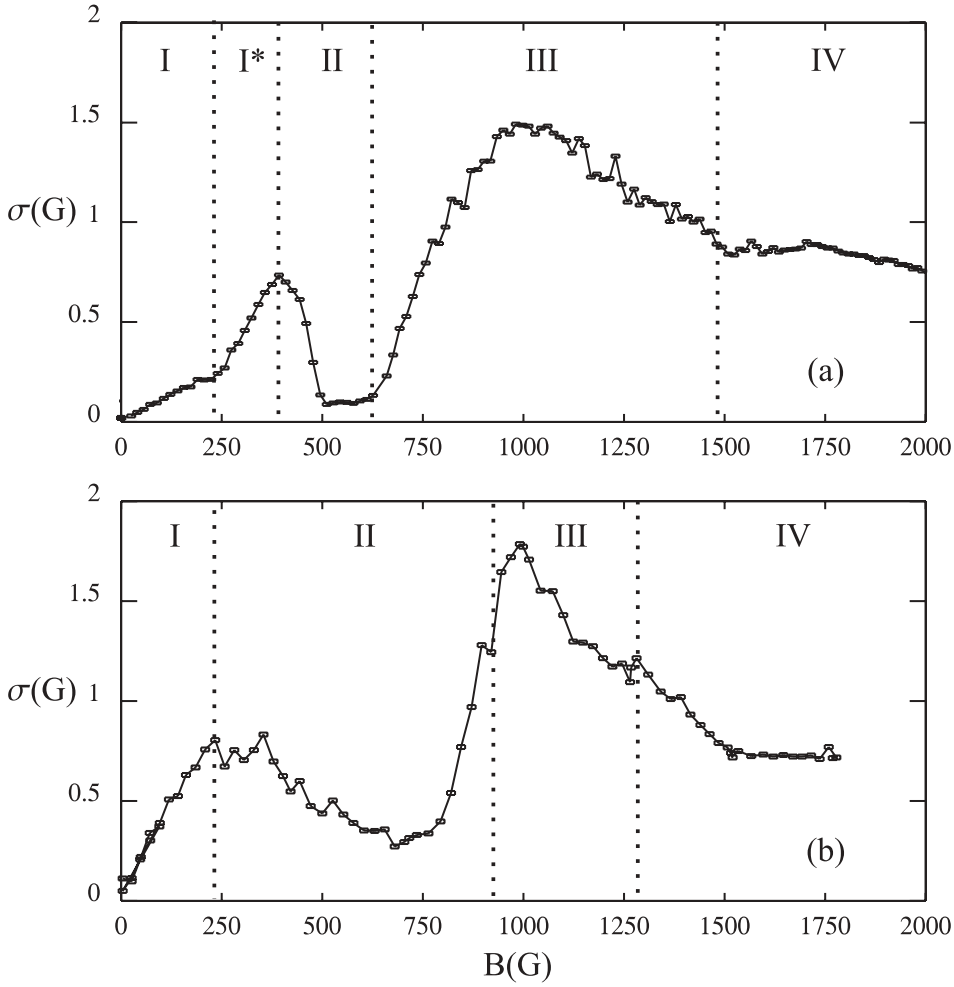

Figure 5.1: Induced field standard deviation vs. applied field at one point outside the sphere (a) with smooth walls and (b) with baffles. The measuring location was at the equator in the radial direction. The regime boundaries defined in Paper I are shown. For both (a) and (b) $R_m = 7.5$ ($\Omega/2\pi = 10$ Hz)

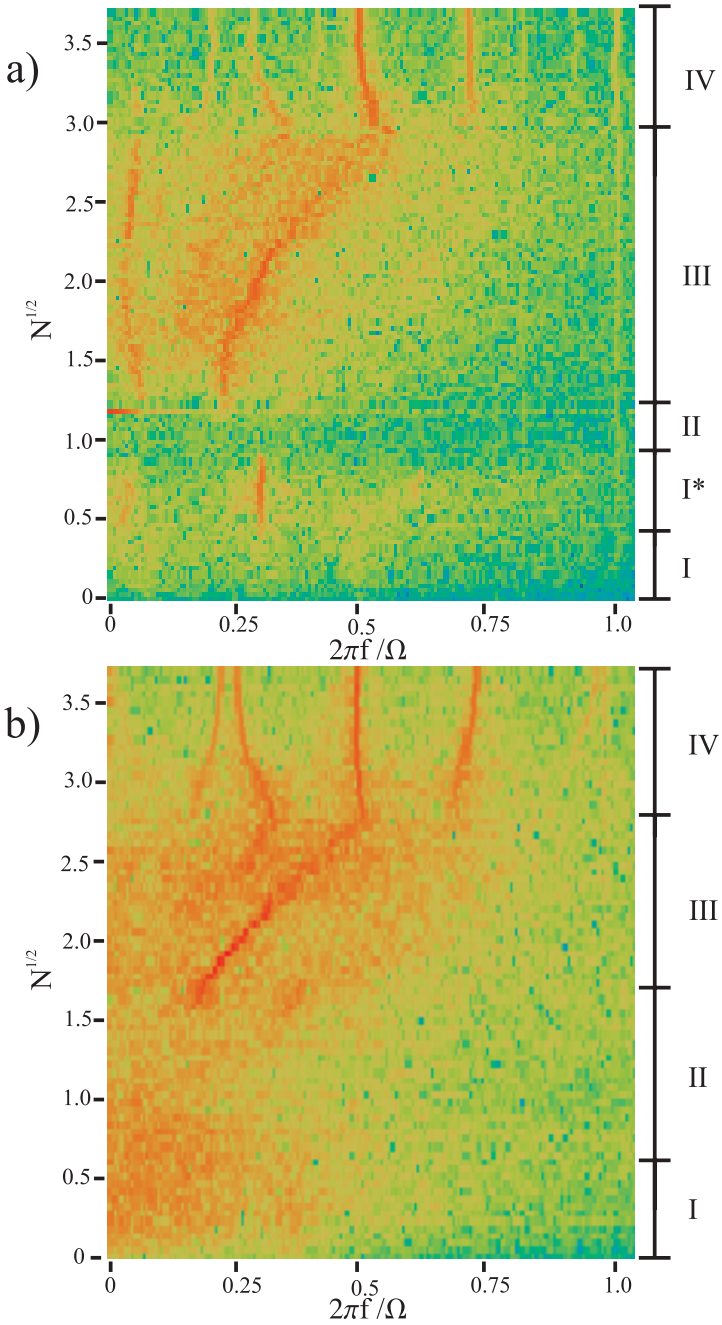

Figure 5.2: Induced field power spectra. Applied field increases up the page, where each horizontal line is a power spectrum of the induced field for smooth walls (a) and with baffles (b). Color indicates logarithmic intensity, from highest to lowest: red-yellow-green-blue. The impeller rotation rate is 10 Hz ($Re_m = 7.5$).

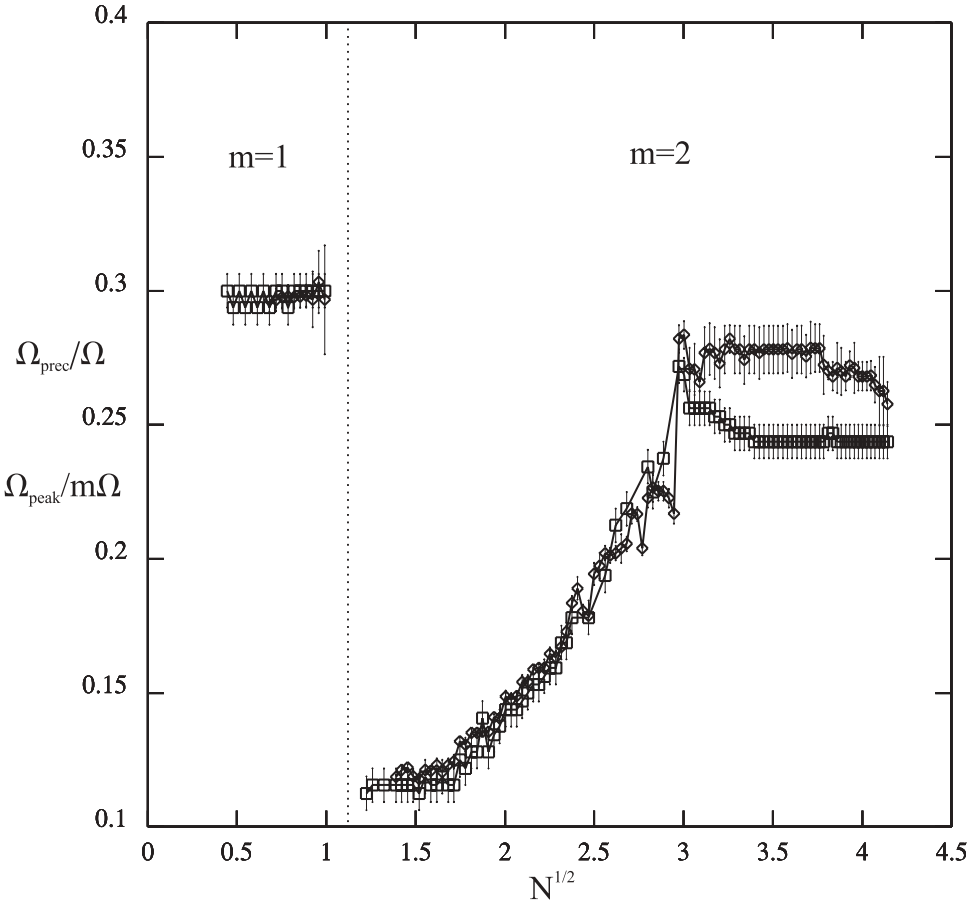

Figure 5.3: Dimensionless precession frequency from cross-correlations ($\diamond$),and frequency peak from induced field power spectra scaled by m ($\square$), vs. interaction parameter. The precession frequency was obtained by first maximizing the cross-correlation function $C(\tau, \phi)$ for probes separated by ϕ on the equatorial array. The precession angular velocity is a linear fit to the angular separation ϕ vs. optimum time lag, $\tau_{max}(\phi)$. These measurements were taken at $R_m = 7.5$ ($\Omega/2\pi = 10$ Hz) with smooth walls.

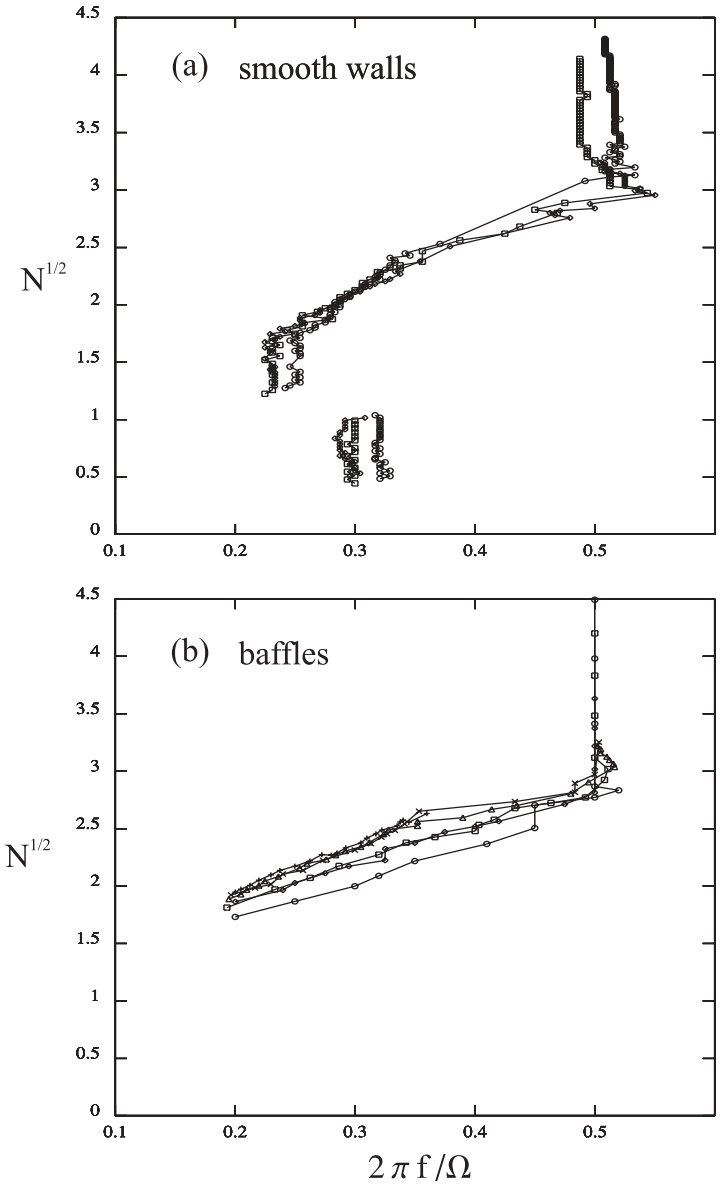

Figure 5.4: The most intense frequency in regimes I*, III and IV for impeller rotation rates: 5 Hz, $Re_m = 3.8$ ($\circ$); 7.5 Hz, $Re_m = 5.6$ ($\square$); 10 Hz, $Re_m = 7.5$ ($\diamond$); 12.5 Hz, $Re_m = 9.4$ ($\triangle$); 15 Hz, $Re_m = 11.3$ ($\times$); and 22.5 Hz, $Re_m = 18.75$ ($+$). The frequency and applied field have been made dimensionless using the rotation rate and the interaction parameter. $N^{1/2}$ is used instead of N here (and elsewhere) because the former is linear in B. In regime III, we have followed the $0.2 < 2\pi f/\Omega < 0.5$ peak and not the peak $2\pi f/\Omega < 0.1$.

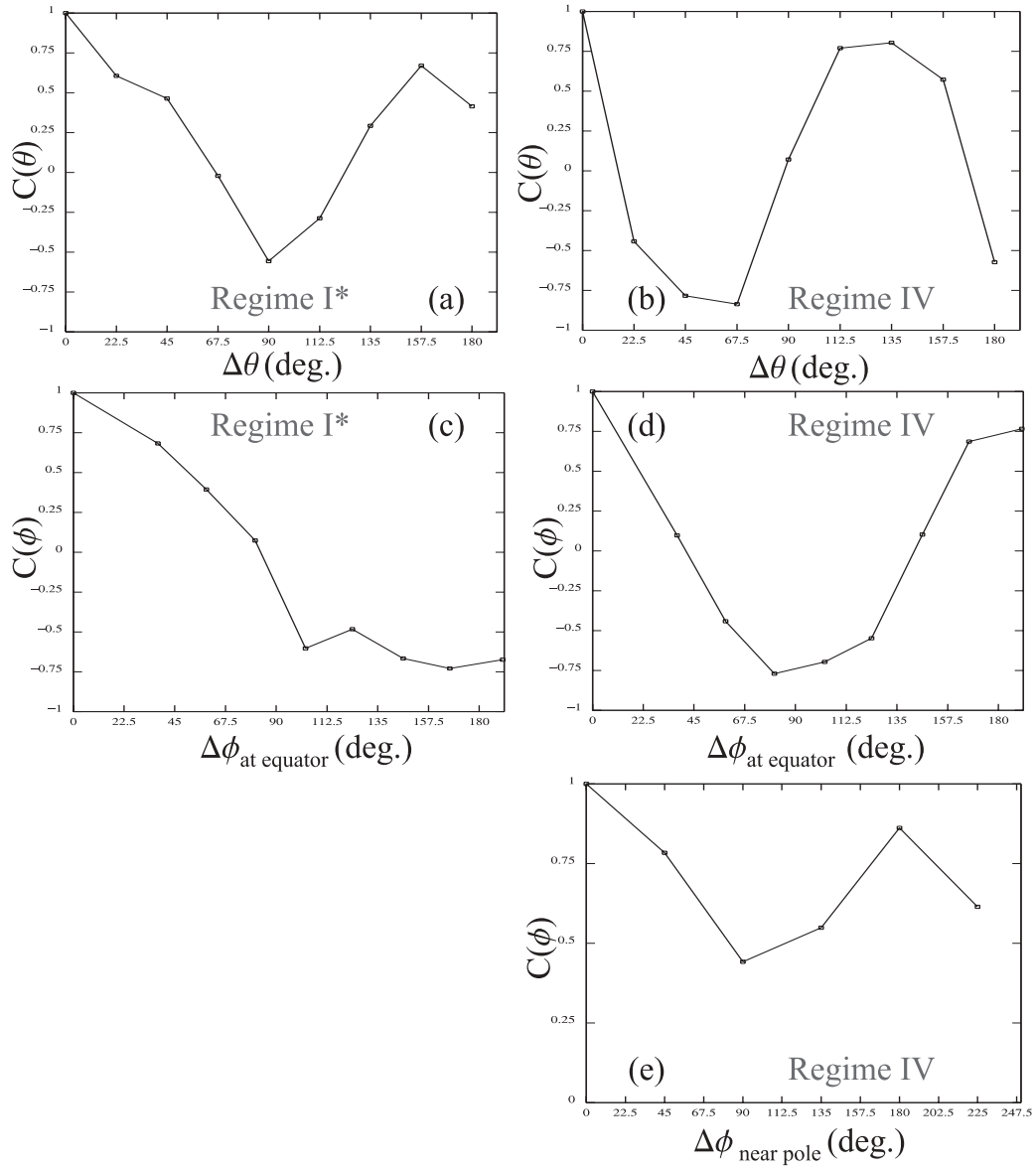

Figure 5.5: Correlations of induced field. The cross correlation as a function of poloidal angle for regime I* (a) and regime IV (b), and as a function of azimuthal angle at the equator for regime I* (c) and regime IV (d), and as a function of azimuthal angle near one pole in regime IV (e). These measurements were taken at $Re_m = 7.5$ ($\Omega/2\pi = 10$ Hz) with smooth walls. In (c), the probe at 103° is offset from the equator, which explains the deviation from the $m = 1$ trend.

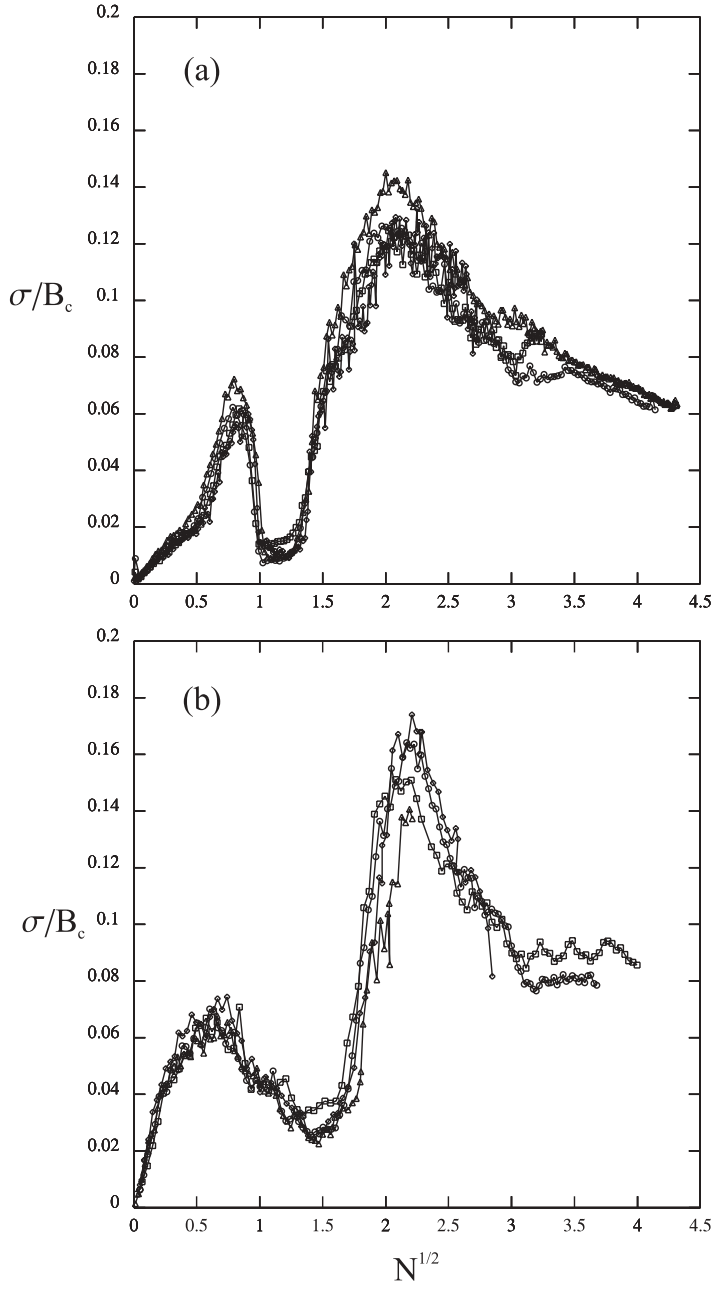

Figure 5.6: Dimensionless standard deviation of the induced field as a function of the applied field (a) with smooth walls and (b) with baffles for the magnetic Reynolds numbers: 3.8 (○), 7.5 (□), 15 (△), and 18.75 (◇). The data are made dimensionless using the interaction parameter and a characteristic magnetic field, $B_c \equiv \sqrt{\rho\mu_o ab^3\Omega^3/\eta}$.

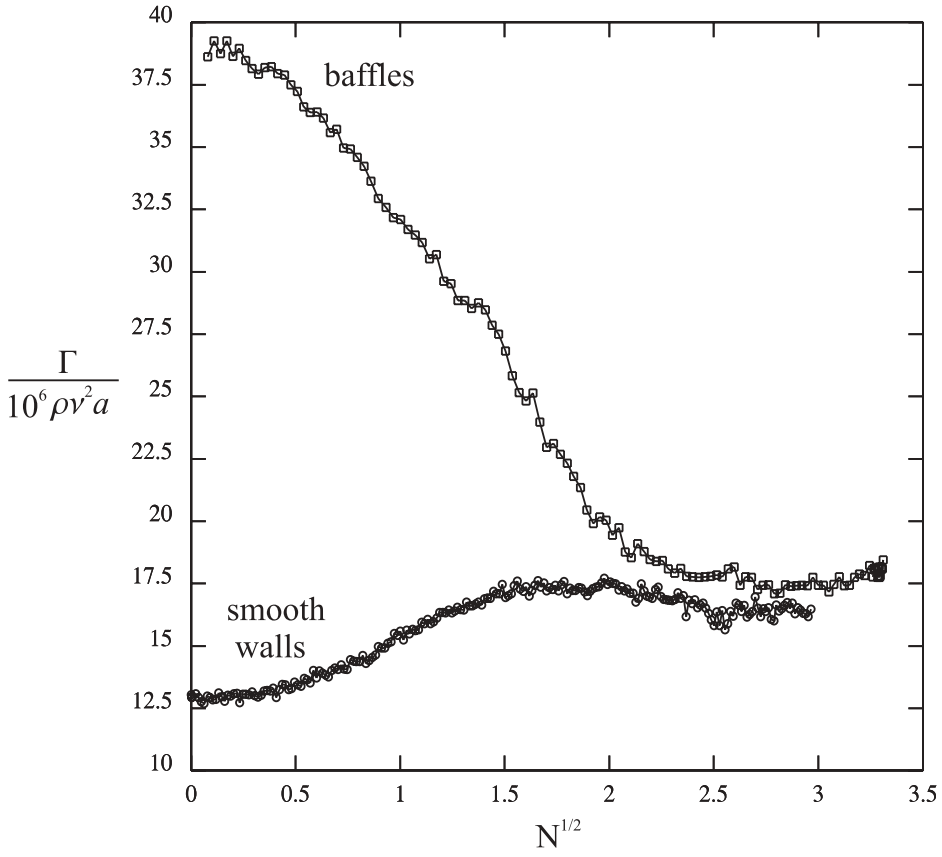

Figure 5.7: Torque as a function of applied field (made dimensionless using the interaction parameter) for $\Omega/2\pi = 40$ Hz, for co-rotating impellers, and for with baffles (see Sect. 5.1.1) inside the outer sphere and without.

Regime	Range (smooth wall)	Range (baffles)	Beginning boundary	Character
I	$0 < N < .3$	$0 < N < .3$		$\vec{B}$ passive vector
I*	$.3 < N < .6$		increasing slope of σ (see Fig. 5.1a)	$m = 1$ oscillations
II	$.6 < N < 2$	$.3 < N < 3$	first peak of σ (see Fig. 5.1)	turb. suppression
III	$2 < N < 9$	$3 < N < 7$	start of induced field freq. peak (see Fig. 5.2)	$m = 2$ oscillations, f depends on B_{ext}
IV	$N > 9$	$N > 7$	start of freq. locking (see Fig. 5.2)	$m = 2$ oscillations, f indep. of B_{ext}

Table 5.1: The five regimes.

Finally, the baffles increase the magnitude of induced field oscillations in regime I. As seen in Figs. 5.1, 5.6, the slope of σ versus B_{ext} is steeper with baffles. The baffles either make a more turbulent flow (assuming $B_{rms} \sim u_{rms}$), or makes the flow more efficiently generate induced fields (i.e., R_m is effectively made larger for a given rotation rate). This effect of the baffles disappears at higher interaction parameter.

5.2 Alternative explanations to the MRI

As mentioned in the introduction, interpreting our results as the MRI is still somewhat controversial. The most likely alternative is the instability of Hollerbach and Skinner [50]. Their instability, though magnetically-induced, is essentially the hydrodynamic Kelvin-Helmholtz instability, where a thin shear layer rolls up into a series of vortices. The shear layer forms at the cylinder aligned with the rotation and tangent to the inner sphere; it is caused by the magnetic tension coupling the fluid inside the cylinder to the rotating inner sphere, and the fluid outside the cylinder to the stationary outer walls. The applied field is necessary for instability, but the instability would presumably proceed the same if one could somehow impose the flow configuration without applied fields. The MRI by contrast has no purely hydrodynamic analogue.

There are several important similarities between our measurements and the dynamics of Hollerbach and Skinner's study, but also several important differences. The most problematic difference is that Hollerbach and Skinner's study is at Reynolds numbers that are three orders of magnitude smaller, yet they see instabilities at applied field strengths comparable to our own. The picture of magnetic tension overcoming inertia (quantified by the Reynolds number) would lead us to expect the onset external field to be correspondingly larger.

Other possible (though less plausible) explanations include dynamo action and Alfvén wave resonances. The former is ruled out because the oscillations disappear when the external field is turned off. The latter we consider next.

5.2.1 Alfvén waves?

The Alfvén wave explanation seems most plausible in the co-rotating impeller section, where as seen in Figs. 5.2, 5.4 the power spectra frequency increases nearly linearly with external field, particularly with baffles. A standing Alfvèn wave resonance frequency would also increase linearly with applied field. However, there are at least four problems with an Alfvèn wave origin for these oscillations. First, the frequency range is too low. The Alfvén velocity, $v_A = B/\sqrt{\mu_0 \rho}$, at 1000 G for our experiment is 2.8 m/s. The resulting resonance for a box of length $2a$, the sphere diameter, is thus 9.9 Hz—too large a frequency for the observed oscillations at 1000 G for the R_m explored in any of our experiments. Second, the induced field frequencies in regime III increase with rotation rate, as evidenced by the collapses in Fig. 5.4. No obvious fluid motion would modify an Alfvén wave resonance in this way. Third, the (extrapolated) zero field induced field frequency in our experiment is non-zero. Lastly, in Fig. 5.2a the frequency increase in regime III deviates more significantly from a linear trend, and there is an even lower frequency peak ($\sim 0.1\Omega$) that changes slowly (and nonlinearly) with applied field.

5.2.2 The MRI smoking gun?

What would it take to more convincingly show we have the MRI? One key MRI signature [80, 46] that could in principle be found in our experiments are local correlations between the radial and toroidal field components. In particular, the correlations must give a

positive value for the Maxwell stress, $M_{r\phi} \sim -B_r B_\phi$, to correspond with outward radial angular momentum transport.

The radial magnetic field fluctuations are caused by radial velocity gradients that stretch the imposed field, so measuring the local velocity would add additional support to an MRI interpretation. In accretion disks, this radial flow is explained by a magnetic spring force that couples nearby orbits. Consider two nearby orbits, where by Kepler's laws the inner orbit rotates faster. The magnetic spring coupling pulls the inner orbit back, lowering its angular momentum, and pulls the outer orbit forward, raising its angular momentum. In a Keplerian disk, angular momentum increases outward, so the inner orbit spirals further in and the outer spirals out. The spring force increases and the instability takes off.

We have not made measurements that could find the above correlations, but they could be made. The easier measurement —correlated velocity and magnetic field or correlated magnetic fields—would be the latter. A 2-D Hall probe that measures two perpendicular components of the magnetic field at the same location are readily purchased and could replace the 1-D probe used to measure the toroidal field. Ultrasound velocity measurements near that location could also be made, but two new ports would have be made on the spherical vessel so that the ultrasound only measures the radial velocity near the point where the toroidal field is measured. Also, the velocity measurement would of course be a centimeter or so away from the magnetic measurement, which is inside an enclosed cylinder. The purely magnetic correlations on the other hand could be measured at the same location.

5.2.3 Is a Kelvin-Helmholtz instability inconsistent with the MRI?

The differences between the MRI and Hollerbach and Skinner's Kelvin-Helmholtz-like instability are difficult to pin down. For instance, the above correlations are not, to our understanding, inconsistent with the instability of Hollerbach and Skinner. Also, the torque needed to spin the inner sphere—a measure of angular momentum transport—in their simulations increases at the instability onset, another hallmark of the MRI. Finally, it is known that Kelvin-Helmholtz instabilities can "parasitize" the MRI [43]. In simulations, after the MRI starts a secondary instability grows on a similar time scale. Our experiment and Hollerbach and Skinner's study could thus have both the MRI *and* a Kelvin-Helmholtz instability.

5.3 Base state turbulence

The base state turbulence in our experiment makes the interpretation of our results as the MRI less straightforward, leading some to call our measurements "dirty." Though not clearing the controversy surrounding Hollerbach and Skinner's results, starting with a laminar base state would shorten the connection of our results to theoretical work. We could potentially do this by rotating the outer sphere to maintain centrifugal stability. Turbulence might still be generated through hydrodynamic nonlinear or finite amplitude instabilities, however, so the plausibility of such an experiment is in question. The current apparatus is incapable of being spun, but future experiments in an apparatus currently used in a rotating convection experiments may be possible.

5.4 Dissipation and heating

Though not measured quantitatively, it was noted that when the external field was turned off after a ramp up to the maximum field the temperature dropped noticeably, as much as a degree in a 20 second span. The torque times the rotation rate equals the dissipation (minus the negligible induced field magnetic energy). This dissipation energy is converted to heat, and the dissipation could thus be measured thermally. Brito et al. [16] measure the temperature increase in a vortex of gallium with an external field and compare the deduced Ohmic dissipation with the dissipation deduced from torque measurements and find the deduced dissipation from the torque to consistently be three times higher than the temperature measurement. Their temperature measurement was at one location in the flow, and so the difference could be caused by poor thermal mixing. They offer no explanation for the difference. It might be interesting to measure the dissipation thermally in our experiment to see if a similar effect is seen.

5.5 Application to the Earth and Sun

We leave off with one of the more speculative parts of the dissertation. Though we put this section with the impeller-driven chapter, the same arguments apply to our more recent spherical Couette results as well. These connections would also be a way in which the MRI applies to the Earth and Sun. In the former, if the MRI is applicable it could be either when the Earth was formed (which would have happened in an accretion disk surrounding the Sun) or is a continuing effect that is coupled to the dynamo.

5.5.1 Core-mantle coupling

Core-mantle coupling—exchange of angular momentum between the core and the mantle—is thought is to be responsible for variations in the Length of Day, and in the orientation of Earth's axis of rotation. The degree of coupling is also an important parameter in many dynamo models [85]. Coupling can occur topographically, viscously, or electromagnetically. These processes are often considered separately (e.g., [55, 1]). However, our results show that Lorentz forces and topography need to be considered together, at least in our parameter regime. Indeed, the magnetic field can either enhance or weaken angular momentum transfer ($\approx 50\%$ over the range of interaction parameter in our experiment) to the outer case depending on the topography of the vessel walls (see Fig. 5.7). In our experiment the angular momentum transfer, with baffles and without, seems to converge at higher interaction parameter. This suggests that magnetic effects come to dominate and "wash out" pure topographic coupling when the interaction parameter is greater than about $N = 5$. The estimated values of interaction parameter in the Earth are much larger than in our experiment; thus, the Earth operates either in regime IV or in some higher regime of Lorentz force domination.

5.5.2 Moving flux lobes

Maps of the radial component of the magnetic field for 1715-1980 at the surface of the Earth indicate structure having similarities to our data. In that interval, the radial component of the Earth's field shows a fixed pattern of four flux concentrations (lobes) placed anti-symmetrically about the equator[45]. Similar to regimes III and IV in our experiment, these lobes are placed anti-symmetrically about the equator. Paleomagnetic evidence, which samples the Earth's field on longer time intervals, suggests that these lobes do

drift, though more slowly than the characteristic westward drift velocity [23, 35]. Are these lobes a precessing instability?

In our experiment, magnetic structures also drift slowly compared to the characteristic velocity (i.e., the impeller rotation rate). The relatively slowly moving flux pattern in the Earth is commonly thought to be an effect of heat flux inhomogeneities at the core-mantle boundary [45]. However, our experiment, having no such inhomogeneities, suggests this motion could be a more robust dynamical feature. One might guess that global rotation or the different forcing of the flow in the Earth would frustrate the instabilities seen in our experiment. Future experiments may determine how robust these instabilities are.

5.5.3 Boundary layers

Though the interaction parameter for the Earth is very large ($N \sim 10^5$), there is a length scale for which the flow in the Earth's core has the same interaction parameter as our experiments. This is approximately 10^{-5} the radius of the core, or about 30 m. One obvious location where the dynamics at this scale could affect geomagnetic observables are the core-mantle and inner core boundary layers. The boundary layers (thermal and Ekman) act as valves for both heat and momentum flux through the outer core. Our observations of the effects of Lorentz forces and roughness (baffles) on momentum transport may apply to these boundary layers. In addition to the effects on angular momentum transport discussed above, there should be Lorentz force effects on heat flux and core cooling. It has been argued that the turbulent momentum and heat fluxes are slaved together (by use of the Reynolds analogy, i.e., a unity turbulent Prandtl number)[57]. Using this concept and our observations of torque dependence one might expect that the heat flux from the

rough core-mantle boundary is reduced when the dynamo first turns on. This might act as one saturation mechanism for the geodynamo.

On this note, we recognize that our experiment is not an ideal geophysical model. One obvious shortcoming, as previously mentioned, is that our sphere is non-rotating—the fluid only rotates due to the co-rotating impellers or rotating inner sphere. We are thus not in a low Rossby number regime as the Earth and most astrophysical objects are. Furthermore, a system driven by impellers or an inner sphere is simpler than a system driven by convection, such as the Earth. The experimental compromises in this experiment were necessary, however, due to the difficulty and safety concerns in performing these types of experiments. With this system, rotating our sphere would cause safety problems associated with decoupling the system from an overflow reservoir. Also, without impellers we would be unable to reach the magnetic Reynolds numbers reached in this experiment (without a *much* larger device), as convection causes weaker fluid velocities. Experiments with a new 60 cm dia. rotating convection apparatus are underway that may illuminate the effects of these simplifications.

The parameter ranges for the Sun come closer to overlapping with our experiment, though there are significant differences (e.g, the sun is plasma, and has a stratified structure). Unfortunately, uncertainties in diffusivity, field strength, and the relevant length scale yield a large range for estimates of the interaction parameter for the Sun $1 < N < 10^4$ [36, 44, 73, 22, 39]. The Rossby number of the Sun is $Ro \sim 10^{-1}$, four orders of magnitude larger than in the Earth. It's possible that the relatively stronger effect of advection relative to rotation in the Sun partially explains why the Sun has more periodic dynamics than the Earth.

Chapter 6

Conclusions

We present the first laboratory realization of the magneto-rotational instability (MRI). Though the MRI is well understood, our observations establish that it exists—and that angular transport increases—in the presence of preexisting hydrodynamic turbulence. Our results connect to a local, WKB stability analysis performed in a cylindrical geometry derived by Ji et al. [53]. By adapting their use of the Lunquist number S and the magnetic Reynolds number R_m to our experiment, we make quantitative comparison to our experiment, which agree remarkably closely, considering: (1) their system was cylindrical, (2) their modes were axisymmetric, and (3) the most unstable modes had wavelengths longer than our system. They predict that modes with higher wave number will become unstable at higher external fields than lower wavenumber modes, a quality that was seen in our experiments.

We also present the first experimental study of a hydromagnetic spherical Couette flow, and only the second in any fluid at our aspect ratio $\beta = 2$, the same as the Earth's core. The instabilities found here share basic qualitative features of the instabilities that lead to turbulence at lower Reynolds number; ours, however, occur from a turbulent background. We show that the primary magnetically-induced instability is a supercritical Hopf bifurcation, and that secondary instabilities, occurring at higher external field, show

hysteresis, suggesting subcritical bifurcations.

We show that the nature of the magnetically-induced instabilities and the corresponding torque depend significantly on the electrical boundary conditions of the inner sphere. The torque increase with external field at a fixed rotation rate is approximately 5 times larger with a solid copper sphere than with a stainless steel shell, and 2-3 times larger than a thin copper shell.

We adapt Bullard and Gellman's spherical harmonic vector functions and their associated selection rules to our system, which allow us to rule out which velocity modes are not playing a role in our system's dynamics, leaving only a handful of possible modes. For the primary $O1$ instability, we determine that the velocity disturbance is $\vec{S}^1_{2v}$.

We formulate a picture for how Lorentz forces and fluid motion couple to produce energy dissipation—and we relate this to the torque required to keep the inner sphere rotating. Subsequent predictions—in particular a torque increasing quadratically with external field at low interaction parameter—are seen in the torque measurements. At larger fields, adapting an Ohmic dissipation argument from decaying turbulence, the torque is predicted to be independent of applied field, though this only occurred for impeller-driven flows. We propose an explanation for why the torque increases at our instability onset—that large scale $m = 1$ vortices increase the action of the Lorentz force on the bulk fluid. The corresponding suppression of this instability decreases the dissipation, as seen in the data.

The design and construction of a Hall array is described that allows spherical harmonic decomposition of the induced field. While conceptually and technologically straightforward, these measurements are the first of their kind in a laboratory liquid metal flow. They also allow us to construct movies of the induced field on the outer sphere surface at

an arbitrary number of points (though of course constrained by the $l = 4$ resolution of the model), which helps visualize the dynamics.

We describe a new and simpler method to obtain ultrasound measurements in liquid sodium. In the course of constructing the ultrasound transducer, we learned about the wetting of sodium with various materials, which would have effect an effect on any liquid sodium boundary, including its electrical boundary conditions.

Finally, we interpret with respect to the present findings a previously published experiment [91] using co-rotating impellers instead of a rotating inner sphere. This experiment likely showed the MRI, as it also showed a sharp increase in non-axisymmetric fluctuations as the external field was increased and their subsequent suppression as the external field was increased further. Many measurements were lacking, however, including the Hall array and ultrasound measurements. Also, the complicated geometry of the impellers limit its interpretation and the likelihood of it being successfully modelled.

6.1 Future work and unanswered questions

The most interesting future work would be to numerically model the spherical Couette flow. There are a number of possibilities in this direction. As mentioned in Chapter 2, our simple truncated mode model could be refined further. Also, a global stability analysis in a spherical geometry, comparable to the analysis of Goodman and Ji in a cylindrical geometry, would be valuable. Ultimately we'd like a see a full 3-D simulation that can be as turbulent as possible. Hollerbach, who with Skinner simulate spherical Couette flow with applied fields up to Reynolds numbers of only $Re = 2000$, thought Reynolds numbers up to $Re = 10^4$ would now be possible [51]. Comparing the results of different codes—e.g., that of Glatzmaier and Roberts, or Kuang and Bloxham—would be very

interesting. Having experimental data in hand—with clear dynamical signatures—should be an excellent way to test the various approaches. Our understanding is that several groups have already begun to model our experiment [67].

Several relatively simple but useful modifications could be made to the current setup. The simplest might be to move the transducer to point in the cylindrical radial direction. This way the radial profile could be obtained at each time step (though of course the azimuthal information would be lost). In the current position, only the time-averaged radial profile can be obtained. Also, it would be interesting to place the transducer at a pole pointing toward the inner sphere, which would give us information about the velocity modes' poloidal structure and the ratio of poloidal to toroidal flow. This ratio appears in dynamo simulations, and whether or not a dynamo exists can depend sensitively on its value. A more involved and expensive modification would be to use multiple transducers. With just two transducers one could measure both the azimuthal and radial directions at one point (the intersection of the chords) for each time sample. With more transducers, it would be possible to decompose the velocity into modes using a least squares technique. Using multiple transducers would require a new ultrasound system capable of multiplexing (or multiple units).

It might also be useful to perform more experiments with the other inner spheres and the co-rotating impellers. We only have ultrasound data and Gauss coefficient measurements for the solid copper inner sphere. With the stainless steel sphere, for instance, it was not clear if an instability developed at low field with only one Hall probe measurement; the Hall array, being able to sensitively extract modal structure from noise, could likely make this determination. Likewise, in the co-rotating impeller experiments, in regime III the poloidal structure was ambiguous, but could likely be determined with the new Hall

array. Ultrasound measurements with the impellers could also be interesting. Compared to the inner sphere, the impellers should drive a more significant flow in the cylindrical radial direction, which would presumably destroy the tangent-cylinder shear layer needed for Hollerbach's Kelvin-Helmholtz style interpretation (and might be seen with ultrasound measurements).

More interesting might be new experiments using different inner sphere radii. Spherical Couette flow in water is known to have quite different dynamics depending on the radius ratio, and the same is likely true for our system.

Finally, in the current apparatus it would be interesting to do more runs with baffles—both on the inner and outer spheres. As in [91], these baffles would simulate topographic coupling in the Earth's core. It would also be interesting to test the Lohse-Grossman theory—which makes predictions on the relative role of viscous boundary layer to bulk dissipation and its dependence on roughness—and apply it to the Hartmann layer. In particular, might Ohmic dissipation be dominated by dissipation in the boundary layer over some range of external field? Improving the precision of the torque measurements could also determine the relative effects of dissipation in the boundary layers and the bulk.

The most interesting experiment of all to try, not involving the current vessel, might be to switch the sense of rotation: rotate the outer vessel while keeping the inner stationary. The main difference would be that the Ekman pumping would occur in the opposite sense—inflow at the inner sphere equator and outflow at the poles. The sign of the induction equation interaction would switch, allowing the possibility for a dynamo—or the MRI and a dynamo! A 60 cm rotating sodium convection experiment, currently just starting to produce data, might be modified to try this experiment. The larger size may also allow a larger value of magnetic Reynolds number. Of course, the rotating convection data should

be interesting too. Finally, a third experiment—a 3 meter sodium experiment!—will be coming online in not-too-distant future, allowing even bigger magnetic Reynolds numbers. With this to look forward to, it's an exciting time indeed for hydromagnetic turbulence experiments.

Appendix A

A.1 Vector Identities

From the front cover of Jackson [54] come the following vector identities.

$$\vec{\nabla} \times \vec{\nabla}\psi = 0 \tag{A.1}$$

$$\vec{\nabla} \times \left(\vec{\nabla} \times \vec{a}\right) = \vec{\nabla}\left(\vec{\nabla} \cdot \vec{a}\right) - \nabla^2 \vec{a} \tag{A.2}$$

$$\vec{\nabla}\left(\vec{a} \cdot \vec{b}\right) = \left(\vec{a} \cdot \vec{\nabla}\right)\vec{b} + \left(\vec{b} \cdot \vec{\nabla}\right)\vec{a} + \vec{a} \times \left(\vec{\nabla} \times \vec{b}\right) + \vec{b} \times \left(\vec{\nabla} \times \vec{a}\right) \tag{A.3}$$

$$\vec{\nabla} \times \left(\vec{a} \times \vec{b}\right) = \vec{a}\left(\vec{\nabla} \cdot \vec{b}\right) - \vec{b}\left(\vec{\nabla} \cdot \vec{a}\right) + \left(\vec{b} \cdot \vec{\nabla}\right)\vec{a} - \left(\vec{a} \cdot \vec{\nabla}\right)\vec{b} \tag{A.4}$$

$$\vec{\nabla} \cdot (\psi\vec{a}) = \vec{a} \cdot \vec{\nabla}\psi + \psi\vec{\nabla} \cdot \vec{a} \tag{A.5}$$

$$\vec{\nabla} \cdot \left(\vec{a} \times \vec{b}\right) = \vec{b} \cdot \left(\vec{\nabla} \times \vec{a}\right) - \vec{a} \cdot \left(\vec{\nabla} \times \vec{b}\right) \tag{A.6}$$

$$\vec{\nabla} \cdot \left(\vec{\nabla} \times \vec{a}\right) = 0 \tag{A.7}$$

$$\vec{\nabla} \times (\psi\vec{a}) = \vec{\nabla}\psi \times \vec{a} + \psi\vec{\nabla} \times \vec{a} \tag{A.8}$$

$$\vec{a} \times \left(\vec{b} \times \vec{c}\right) = (\vec{a} \cdot \vec{c})\,\vec{b} - \left(\vec{a} \cdot \vec{b}\right)\vec{c} \tag{A.9}$$

A.2 Basic electromagnetics

Maxwell's equations relevant to hydromagnetics:

$$\vec{\nabla} \cdot \vec{B} = 0 \tag{A.10}$$

$$\vec{\nabla} \times \vec{B} = \mu_0 \vec{J} \tag{A.11}$$

$$\vec{\nabla} \cdot \vec{E} = \rho/\epsilon_0 \tag{A.12}$$

$$\vec{\nabla} \times \vec{E} = -\frac{\partial \vec{B}}{\partial t} \tag{A.13}$$

In Maxwell's equations, an additional term, the displacement current ($c^{-2}\frac{\partial \vec{E}}{\partial t}$), appears in Eqn. A.11 but is not included because it only becomes appreciable when velocities approach the speed of light.

Equation A.11 is often referred to as "Ampére's law." Equation A.13 is often referred to as "Faraday's law."

Ohm's law for a moving conductor:

$$\vec{J} = \sigma \left(\vec{E} + \vec{u} \times \vec{B} \right) \tag{A.14}$$

Table A.1 give the positions of the probes in the array.

A.3 Least squares basis functions, in C format

Below are the explicit forms for the basis functions f_c used in the least squares analysis. As mentioned in Chapter 3, these functions are the cylindrical r components of the poloidal modes $\vec{S}_l^m$, with radial functions $S_l(r) = Ar^{-l}$. The constant A is chosen to give the Schmidt normalization. This form for the radial functions gives fields whose potentials are solutions to Laplace's equation. The f's and $\vec{S}$'s are paired as follows: $(f_1 : \vec{S}_1^0)$, $(f_2 : \vec{S}_1^{1c})$, $(f_3 : \vec{S}_1^{1s})$, $(f_4 : \vec{S}_2^0)$, etc.

```
float f1 (float r, float th, float ph){
  return 3*cosf(th)*sinf(th)/powf(r,3.);}
float f2 (float r,float th, float ph){
  return (-2+3*powf(cosf(th),2))*fabs(sinf(th))/sinf(th)*cosf(ph)/powf(r,3.);}
float f3 (float r,float th, float ph){
  return (-2+3*powf(cosf(th),2))*fabs(sinf(th))/sinf(th)*sinf(ph)/powf(r,3.);}
float f4 (float r,float th, float ph){
  return .75*(3+5*cosf(2*th))*sinf(th)/powf(r,4.); }
float f5 (float r,float th, float ph){
  return sqrt(3)*(-4+5*powf(cosf(th),2))*cosf(th)*fabs(sinf(th))/
     sinf(th)*cosf(ph)/powf(r,4.);}
float f6 (float r,float th, float ph){
  return sqrt(3)*(-4+5*powf(cosf(th),2))*cosf(th)*fabs(sinf(th))/
    sinf(th)*sinf(ph)/powf(r,4.);}
float f7 (float r,float th, float ph){
  return .5*sqrt(3)*(3-5*powf(cosf(th),2))*sinf(th)*cosf(2*ph)/
     powf(r,4.);}
float f8 (float r,float th, float ph){
  return sqrt(3)*(3-5*powf(cosf(th),2))*sinf(th)*cosf(ph)*sinf(ph)/
     powf(r,4.); }
float f9 (float r,float th, float ph){
  return 5./16.*(2*sinf(2.*th)+7*sinf(4.*th))/powf(r,5.);}
float f10 (float r,float th, float ph){
  return sqrt(3/2.)*(-3+35*cosf(4.*th))*cosf(th)*cosf(ph)*
     fabs(sinf(th))/sinf(th)/16./powf(r,5.);}
float f11(float r,float th, float ph){
  return sqrt(3./2)*(-3+35*cosf(4.*th))*cosf(th)*sinf(ph)*
    fabs(sinf(th))/sinf(th)/16./powf(r,5.); }
float f12 (float r,float th, float ph){
  return .5*sqrt(15)*cosf(th)*(5-7*powf(cosf(th),2))*
  sinf(th)*cosf(2*ph)/powf(r,5);}
float f13 (float r,float th, float ph){
  return sqrt(15)*cosf(th)*(5-7*powf(cosf(th),2))*sinf(th)*
  cosf(ph)*sinf(ph)/powf(r,5); }
float f14 (float r,float th, float ph){
  return sqrt(5./2.)*(-1+7*cosf(2*th))*cosf(3*ph)*sinf(th)*
  fabs(sinf(th))/4./powf(r,5);}
```

```
float f15 (float r,float th, float ph){
  return sqrt(5./2.)*(-1+7*cosf(2*th))*sinf(3*ph)*sinf(th)*
  fabs(sinf(th))/4./powf(r,5);}
float f16 (float r,float th, float ph) {
  return 15*(2*sinf(th) + 7*(sinf(3*th) + 3*sinf(5*th)))/
  128/powf(r,6);}
float f17 (float r,float th, float ph){
  return sqrt(5./2.)*(-6*cosf(th)+7*cosf(3*th)+63*cosf(5*th))*
  cosf(ph)*fabs(sinf(th))/ sinf(th)/32./powf(r,6);}
float f18 (float r,float th, float ph) {
  return sqrt(5./2.)*(-6*cosf(th)+7*cosf(3*th)+63*cosf(5*th))*
  sinf(ph)*fabs(sinf(th))/sinf(th)/32./powf(r,6);}
float f19 (float r,float th, float ph) {
  return -sqrt(5)*(5+28*cosf(2*th)+63*cosf(4*th))*cosf(2*ph)*
  sinf(th)/32/powf(r,6);}
float f20 (float r,float th, float ph) {
  return -sqrt(5)*(5+28*cosf(2*th)+63*cosf(4*th))*sinf(2*ph)*
  sinf(th)/32/powf(r,6);}
float f21 (float r,float th, float ph) {
  return 1.5*sqrt(35./2.)*cosf(th)*(-2+3*powf(cosf(th),2))*
  cosf(3*ph)*fabs(sinf(th))*sinf(th)/powf(r,6);}
float f22 (float r,float th, float ph) {
  return 1.5*sqrt(35./2.)*cosf(th)*(-2+3*powf(cosf(th),2))*
  sinf(3*ph)*fabs(sinf(th))*sinf(th)/powf(r,6);}
float f23 (float r,float th, float ph) {
   return -sqrt(35)*(-1+9*cosf(2*th))*cosf(4*ph)*
   powf(sinf(th),3)/16/powf(r,6);}
float f24 (float r,float th, float ph) {
  return -sqrt(35)*(-1+9*cosf(2*th))*sinf(4*ph)*
  powf(sinf(th),3)/16/powf(r,6);}
```

Ring	**r/a**	θ	ϕ	**Ring**	**r/a**	θ	ϕ
Ring 1	1.333	0.6109	0.4613	Ring 3	1.383	1.702	0.2793
	1.333	0.6109	1.35886		1.383	1.702	1.06465
	1.333	0.6109	2.25646		1.383	1.702	1.85005
	1.333	0.6109	3.1540		1.383	1.702	2.6354
	1.333	0.6109	4.0517		1.383	1.702	3.4208
	1.333	0.6109	4.949		1.383	1.702	4.2062
	1.333	0.6109	5.84685		1.383	1.702	4.9916
Ring 2	1.397	1.3788	0.67195		1.383	1.702	5.7770
	1.397	1.3788	1.45735	Ring 4	1.4	2.44346	0.65275
	1.397	1.3788	2.2427		1.4	2.4435	1.55035
	1.397	1.3788	3.0281		1.4	2.4435	2.4480
	1.397	1.3788	3.8135		1.4	2.4435	3.34555
	1.397	1.3788	4.59894		1.4	2.4435	4.24314
	1.397	1.3788	5.38434		1.4	2.4435	5.14074
	1.397	1.3788	6.1697		1.4	2.4435	6.03834

Table A.1: Probe positions of the array. The radius column is a fraction of the vessel radius. The angles are in radians. In the matrix $\mathbf{M}$ (from Chapter 3), the rings are ordered: Ring 1, Ring 4, Ring 2, Ring 3.

BIBLIOGRAPHY

[1] Aldridge K.D., Bloxham J., Gubbins D., Hide R., Hinderer J., Hutcheson K.A., Jault D., Jones C.A., Legros H., Le Mouël J.-L, Lloyd D., Wahr J.M, Whaler K.A. and Zhang K. Core-mantle interactions. *Sur. in Geophys.* **11**, 329-353 (1990).

[2] Alemany A., Moreau R., Sulem L. and Frisch U. Influence of an external magnetic field on homogenous turbulence. *J. de Méca.* **18**, 277-313 (1990).

[3] Arlt R., Hollerbach R. and Rüdiger G. Differential rotation decay in the radiative envelopes of CP stars. *Astron. Astrophys.* **401**, 1087-1094 (2003).

[4] Astafyeva N.M. Nonlinear shear flow in rotating spherical layers and global atmosphere motion melling (in Russian). *Izv. Vusov PND* **5**, 3-30 (1997).

[5] Beckley H., Colgate S., Ferrel R., Romero V., and Westphahl D. Fluid flow for an experimental $\alpha - \Omega$ dynamo: plume rotation. *Bull. Am. Phys. Soc.* **2057**, 43 (1998).

[6] Bullard E.C. Electromagnetic induction in a rotating sphere. *Proc. R. Soc.* A (1949).

[7] Bullard E. and Gellman H. Homogeneous dynamos and terrestrial magnetism. *Phil. Trans. R. Soc. Lond.* A **247**, 213-278 (1954).

[8] Bloxham J. and Gubbins D. Thermal core-mantle interactions. *Nature* **325**, 511-513 (1987).

[9] Balbus S.A. and Hawley J.F. A powerful local shear instability in weakly magnetized disks. I. Linear analysis. *Astrophys. J.* **376**, L189-L192 (1991).

[10] Balbus S.A. and Hawley J.F. A powerful local shear instability in weakly magnetized disks. IV. Nonaxisymmetric perturbations. *Astrophys. J.* **400**, 610-621 (1992).

[11] Balbus S.A. and Hawley J.F. Instability, turbulence, and enhanced transport in accretion disks. *Rev. Mod. Phys.* **70**, 1-53 (1998).

[12] Balbus S.A., Hawley J.F. and Stone J.M. Nonlinear stability, hydrodynamical turbulence, and transport in disks. *Astrophys. J.* **467** (1), 76-86 (1996).

[13] Brahme A. On the hydromagnetic stability of a nonuniformly rotating fluid. *Phys. Scr.* **2**, 107-111 (1970).

[14] Brito D., Aurnou J. and Cardin P. Turbulent viscosity measurements relevant to planetary core-mantle dynamics. *Phys. Earth Planet. Inter.* **141**, 3-8 (2004).

[15] Brito D., Cardin P., Nataf H.-C. and Marolleau G. An experiment study of a geostropic vortex of gallium in a transverse magnetic field. *Phys. Earth Planet. Inter.* **91**, 77-98 (1995).

[16] Brito D., Cardin P., Nataf H.-C. and Olson P. Experiments on Joule heating and the dissipation of energy in the Earth's core. *Geophys. J. Int.* **127**, 339-347 (1996).

[17] Busse F.H. Homogeneous dynamos in planetary cores and in the laboratory. *Annu. Rev. Fluid Mech.* **32**, 383-408 (2000).

[18] Chagelishvili G.D., Zahn J.P., Tevzadze A.G., Lominadze J.G. On hydrodynamic shear turbulence in Keplerian disks: Via transient growth to bypass transition. *Astron. Astrophys.* **402** (2), 401-407 (2003).

[19] Chandrasekhar S. *Hyrodynamic and Hydromagnetic Stability.* Clarendon, Oxford (1961).

[20] Charbonneau P. and MacGregor K.B. Solar interface dynamos. II. Linear, kinematic models in spherical geometry. *Astrophys. J.* **486**, 502-520 (1997).

[21] Chen A., Mujica N., Lathrop D.P. Spherical Couette experiments in water. Unpublished.

[22] Christensen-Dalsgaard J. et al. The current state of solar modeling. *Science* **272**, 1286-1292 (1996).

[23] Constable C.G., Johnson C.L., and Lund S.P. Global geomagnetic field models for the past 3000 years: transient or permanent flux lobes? *Proc. R. Soc. Lon.* A **358**, 991-1008 (2000).

[24] Chossat P., Armbruster D. and Oprea I. (Editors) Proceedings of the NATO Advanced Research Workshop, Dynamo and Dynamics, a Mathematical Challenge, Cargèse, France, Kluwer, **66**, 59-66 (2001).

[25] Cowling T.G. *Magnetohydrodynamics.* Interscience, New York, 115 pp (1957).

[26] Davidson P.A. *An introduction to magnetohydrodynamics.* Cambridge University Press, Cambridge, 430 pp (2001).

[27] Donnelly R.J., Caldwell D.R. Experiments on the stability of hydromagnetic Couette flow. *J. Fluid Mech.* **19**, 257 (1964).

[28] Donnelly R.J., Ozima M. Hydromagnetic stability of flow between rotating cylinders. *Phys. Rev. Lett.* **4**, 497 (1960).

[29] Donnelly R.J. and Ozima M. Experiments on stability of flow between rotating cylinders in presence of a magnetic field. *Proc. R. Soc. Lond.* A, **4**, 497 (1962).

[30] Dormy E., Valet J.-P. and Courtillot V. Numerical models of the geodynamo and observation constraints. *Geochem. Geophys. Geosys.* **1**, 2000GC000062 (2000).

[31] Dudley M.L. and James R.W. Time-dependent kinematic dynamos with stationary flows. *Proc. R. Soc. Lon.* A **425**, 407-429 (1989).

[32] Eckert S. and Gerbeth G. Velocity measurments in liquid sodium by means of ultrasound Doppler velocimetry. *Exp. Fluids* **32** 542-546 (2002).

[33] Egbers C. and Pfister G. (Eds.) *Physics of rotating fluids.* Springer, Berlin (2000).

[34] Pétrélis F. and Fauve S. Saturation of the magnetic field above the dynamo threshold. em Eur. Phys. J. B **22**, 273-276 (2001).

[35] Finlay C.C. and Jackson A. Equatorially dominated magnetic field change at the surface of Earth's core. *Science* **300**, 2084-2086, (2003).

[36] Fisher G.H., Fan Y., Longcope D.W., Linton M.G., and Pevtsov A.A. The solar dynamo and emerging flux. *Sol. Phys.* **192**, 119-139 (2000).

[37] Gailitis A., Lielausis O., Platacis E., Dement'ev S., Cifersons A., Gerbeth G., Gundrum T., Stefani F., Christen M., and Will G. Magnetic field saturation in the Riga dynamo experiment. *Phys. Rev. Lett.* **86**, 3024-3027 (2001).

[38] Gailitis A., Lielausis O., Dement'ev S., Platacis E., Cifersons A., Gerbeth G., Gundrum T., Stefani F., Christen M., Hanel H. and Will G. Detection of a flow induced magnetic field eigenmode in the Riga dynamo facility. *Phys. Rev. Lett.* **84**, 4365-4368, (2000).

[39] Gilman P.A. Fluid dynamics and MHD of the solar convection zone and tachocline: current understanding and unsolved problems. *Sol. Phys.* **192**, 27-48, (2000).

[40] Gill A.E. Atmosphere-ocean dynamics. Academic Press, San Diego, (1982).

[41] Guckenheimer J. and Holmes P. *Nonlinear oscillations, dynamical systems, and bifurcations of vector fields.* Springer-Verlag, New York (1990).

[42] Glatzmaier G.A. and Roberts P.H. A three-dimensional self-consistent computer simulation of a geomagnetic field reversal. *Nature* **377**, 203-209 (1995).

[43] Goodman J. and Xu G.H. Parasitic instabilities in magnetized, differentially rotating-disks. *Astrophys. J.* **432**, 213-223 (1994).

[44] Gough D.O. and McIntyre M.E. Inevitability of a magnetic field in the Sun's radiative interior. *Nature* **394**, 755-757 (1998).

[45] Gubbins D. and Bloxham J. Morphology of the geomagnetic field and implications for the geodynamo. *Nature* **325**, 509-511 (1987).

[46] Hawley J.F. and Balbus S.A. A powerful local shear instability in weakly magnetized disks. II. Nonlinear evolution. *Astrophys. J.* **376**, 223-233 (1991).

[47] Hawley J.F., Balbus S.A. and Stone J.M. A magnetohydrodynamic nonradiative accretion flow in three dimensions. *Astrophys. J.* **554** (1), L49-L52 Part 2 (2001).

[48] Hawley J.F. Accretion disks: The magnetohydrodynamic powerhouse. *Phys. Plas.* **10**, 1946 (2003).

[49] Hollerbach R. A spectral solution of the magneto-convection equations in spherical geometry. *Int. J. Num. Meth. Fluids* **32**, 773-797 (2000).

[50] Hollerbach R. and Skinner S. Instabilities of magnetically induced shear layers and jets. *Proc. R. Soc. Lon.* A **457**, 785-802 (2001).

[51] Hollerbach R. Private communication. (2003).

[52] Hulot G., Eymin C., Langlais B., Mandea M., and Olsen N. Small-scale structure of the geodynamo inferred from Oersted and Magsat satellite data. *Nature* **416**, 620-623 (2002).

[53] Ji H., Goodman J. and Kageyama A. Magnetorotational instability in a rotating liquid metal annulus. *Mon. Not. R. Astron. Soc.* **325**, L1-L5 (2001).

[54] Jackson J.D. *Classical Electrodynamics.* Wiley, New York, 808 pp. (1998).

[55] Jault J., Hulot J.L. and Le Mouël J.L. Mechanical core-mantle coupling and dynamo modelling. *Phys. Earth Planet. Inter.* **98**, 187-191 (1996).

[56] Junk M. and Egbers C. Isothermal spherical Couette flow. In: [33].

[57] Kays W.M. and Crawford M.E. *Convective heat and mass transfer.* McGraw-Hill, New York, 420 pp. (1980).

[58] Kim W.-T. and Ostriker E.C. Magnetohydrodynamic instabilities in shearing, rotating, stratified winds and disks. *Astrophys. J.* **540**, 372-403 (2000).

[59] Kitchatinov L.L. and Rüdiger G. Global magnetic shear instability in spherical geometry. *Mon. Not. R. Astron. Soc.* **286**, 757-764, (1997).

[60] Klahr H.H. and Bodenheimer P. Turbulence in accretion disks: Vorticity generation and angular momentum transport via the global baroclinic instability. *Astrophys. J.* **582** (2), 869-892 (2003).

[61] Kuang W. and Bloxham J. An Earth-like numerical dynamo model. *Nature* **389**, 371-374 (1997).

[62] Knobloch E. Symmetry and instability in rotating hydrodynamics and magnetohydrodynamics flows. *Phys. Fluids* **8**, 1446-1454 (1996).

[63] Labbé R., Pinton J.-F., and Fauve S. Study of the von Kármán flow between coaxial corotating disks. *Phys. Fluids* **8**, 914-922 (1996).

[64] Langel R.A. The main geomagnetic field. Chapter 4 from Geomagnetism. Ed: J. Jacobs. Academic Press (1983).

[65] Lathrop D.P., Fineberg J., and Swinney H.L. Turbulent flow between concentric rotating cylinders at large Reynolds number. *Phys. Rev. Lett.* **68**, 1515 (1992).

[66] Lathrop D.P., Shew W.L. and Sisan D.R. Laboratory Experiments on the Transition to MHD Dynamos. *Plasma Phys. Cont. Fusion* **43**, 1 (2003).

[67] From personal communications to Daniel Lathrop at a recent conference in Catania, Italy: "MHD Couette flows: Experiments and models."

[68] Lehnert B. An instability of laminar flow of mercury caused by an external magnetic field. *Proc. R. Soc. Lon.* A **233**, 299-302 (1995).

[69] Lewis G.S. and Swinney H.L. Velocity structure functions, scaling, and transitions in high-Reynolds-number Couette-Taylor flow. *Phys. Rev. E* **59** (5), 5457-5467 (1999).

[70] Longaretti P.Y. On the phenomenology of hydrodynamic shear turbulence. *Astrophys. J.* **576** (1), 587-598 (2002).

[71] Lynden-Bell D. and Pringle J.E. *Mon. Not. R. Astron. Soc.* **168**, 603 (1974).

[72] Marie L., Burguete J., Daviaud F. and Leorat J. Numerical study of homogeneous dynamo based on experimental von Karman type flows. *Euro. Phys. J. B* **33** (4), 469-485 (2003).

[73] Moffatt H.K. *Magnetic field generation in electrically conducting fluids.* Cambridge University Press, Cambridge, 343 pp. (1978).

[74] Moreau R. *Magnetohydrodynamics.* Kluwer Academic Publishers, Dordrecht, 313 pp. (1990).

[75] Munson B.R., Menguturk M. Viscous incompressible flow between concentric rotating spheres. Part 3: Linear stability and experiments. *J. Fluid Mech.* **69**, 705-719 (1975).

[76] Noguchi K., Pariev V.I., Colgate S.A., Beckley H.F. and Nordhaus, J. Magnetorotational instability in liquid metal Couette flow. *Astrophys. J.* **575**, 1151 (2002).

[77] O'Connell R., Kendrik R., Nornberg M., Spence E., Bayliss A. and Forest C.B. On the possibility of a homogeneous dynamo in the laboratory. In: [24]

[78] Odier P., Pinton J-.F. and Fauve S. Advection of a magnetic field by a turbulent swirling flow. *Phys. Rev. E* **58**, 7397-7401 (1998).

[79] Oglivie G.I. and Proctor M.R.E. On the relation between viscoelastic and magnetohydrodynamic flows and their instabilities. *J. Fluid Mech.* **476**, 389-409 (2003).

[80] Ostriker E.C. Personal communication to author. (2004).

[81] Ott E. *Chaos in dynamical systems.* Cambridge University Press, Cambridge (1993).

[82] Pedlosky J. *Geophysical Fluid Dynamics.* Springer, New York (1987).

[83] Peffley N.L., Cawthorne A.B. and Lathrop D.P. Toward a self-generating dynamo: the role of turbulence. *Phys. Rev. E* **61**, 5287-5294 (2000).

[84] Richard D. On non-linear hydrodynamic instability and enhanced transport in differentially rotating flows. *Astron. Astrophys.* **408**, 409-U2 (2003).

[85] Roberts P.H. Future of geodynamo theory. *Geophys. Astrophys. Fluid Dyn.* **44**, 3-31 (1998).

[86] Roberts P.H. and Glatzmaier, G.A. Geodynamo theory and simulations. *Rev. Mod. Phys.* **72**, 1081-1123 (2000).

[87] Rochester M.G. Geomagnetic core-mantle coupling. *J. Geophys. Research* **67**, 4833-36 (1962).

[88] Rüdiger G. and Drecker A. Turbulence driven angular momentum transport in modulated Kepler flows. *Astron. Nachr.* **322**, 179-187 (2001).

[89] Rüdiger G. and Shalybkov D. Stability of axisymmetric Taylor-Couette flow in hydromagnetics. *Phys. Rev. E* **66**, 016307 (2002).

[90] Rüdiger G., Shultz M., and Shalybkov D. Linear magnetohydrodynamic Taylor-Couette instability for liquid sodium. *Phys. Rev. E* **67**, 046312 (2003).

[91] Sisan D.R., Shew W.L. and Lathrop, D.P. Lorentz force effects in magneto-turbulence. *Phys. Earth Planet. Inter.* **135**, 137-159 (2003).

[92] Shakura N.I. and Sunyaev R.A. Black holes in binary-systems - Observational appearance. *Astron. Astrophys.* **24** (3), 337 (1973).

[93] Shew W.L., Sisan D.R. and Lathrop D.P. Hunting for dynamos: eight different liquid sodium flows. In: [24] (2001).

[94] Song X. and Richard P. *Nature* **382**, 221 (1996).

[95] Spitzer L. *Physics of Fully Ionized Gases.* Wiley Interscience, New York, (1962).

[96] Steenbeck M., Krause F. and Rädler K.-H. A calculation of the mean electromotive force in an electrically conducting fluid in turbulent motion, under the influence of Coriolis forces. *Z. Naturforsch.* **21**a, 369-376. [English translation: Roberts, P.H. and Stix, M., 1971. The turbulent dynamo: a translation of a series of papers by F. Krause, K.-H. Rädler and M. Steenbeck. *Tech. Note* **60**, NCAR, Boulder, Colorado, pp. 29-47.] (1996).

[97] Stieglitz R. and Müller U. Experimental demonstration of a homogeneous two-scale dynamo. *Phys. Fluids* **13**, 561-564 (2001).

[98] Strogatz S.H. *Nonlinear dynamics and chaos.* Addison-Wesley, New York (1994).

[99] Takeda Y. Development of an ultrasound velocity profile monitor. *Nuc. Eng. And Design* **126**, 277-284 (1991).

[100] Tritton D.J., *Physical fluid dynamics.* Clarendon, Oxford, 519 pp. (1988).

[101] Urpin V. A comparison study of the vertical and magnetic shear instabilities in accretion discs. *Astron. Astro.* **404** (2), 397-403 (2003).

[102] van den Berg T.H., Doering C.R., Lohse D. and Lathrop D.P. Smooth and rough boundaries in turbulent Taylor-Couette flow. *Phys. Rev. E* **68**, 036307, (2003).

[103] Velikhov E.P. Stability of an ideally conducting liquid flowing between cylinders rotating in a magnetic field. *Sov. Phys. JETP* **9**, 995 (1959).